

NORTHWESTERN UNIVERSITY

Reinventing the Wheel:
Stress Analysis, Stability, and Optimization of the Bicycle Wheel

A DISSERTATION

SUBMITTED TO THE GRADUATE SCHOOL
IN PARTIAL FULFILLMENT OF THE REQUIREMENTS

for the degree

DOCTOR OF PHILOSOPHY

Field of Mechanical Engineering

By

Matthew Ford

EVANSTON, ILLINOIS

December 2018

© Copyright by Matthew Ford 2018

All Rights Reserved

ABSTRACT

Reinventing the Wheel:

Stress Analysis, Stability, and Optimization of the Bicycle Wheel

Matthew Ford

The tension-spoke bicycle wheel owes its stiffness and strength to a cooperative relationship between the rim and the spokes: the rim holds the spokes in tension to prevent them from buckling under external loads, while the spokes channel external forces to the hub and prevent the rim from becoming severely distorted. The prestressed design enables the slender spokes to support compressive loads without going slack, but also makes the rim susceptible to buckling under compression. I aim to uncover the principles governing the deformation and stability of the tension-spoke wheel subject to internal and external forces.

I establish a theoretical framework in which the wheel is modeled as a monosymmetric elastic beam (the rim) anchored by uniaxial elastic truss elements (the spokes) to a rigid foundation (the hub). From a general statement of the total energy of the system, I derive a set of coupled, linear, ordinary differential equations describing the deformation of the wheel and illustrate instances in which those equations can be solved analytically. To solve the general equations, I approximate the displacement field with a finite set of periodic functions to transform the differential equations to a linear matrix equation. This matrix equation leads to an intuitive model for calculating the lateral stiffness of the bicycle wheel by constructing an infinite array of springs connected in series, where each spring is associated with a discrete deformation mode. The series-springs model reveals the importance of the rim torsional stiffness, which is generally much smaller than the bending stiffness and therefore dominates the overall flexibility.

The theoretical framework incorporates the effects of spoke tension, which can both promote wheel stability by preventing spokes from going slack, and reduce wheel stiffness due to the resulting compression in the rim. Contrary to both popular belief and expert consensus, increasing spoke tension *reduces* the lateral stiffness of the wheel, which I demonstrate through theoretical calculations, finite-element simulations, and experiments. I derive an equation for the maximum tension that a wheel can support before buckling. Two well-known buckling solutions emerge as special cases of the general wheel buckling criterion.

Under external loads, two competing failure modes govern the elastic stability of the wheel: spoke buckling and rim buckling. The trade-off between spoke stability and rim stiffness leads to an optimum spoke tension of roughly 50% of the critical buckling tension in order to maximize the lateral load a wheel can withstand before spokes go slack. Using a machine designed and built by Northwestern undergraduate students, we test the strength of wheels under radial compression. By considering separately the two failure modes of spoke buckling and rim buckling, I develop a simple formula to predict the radial strength that matches our experimental result to within 10%.

Finally I discuss the existence of optimal wheel configurations and properties. By reducing the design space to a single parameter—the mass of the rim divided by the total mass—I find optimal wheels which maximize the lateral stiffness, radial strength, or buckling tension. In general, more mass should be invested in the spokes when optimizing solely for lateral stiffness, while the rim and spoke mass should be on the same order when optimizing for strength and maximum tension. The existence of an optimal wheel for a given mass, rim radius, and hub width permits investigation of general scaling laws governing stiffness and strength. The strength of the wheel with respect to buckling under radial loads is proportional to the mass divided by the radius. Therefore the strength-to-weight ratio of the wheel scales with $1/R$. Smaller wheels are inherently stronger relative to their weight than large wheels.

Acknowledgments

My deepest thanks go to my thesis committee: Oluwaseyi Balogun, Jim Papadopoulos, and John Rudnicki. I am especially grateful for the support of my adviser, Oluwaseyi Balogun, who gave me a home in his lab and took a great professional risk by encouraging me to pursue an unconventional thesis topic. This project would not have progressed without the critical eye of Jim Papadopoulos, with whom I exchanged many manuscripts and ideas and whose pioneering work on the dynamics and stability of the bicycle and studies of the mechanics of the wheel “paved the way” for this work. I am grateful for the support and advice I received from Professor Jan D. Achenbach, whose generosity with his research funds provided by Sigma Xi, and with his time and wisdom enabled this project to succeed.

I, like many mechanics researchers at Northwestern, am indebted to Dr. Joel Fenner for his consultations on experimental measurement techniques. Scarcely a test fixture or amplifier circuit is constructed in the department without his expert guidance. His boundless curiosity and encyclopedic knowledge of topics ranging from vacuum tube technology to pianoforte construction is an inspiration to me.

I am lucky to have found The Recyclery, an educational community bike shop and diverse community of generous and passionate humans. In addition to giving me access to bicycle components and tools, The Recyclery connected me with the broader world of community bike projects.

Many thanks to Professors Michael Beltran and J. Alex Birdwell, and Ellen Owens for the guidance they gave to the Northwestern Bicycle Wheel Tester team through the ME 398 capstone course.

This material is based upon work supported by the National Science Foundation Graduate Research Fellowship Program under Grant No. DGE-1324585. Conference travel was funded by the Ryan Fellowship, made possible by the generous support of Patrick G. and Shirley W. Ryan. Funding for the ME 398 wheel tester was provided by the Mechanical Engineering department at Northwestern.

I am grateful to Anne Dufault for her assistance copy-editing the manuscript.

Manuscript preparation and data availability

This thesis was created using Open Source Software wherever possible. The thesis was typeset using L^AT_EX (www.latex-project.org). Drawings and figures were created or formatted in Inkscape (inkscape.org). Version control was implemented using Git (git-scm.com). The analysis was performed using the Python programming language (www.python.org). Numerical computations were performed using NumPy [57] and Pandas [50]. Plots and data visualizations were created using Matplotlib [40]. Symbolic computations were performed using SymPy [52].

The experimental data, code, and ABAQUS input files necessary to reproduce the analysis in this thesis are archived at <https://github.com/dashdotrobot/thesis>.

List of Symbols

$\mathbf{e}_1, \mathbf{e}_2, \mathbf{e}_3$	basis vectors of a cylindrical coordinate system at the rim centroid
s	arc length coordinate
θ	angular coordinate
x, y	Cartesian coordinates of a point in the rim cross-section relative to its centroid
$(\)_p$	quantity in the prestressed configuration
$\delta(\)$	change in quantity moving from the prestressed configuration to the deformed configuration
\mathbf{u}	vector displacement field
\mathbf{u}_s	vector displacement of the rim shear center
\mathbf{u}_n	vector displacement of the spoke nipple
u, v, w	shear center displacement vector components
ϕ	rotation of the rim cross-section about its normal vector
\mathbf{d}	augmented rim displacement vector
ω	rotation vector of the line of shear centers
κ	curvature vector of the line of shear centers
ε_{33}	longitudinal strain in the rim
ε_c	longitudinal strain of the centroidal line
γ	torsion-induced shear strain
w_h	distance between hub flanges
d_h	hub flange diameter
α	out-of-plane spoke angle

β	in-plane spoke angle
n_s	number of spokes
l_s	length of a spoke
A_s	cross-sectional area of a spoke
\mathbf{n}	spoke unit vector pointing from rim to hub
c_1, c_2, c_3	direction cosines of spoke vector \mathbf{n}
\mathbf{b}_s	vector offset from rim shear center to spoke nipple
b_1, b_2	lateral and radial components of \mathbf{b}_s
R	rim radius measured at the shear center
y_0	height of the shear center above the centroid
r_x, r_y	radii of gyration for lateral and radial bending, respectively
r	outer radius of circular rim cross-section (see Optimization)
t_w	wall thickness of circular rim cross-section
A	rim cross-sectional area
I_1	rim second moment of area for radial bending
I_2	rim second moment of area for lateral bending
J	rim torsion constant
α_s	rim warping function
I_w	rim warping constant
μ	ratio of torsional stiffness to lateral bending stiffness
$\tilde{\mu}$	ratio of torsional stiffness to lateral bending stiffness, including warping effects
E, G	Young's modulus and shear modulus of the rim, respectively
E_s	Young's modulus of a spoke
ρ_r	mass density of the rim
ρ_s	mass density of the spokes
m_{rim}	mass of the rim

m_{spk}	total mass of the spokes
M	total mass of the rim and spokes
T	tension in a spoke
\bar{T}	average radial spoke tension per unit rim circumference
τ	non-dimensionalized spoke tension
T_c, \bar{T}_c, τ_c	critical tension for rim buckling
\mathbf{f}	force exerted on a spoke by the rim
\mathbf{F}_{ext}	modal force vector
F_3	axial force in the rim
F_2	radial shear force in the rim
P	external force
P_{sb}	critical external force to cause a single spoke to buckle
P_c	critical external force to cause the rim to buckle
U	strain energy
Π	total potential energy
$(\cdot)_0, (\cdot)_n^c, (\cdot)_n^s$	displacement mode coefficients, where (\cdot) may be u, v, w , or ϕ
n	mode number
N	highest mode included in the mode stiffness approximation
\mathbf{d}_m	vector of mode displacement coefficients
\mathbf{B}	matrix relating mode displacement vector to augmented displacement vector
K_s	axial stiffness of a spoke
\mathbf{k}_f	spoke stiffness matrix relating the force on a spoke to the spoke nipple displacement
\mathbf{k}	spoke augmented stiffness matrix, including ϕ terms
$\bar{\mathbf{k}}$	homogenized spoke stiffness per unit rim circumference
\bar{k}_{ij}	components of $\bar{\mathbf{k}}$ in cylindrical coordinates

\mathbf{K}_{rim}	rim modal stiffness matrix
\mathbf{K}_n^{rim}	rim stiffness matrix for the n th mode
\mathbf{K}_{spk}	spoke system modal stiffness matrix
$\bar{\mathbf{K}}_{spk}$	spoke system modal stiffness matrix, smeared-spoke approximation
K_{rad}	radial point-load stiffness of the wheel
K_{lat}	lateral point-load stiffness of the wheel
K_{tan}	tangential point-load stiffness of the wheel
K_n	scalar lateral mode stiffness of the wheel
K_n^{rim}	scalar lateral mode stiffness of the rim alone
$()^0$	stiffness evaluated at zero spoke tension
$()^{matl}$	denotes the part of the spoke proportional to E , G , or E_s
$()^{geom}$	denotes the part of the spoke stiffness proportional to \bar{T}
λ_{ij}	non-dimensionalized ratio of spoke stiffness to rim stiffness
f_n^{rad}	natural frequency of a radial bending mode
f_n^{lat}	natural frequency of a lateral bending-twisting mode
t	time
f_{rim}	fraction of wheel mass in the rim
χ	vector of wheel design parameters
χ_{extent}	vector of extensive wheel parameters, (R, M)
χ_{geom}	vector of geometric wheel parameters, $(r/R, w_h/R, d_h/R)$
χ_{matl}	vector of material wheel parameters, $(E, G, E_s, \rho_r, \rho_s)$

Table of Contents

ABSTRACT	3
Acknowledgments	5
Manuscript preparation and data availability	6
List of Symbols	7
List of Figures	13
List of Tables	15
Chapter 1. Introduction	16
1.1. History of the bicycle wheel	17
1.2. The Eiffel Tower and the Ferris Wheel	18
1.3. Technical literature on wheels	19
1.4. Outline of this thesis	24
Chapter 2. Linear stress analysis	25
2.1. Kinematics and strain energy	25
2.2. Stresses and deformation of the pretensioned wheel	36
2.3. Total potential energy of the deformed wheel	39
2.4. Equilibrium equations	42
2.5. Loads in the plane of the wheel	48
2.6. Loads out of the plane of the wheel	52
2.7. Radial–lateral coupling	62
2.8. Concluding remarks	63

	12
Chapter 3. Acoustic characterization of bicycle rims	65
3.1. Resonant frequencies of a bicycle rim	66
3.2. Experimental procedure	67
3.3. Results and discussion	70
Chapter 4. Flexural-torsional buckling under uniform tension	74
4.1. Elastic stability criterion	75
4.2. Finite-element buckling calculations	79
4.3. Closed-form solutions for special cases	81
4.4. Experimental measurement of buckling tension	84
Chapter 5. Buckling under external loads	88
5.1. Buckling under lateral force	89
5.2. Buckling under radial force	91
5.3. Radial buckling experiments	99
5.4. Concluding remarks	107
Chapter 6. Optimization of bicycle wheels	109
6.1. Performance criteria	111
6.2. Design space	112
6.3. One-parameter optimization	116
6.4. Scaling of strength with size and mass	117
Concluding Remarks	119
References	121
Appendix	126

List of Figures

2.1	Schematic of a typical bicycle wheel	25
2.2	Comparison of smeared-spokes and discrete-spokes calculations	34
2.3	Radial deformation of the wheel under uniform tension	38
2.4	Radial-tangential deformation of the wheel	49
2.5	Change in spokes tensions under in-plane loads	51
2.6	Equivalent spring model for lateral stiffness	55
2.7	Influence of spoke tension on lateral stiffness	57
2.8	Lateral stiffness with laterally-offset spokes	60
2.9	Stiffness of wheels with left-right asymmetry	63
3.1	Acoustic test on a rim	68
3.2	Mechanical testing of rims	69
3.3	Results from acoustic and mechanical tests on rims	71
3.4	Acoustic mode stiffnesses of rims	73
4.1	Buckling tension and mode shapes	78
4.2	Simulation of non-linear buckling under spoke tension	80
4.3	Four-point bending test on a wheel	85
4.4	Four-point bending test results	86
5.1	A bicycle with a buckled wheel	88
5.2	Buckling under lateral force	90

	14
5.3 Buckling under radial force	92
5.4 Buckling of wheels with laterally restrained spokes	93
5.5 Single-degree-of-freedom wheel buckling model	95
5.6 Comparison of radial strength model and simulation results	96
5.7 Post-buckling behavior under radial load	98
5.8 NU bicycle wheel testing machine	100
5.9 Lateral carriage assembly	103
5.10 Radial buckling experimental results	105
6.1 Trends in one-parameter optimization	116
6.2 Scaling laws for radial strength	117
B.1 Diameter measurement of CR18 rim	129
C.1 Frequency response of the iPhone SE microphone	132
C.2 Fitted peaks in acoustic frequency spectra	134
E.1 Schematic of rim four-point bending test	136

List of Tables

2.1	Example lateral stiffness properties	56
3.1	Properties of rims for acoustic testing	67
4.1	Simplifying assumptions for tension buckling criterion	76
5.1	Product Needs for the bicycle wheel tester	101
5.2	Radial buckling experimental results	104
6.1	Comparison of selected references on wheel optimization	110
6.2	Design parameters for optimization	113
B.1	Wheel properties	130
B.2	Wheel properties for buckling simulations	131
C.1	Rim properties from acoustic and mechanical testing	133
D.1	Calibration constants for WheelFanatyk tensiometer	135

CHAPTER 1

Introduction

In its heyday in the 1890s, the bicycle was regarded as one of the most advanced products of the Industrial Age. Inventors and industrialists spent considerable effort mastering the manufacture of lighter, more efficient machines. Many now-ubiquitous technologies made their debut on or were perfected for the bicycle including ball-bearings, chain drives, and tension-spoke wheels [36]. By the end of the 1890s, patents for bicycles and bicycle-related technologies accounted for roughly two-thirds of all patent applications in the United States [69]. Many pioneering bicycle firms and inventors of the 1890s transitioned to automobile and aerospace technology in the early part of the 20th century.

Bicycle technology has not radically changed since the introduction of derailleur gears in the 1920s. The number of technical minds bent on the perfection of “the mechanical horse” has diminished, but this may be seen as the inevitable maturation of a robust and enduring technology. The bicycle is humanity’s most efficient means of transportation¹—a technology for the age of climate change—and will be a key component of the modern, sustainable city.

Bicycles have not become significantly more complex over time, which has enabled widespread participation in bicycle design and maintenance by amateurs. A few industry standards dominate each major component, allowing parts to be easily swapped, upgraded, or modified. Many U.S. cities have a bicycle co-op where community members can collaborate, share tools, and learn about bicycle repair². A classic example of “user innovation” is the invention of the mountain bike in California by a loose group of cycling enthusiasts. Using older steel-frame bicycles (mainly used Schwinn from the 1950s), these pioneers hacked together rugged bikes to meet the demands of off-road cycling. Eventually, the industry picked up the trend and mountain bicycles constitute the majority of bicycles sold in the U.S. today [17].

¹Comparisons are sensitive to specific assumptions, but the bicycle almost always comes out on top. See, e.g. [29].

²See <http://www.bikecollectives.org> for an incomplete list.

1.1. History of the bicycle wheel

With its elegant system of slender spokes, the wheel is the most recognizable component of the bicycle—an invention whose success it critically enabled. Indeed, the term “wheel” was once used to refer to the entire bicycle; the League of American Bicyclists was known as the League of American Wheelmen until changing their name in 1994 [82].

The vast majority of bicycle wheels produced today are wire-spoked wheels consisting of a system of slender spokes held under tension by a rim. Originally conceived as landing gear for the yet-to-be-invented aircraft by Sir George Cayley in 1808 [3], the tension-spoke wheel saw its first practical application on the bicycle and was later utilized in early automobiles and aircraft [34]. Although materials and manufacturing methods have evolved over time, the fundamental design and operating principle has not significantly changed since the 1870s.

For the first 50 years of the bicycle’s history³, wheels generally consisted of a small number of stout wooden spokes fitted into individual wooden rim sections, or felloes, fitted together with mortice and tenon joints. An iron tire was heated and placed around the circumference of the rim and allowed to cool and contract, putting the spokes and rim under compression and the tire under tension [77]. The structure was held together by prestress; the rim sections were not joined except by compression. The spokes, which had to be quite wide to prevent lateral buckling, made these wheels extremely heavy. In 1869, A French mechanic and inventor named Eugene Meyer obtained a patent for a tensioned, wire-spoked wheel which enabled the construction of much larger wheels [15]. In Meyer’s tension-spoke wheel the method of prestress was reversed: each slender iron spoke could be individually pretensioned, stabilized by an iron rim in compression. The spokes in such a wheel can effectively support compression—by losing some, but not all, of their tension—without the risk of lateral buckling.

Several other prestressing methods were developed around the same time. W. F. Reynolds and J. A. Mays introduced the Phantom bicycle featuring long wire spokes secured to one flange of the hub, looped through an eyelet on the rim, and secured to the other flange [36]. The spokes were all tensioned simultaneously by spreading apart the hub flanges. The spokes of James Starley’s successful Ariel bicycle, which emerged

³Although the first steerable, two-wheeled vehicle, the Draisienne, was invented in 1817, some authors reserve the word “bicycle” for two-wheeled pedal-driven vehicles.

radially from the hub, were prestressed simultaneously by rotating the hub relative to the rim by means of a pair of levers connected to the hub and secured to the rim by adjustable tensioning rods [13]. Although the spokes were attached radially (and therefore could not efficiently transmit torque), the prestress resulted in a small offset which conferred rotational stiffness. The tangent-spoked wheel, developed by Starley in 1874, achieved rotational stiffness by connecting the spokes tangent to the hub. This remains the most common spoke configuration used today.

Prestressing the spokes enabled the construction of larger and lighter wheels. The gear of a direct-drive pedal-driven bicycle (the linear distance traveled per rotation of the cranks) is equal to the circumference of the wheel, so a larger wheel confers a considerable speed advantage. The high-wheel bicycle enjoyed popularity primarily amongst young men of means throughout the 1880s and into the 1890s [79]. The development of practical and lightweight chain drives brought the “safety bicycle”—so named because the gear ratio afforded by the chain enabled the use of a smaller front wheel, reducing the risk of pitching over the handlebars—to the masses.

1.2. The Eiffel Tower and the Ferris Wheel

The tensioned bicycle wheel arrived during a time of rapid progress in the use of iron and steel in lightweight structures. The first prestressed bicycle wheels were commonly called “suspension wheels,” perhaps due to an analogy with the suspension bridge, itself a relatively new structural innovation [76]. The Home Insurance Building in Chicago, completed in 1885, was partially built around a steel skeleton-frame and is widely recognized as an early skyscraper [53]. The Eiffel Tower, constructed in 1889 for the World’s Fair in Paris, became the tallest human-built structure in the world. Its sparse, wrought-iron truss frame initially drew sharp criticism on aesthetic grounds, but eventually became one of the most enduring and recognizable symbols of the city, and continues to engage engineers and mathematicians today [89].

Perhaps the most striking structural analogy to the bicycle wheel, the Ferris Wheel, was completed in 1893 for the Columbian World Exposition in Chicago. Crafted as Chicago’s answer to the Eiffel tower, George Washington Gale Ferris’ wheel drew frequent comparisons to the bicycle, such as the following observation by Julian Hawthorne (son of the novelist, Nathaniel), [46]:

“...it has no visible means of support—none that appear adequate. The spokes look like cobwebs; they are after the fashion of those on the newest make of bicycles.”

Of course the means of support *were* adequate; the “Chicago Wheel” derived its remarkable stability from the fact that the iron spokes were pretensioned by turnbuckles so as not to lose tension (and therefore stiffness) when they came to be at the top of the wheel. The construction of the Ferris Wheel, and perhaps the reluctance of its builders to satisfy the engineering community with details of its analysis, spurred considerable interest and debate [2, 75]. These early analyses relied heavily on intuition or assumed that the rim was stiff enough that all deformation was confined to the spokes. But the technical marvel of the Ferris Wheel, and the bicycle wheel that preceded it, may have inspired a long but sparse effort to understand the mechanics of pretensioned wheels.

1.3. Technical literature on wheels

In his 1896 treatise on the mechanics and design of bicycles and tricycles [77], Archibald Sharp gave a brief, qualitative description of the deformation of a tension-spoke wheel. He correctly noted that the bottom spokes play the most dynamic role in supporting loads applied to the hub. He then motivated the development of a set of equations for the tensions in the spokes using a polygonal approximation for the rim, but correctly deduced that they form a statically indeterminate system and did not attempt a solution.

In 1901 Bernard Smith [78] published an analysis of the deformation of a pretensioned wheel with purely radial spokes by assuming that the number of spokes is great enough such that the spoke stiffness is continuously distributed about the rim and produces a radial reaction force proportional to radial displacement. This clever method transforms a discrete system of coupled equations for the spoke tensions into a linear, ordinary differential equation for the radial displacement of the rim. Through an analytical solution, he came to the same conclusion as Sharp—that the bottom spokes play the most direct role in supporting loads—and gave a table for the influence function (change in spoke tensions per unit applied radial load) for a typical 32-spoke wheel.

The most complete theoretical treatment of the deformations of tension-spoke wheels came in a series of investigations in 1931-32 by Alfred J. Sutton Pippard and various coauthors. Pippard, a civil engineer with expertise in elasticity of lightweight structures, was engaged by the British Royal Air Force to undertake an

investigation of lightweight wheels for aircraft⁴. Pippard and Francis derived a set of coupled equations for the spoke tensions in radially-spoked wheels under radial loads, and gave tables for the calculation of wheels with up to six spokes [66]. Apparently unaware of Smith’s earlier contribution, they also gave a general analytical solution using Smith’s smeared-spokes approximation. Recognizing the power of this approach, Pippard and White extended the method to analysis of wheels with non-radial spokes [68]. Pippard and Francis analyzed the wheel under lateral loads [67], although they neglected the effects of spoke tension.

For the purposes of validation, Pippard and Francis performed radial extension tests on specially-constructed wheels with pin-jointed radial spokes to compare the change in spoke tension to the smeared-spokes model. They achieved good agreement in the spoke tension at the load point (maximum difference less than 9%) between theory and experiments, and noted that accuracy increased with the number of spokes, as is expected when assuming that the spoke stiffness is continuously distributed. The rims used in their experiments, cut from solid steel plate, were quite stiff in bending compared to the axial stiffness of the spokes, which would have increased the accuracy of their model.

The Smith-Pippard approximation—taking the limit in which the number of spokes goes to infinity—transforms the bicycle wheel into a curved beam resting on an elastic foundation. The foundation produces a reaction at each point proportional to the local deflection. The stiffness of the beam effectively spreads out point loads with a characteristic decay length equal to $(4EI/k)^{1/4}$, where EI is the bending stiffness of the beam around the relevant axis and k is the stiffness constant of the foundation (in units of force per unit length, per unit deflection). The theory of beams on elastic foundations was broadly summarized and formalized by Hetenyi [37] in his 1946 monograph. He included a treatment of radial deflection of rings on elastic foundations, citing Pippard et. al., but not Smith. The significance of the beam-on-elastic-foundation analogy was noted by Papadopoulos in a note on wheel mechanics in the now-defunct journal *Human Power* [59]:

“...it may be most helpful to think of a bicycle wheel as a long, bendable, twistable, curved rod (or beam) held in place by 36 springs anchored in a firmly-held hub. Forces in any direction applied to a point on the rim always produce the greatest effects in spokes nearby.”

⁴After his retirement in 1956, Pippard took up a yearlong visiting lecturer position at Northwestern University where he taught undergraduate and graduate courses in theory of structures.

1.3.1. Modern bicycle wheel literature

After Pippard there has been scant development of broadly applicable analytical theories for stress analysis of bicycle wheels, to the best of my knowledge. Instead, modern studies have employed finite-element analysis and experimental techniques.

Jobst Brandt, a mechanical engineer and cycling enthusiast, published *The Bicycle Wheel* in 1981 as a practical manual for wheelbuilding and brief treatise on wheel mechanics drawn from his own experience and analysis [10]. To illustrate some key points of wheel mechanics, Brandt calculated radial and tangential deformations on a 2-dimensional model of a typical wheel using the linear finite-element method. As in Smith and Pippard's analyses, the dominant role of the lower spokes is apparent. Finite-element results also exhibit a phenomenon suppressed by the continuum approximation of Pippard and Smith: a drive torque applied to the hub and reacted at the road contact point produces a small, periodic, radial distortion of the wheel with a period of four spokes. This effect is due to the local increase and decrease in tensions from leading and trailing spokes in a tangent-spoked wheel. The same periodic deformation would be observed in the lateral deflection, which was not considered in Brandt's 2-dimensional analysis.

Salamon and Oldham published the first comparative finite-element study of the bicycle wheel [73]. They compared wheels with radial spokes to wheels with tangent spokes under purely radial loading, finding that the radially-spoked wheel was only 5% stiffer than the tangent-spoked wheel and the maximum stresses were substantially similar. They also analyzed wheels with 3, 7, and 9 spokes (which would typically not be built with prestress) and found that the bending stress varied by up to an order of magnitude when the load was moved from directly at a spoke to a point halfway between spokes.

Most experimental and theoretical studies have neglected the effect of the tire and inner tube due to the considerable complexity introduced. Burgoyne and Dilmaghanian [12] studied the entire spokes-rim-tire-tube assembly as an engineering system and experimentally demonstrated that the tire effectively spreads out radial loads along a segment of rim near the contact point. The load distribution has a significant effect on the bending moment sustained by the rim (hence the danger of damaging the rim when hitting a pothole at low inflation pressure), but only has a small effect on spoke strain. They identified three systems of prestress in the wheel: the spokes prestressed against the rim, the tire casing prestressed against the inflated

inner tube, and (incorrectly) the tire bead prestressed against the rim [60]. The third effect is not present since the diameter of the tire bead is significantly larger than the diameter of the bottom of the rim channel.

Wheel failure is most commonly preceded by the gradual accumulation of fatigue damage, especially in the spokes, which are repeatedly stressed each time the wheel rotates or a lateral load is encountered. Henri Gavin constructed an instrumented wheel for measuring strain on a single spoke during naturalistic riding conditions in order to make fatigue life predictions [28]. Averaged road testing results from three wheels with different spoke configurations showed negligible differences in strain history between the three wheels, however, it should be noted that possible strains from lateral or braking loads which produced non-periodic strains were omitted from the analysis. Gavin also described an experimental method to obtain the lateral bending stiffness EI_2 and torsional stiffness GJ of a bicycle rim, but he did not conduct lateral stiffness tests on a wheel to compare with theory or his finite-element calculations.

The rim and spokes are structurally coupled and their contributions to wheel stiffness cannot be easily decoupled. In an attempt to separately quantify the contributions of the spokes and rim, Minguez and Vogwell [54] derived a model for the radial stiffness of bicycle wheels by assuming that the top half of the rim remains perfectly rigid, and the bottom half deforms from a circular arc to an ellipsoidal (squashed) arc. They calculated the stiffness using Castigliano's theorem on the assumed displacement field. This assumption contradicts the qualitative observations by Sharp and calculations by Smith for typical wheels (that the distortion of the rim is limited to a narrow arc about the bottom spoke), but they nevertheless achieved close (within 10%) agreement due to their choice of very stiff rims on wheels with few (< 18) spokes.

The structural simplicity of the bicycle wheel makes finite-element analysis straightforward: if localized stresses are not of great interest the spokes and rim can be readily modeled with structural beam elements, and no delicate choices must be made regarding meshing except to choose an appropriate discretization for the curvature of the rim. Due to its structural simplicity and broad appeal, the bicycle wheel is a popular subject for undergraduate and masters theses and hobbyist projects. These authors have focused on stiffness and stress analysis [35, 56], optimization [42, 83], and buckling [43].

Papadopoulos and Wilson reviewed the most important insights and open questions regarding tension-spoke wheels in a straightforward and non-mathematical treatment in *Bicycling Science* [90]. They gave qualitative descriptions of the structural response under radial, lateral, and tangential loads, and briefly discussed wheel buckling and other failure modes. In describing the factors involved in bicycle wheel buckling and collapse, they also noted the importance of torsional stiffness of the rim. Comparing a double-wall rim (whose cross-section contains a large hollow cavity) to a single-wall rim with a much greater bending stiffness, the single-wall rim will deform laterally much more readily due to its low torsional stiffness. Several of the problems considered in this thesis are direct responses to comments and speculations by Papadopoulos and Wilson.

1.3.2. The “gray” literature

Other than the studies mentioned above, scant attention has been paid to the bicycle wheel in the peer-reviewed technical literature. However, a number of hobbyists and specialists have published experimental results on the wheel with varying levels of technical rigor and documentation. Stiffness, being the most intuitive mechanical property to the non-specialist, is generally the focus of these studies. It is generally agreed that lateral stiffness plays a much more significant role than radial stiffness in the performance and qualitative experience of a wheel [45]. The radial stiffness is generally about two orders of magnitude larger than the lateral stiffness, and is completely obscured by the flexibility of the inflated tire.

Damon Rinard devised a simple setup for measuring the lateral stiffness of wheels by gripping the axle between specially-machined aluminum blocks held in a milling machine and loading the rim with hanging weights [70]. In addition to simply publishing the lateral stiffness for a variety of commercially-available wheels, he also addressed several questions about stiffness including variation with spoke tension (discussed in detail in Section 2.6), difference in stiffness between the right and left directions, and the stiffness of a few specialized spoke configurations. Because he measured stiffness with a fixed 25 lb test load, he was not able to distinguish between the infinitesimal stiffness of the wheel and the nonlinear deflection due to potentially buckled spokes.

The industry blog, Roues Artisanales [1] (affiliated with RAR, manufacturer of high-end wheels and components) has published a number of investigations on wheels, mostly involving lateral stiffness. As part

of their “Great Wheel Test,” they published lateral and radial stiffnesses of 44 wheels. They performed some systematic tests with some wheel parameters held constant to determine the effects of spoke count, spoke diameter, and spoke tension. They have not compared these results with theory.

1.4. Outline of this thesis

The purpose of this thesis is to develop a consistent theoretical framework for stress analysis of the bicycle wheel. The solutions by Smith and Pippard emerge as special cases within this framework. In Chapter 2, I develop the analysis framework and use it for stress analysis of the wheel under external loads. In Chapter 3, I demonstrate an experimental method for determining rim stiffness parameters necessary for theoretical analysis. In Chapter 4, I show that the equations developed in Chapter 2 lead to an elastic instability of the wheel under spoke tension, and derive equations for the critical tension under several approximations. In Chapter 5, I analyze buckling failure of the wheel under external loads and derive an approximate formula for the critical radial load based on a simplified model of the wheel. The theory accurately predicts the radial strength of a bicycle wheel tested in a custom compression machine and offers insight into the competing failure modes involved in wheel collapse. Finally, in Chapter 6, I use the models derived in this thesis to design wheels optimized for specific performance parameters.

CHAPTER 2

Linear stress analysis

2.1. Kinematics and strain energy

A schematic of a typical bicycle wheel is shown in Fig. 2.1. The structure consists of a hub, rim, and spokes. The spokes are connected to two parallel flanges on the hub and the resulting projected bracing angle, α , stabilizes the rim laterally. Since the introduction of the tangent-spoked wheel by Starley in 1874 [34], the spokes on most wheels are inclined by an angle β in the plane of the rim relative to the radial vector in order to efficiently transmit torque between the hub and rim. Conventional spokes are threaded into nipples set into the rim which can be tightened and loosened independently. The spokes are tensioned during construction to prevent them from buckling when the wheel carries load. Bicycle rims today are

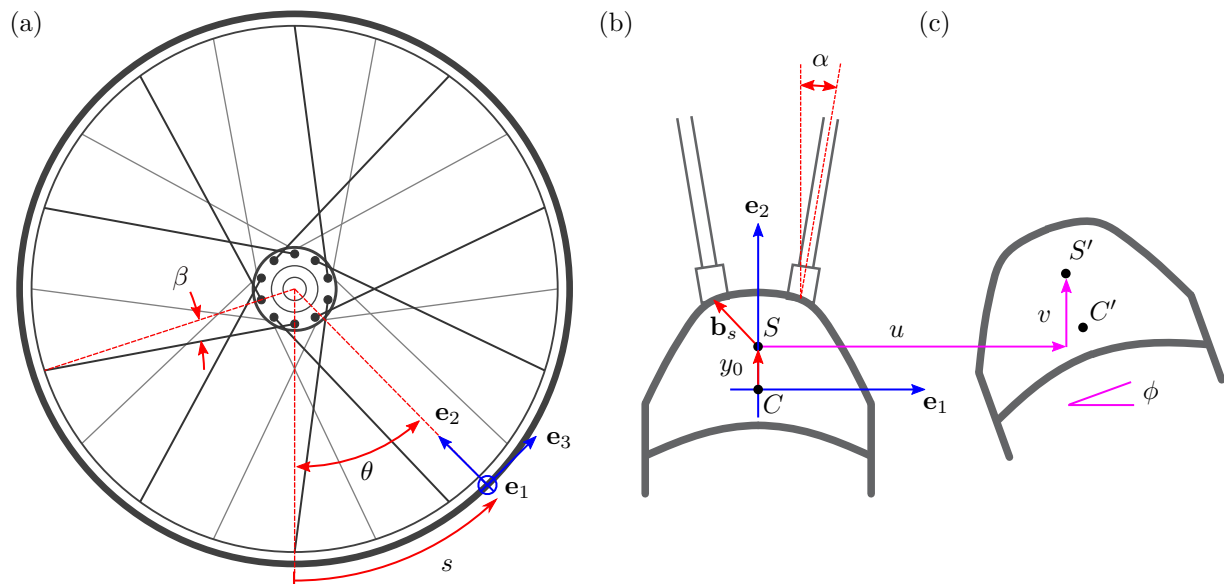


Figure 2.1. Schematic of a typical bicycle wheel. (a) Side view, looking at the hub. (b) Rim cross-section showing local coordinate system at the centroid and vector spoke offset \mathbf{b}_s . (c) Rim cross-section after deformation. Tangential displacement w is not shown.

typically constructed from thin-walled extruded sections, while rims on older bicycles were constructed from roll-formed metal strip or solid wood.

To describe forces and deformations of a wheel, we employ a local coordinate triad whose origin is at the cross-section centroid, C . The basis vector \mathbf{e}_2 points radially inwards, the basis vector \mathbf{e}_3 points in the circumferential direction of increasing arc length s , and the lateral basis vector \mathbf{e}_1 completes a right-hand triad.

2.1.1. Deformation of the rim

The rim is modeled as a circular beam with a constant, thin-walled cross-section having an axis of symmetry in the plane of the wheel. I adopt the standard Euler-Bernoulli assumptions:

- (1) The material behavior is linear-elastic.
- (2) The cross-section is rigid with respect to in-plane deformation, except for out-of-plane warping deformation.
- (3) Shear deformations can be neglected, except that associated with uniform torsion.
- (4) Displacements and rotations are infinitesimal.

We first compute the continuum displacement field in the rim based on assumptions (2) and (3). Due to assumption (2), the displacement at any point in the cross-section is given by a rigid-body displacement of a suitable reference point, a rigid-body rotation about that reference point, followed by a normal displacement given by the rate-of-twist curvature multiplied by the normalized warping function [85]. For a monosymmetric beam, the most convenient reference point is the shear center, which is the unique point in the rim cross-section at which an applied shear load produces no twist¹. Due to assumption (4), these operations can be applied in any order.

¹For an introduction to torsion of thin-walled beams, see Barber [7].

After deformation, each point in the body displaces by \mathbf{u} and the basis vectors $\mathbf{e}_1, \mathbf{e}_2, \mathbf{e}_3$ rotate through angles $\omega_1, \omega_2, \omega_3$. The displacement vector at a point $(x, y, 0)$ in the cross-section is given by

$$(2.1) \quad \mathbf{u} = \mathbf{u}_s + \left[\left(\phi' - \frac{u'}{R} \right) \alpha_s \right] \mathbf{e}_3 + \begin{bmatrix} 0 & -\omega_3 & \omega_2 \\ \omega_3 & 0 & -\omega_1 \\ -\omega_2 & \omega_1 & 0 \end{bmatrix} \begin{bmatrix} x \\ y - y_0 \\ 0 \end{bmatrix}$$

where $\mathbf{u}_s = u\mathbf{e}_1 + v\mathbf{e}_2 + w\mathbf{e}_3$ is the displacement of the shear center, α_s is the normalized warping function defined at the shear center, and y_0 is the height of the shear center relative to the centroid. The infinitesimal rotation angles are given by

$$(2.2a) \quad \omega_1 = v' + w/R$$

$$(2.2b) \quad \omega_2 = u'$$

$$(2.2c) \quad \omega_3 = \phi$$

The deformation curvature κ is found by differentiating the rotation vector ω with respect to s , making use of the Frenet-Serret formulas: $\mathbf{e}'_2 = -\mathbf{e}_3/R$ and $\mathbf{e}'_3 = \mathbf{e}_2/R$. The result is:

$$(2.3a) \quad \kappa_1 = \left(v'' + \frac{w'}{R} \right)$$

$$(2.3b) \quad \kappa_2 = \left(u'' + \frac{\phi}{R} \right)$$

$$(2.3c) \quad \kappa_3 = \left(\phi' - \frac{u'}{R} \right)$$

We recognize these three components as the in-plane bending curvature, out-of-plane bending curvature, and twist. For understanding rim deformation, it is worth remarking that $\phi = \text{constant}$ creates pure bending (ring eversion), while $u' = \text{constant}$ creates pure torsion (analogous to a helical spring) [58].

2.1.1.1. Strain-displacement relations. The longitudinal strain at each point in the body is computed from the displacement field (2.1). In cylindrical coordinates:

$$(2.4) \quad \begin{aligned} \varepsilon_{33} &= u_3' - \frac{1}{R}u_2 \\ &= w' - \frac{v}{R} - x \left(u'' + \frac{\phi}{R} \right) + (y - y_0) \left(v'' + \frac{w'}{R} \right) + \left(\phi'' - \frac{u''}{R} \right) \alpha_s \end{aligned}$$

The longitudinal strain distribution in (2.4) is identical to the linear part of the longitudinal strain derived by Trahair and Papangelis [87], and Pi, et. al. [64]. In deriving (2.4), it is assumed that the initial curvature $1/R$ is constant across the cross-section. For most bicycle rims, for which the ratio of rim radius to cross-section height typically exceeds 20, this is an excellent approximation. For very deep rims, (2.4) must be multiplied by the curvature factor $R/(R + y)$, which greatly complicates integration of the section [41, 48, 72].

The non-vanishing shear strain associated with uniform torsion is given by [64, 41]:

$$(2.5) \quad \gamma = 2\xi \left(\phi' - \frac{u'}{R} \right)$$

where ξ is the normal distance from the midplane of the thin-walled section. The shear direction is directed normal to the thickness direction of the local section. Equation (2.5) is appropriate for cross-sections assembled from multiple open and closed thin-walled profiles (which includes the vast majority of bicycle rims). An expression suitable for general, symmetrical bodies neglecting the curvature correction $R/(R + y)$ is given by Pi, et. al. [9]:

$$(2.6a) \quad \gamma_{31} = - \left(y + \frac{\partial \alpha_s}{\partial x} \right) \left(\phi' - \frac{u'}{R} \right)$$

$$(2.6b) \quad \gamma_{32} = \left(x + \frac{\partial \alpha_s}{\partial y} \right) \left(\phi' - \frac{u'}{R} \right)$$

In general, determining the warping function α_s for an arbitrary cross-section is difficult and must be obtained numerically [85].

2.1.1.2. Strain energy. Making use of assumption (1), the strain energy in the rim due to the linearized displacement field is given by

$$(2.7) \quad U_{rim} = \frac{1}{2} \int_0^{2\pi R} \int_A (E\varepsilon_{33}^2 + G\gamma^2) dA ds$$

where E and G are the Young's modulus and shear modulus, respectively. Substituting (2.4) and (2.5) into (2.7) and integrating over the rim cross-section yields

$$(2.8) \quad U_{rim} = \frac{1}{2} \int_0^{2\pi R} EA \left(w' - \frac{v}{R} - y_0 \left(v'' + \frac{w'}{R} \right) \right)^2 + EI_1 \left(v'' + \frac{w'}{R} \right)^2 + EI_2 \left(u'' + \frac{\phi}{R} \right)^2 + EI_w \left(\phi'' - \frac{u''}{R} \right)^2 + GJ \left(\phi' - \frac{u'}{R} \right)^2 ds$$

Equation (2.8) is derived with the help of the following relations:

$$(2.9) \quad \int x dA = \int y dA = \int xy dA = 0$$

$$(2.10) \quad \int dA = A, \quad \int x^2 dA = I_2, \quad \int y^2 dA = I_1, \quad \int 4\xi^2 dA = J, \quad \int \alpha_s^2 dA = I_w$$

Noting that the longitudinal strain at the centroid is given by $\varepsilon_c = w' - v/R - y_0(v'' + w'/R)$ and substituting the curvatures (2.3) into (2.8), we obtain

$$(2.11) \quad U_{rim} = \frac{1}{2} \int_0^{2\pi R} EA\varepsilon_c^2 + EI_1\kappa_1^2 + EI_2\kappa_2^2 + GJ\kappa_3^2 + EI_w(\kappa_3')^2 ds$$

2.1.1.3. Strain energy in a general deformed configuration. Any general deformation of the bicycle wheel may be represented as a transition from an unstressed state \mathcal{S}_0 to a prestressed state \mathcal{S}_p , and then to a deformed state \mathcal{S}_d . The total displacement field is given by

$$(2.12) \quad \mathbf{u} = \mathbf{u}_p + \delta\mathbf{u}$$

where \mathbf{u}_p is the displacement field for $\mathcal{S}_0 \rightarrow \mathcal{S}_p$ and $\delta\mathbf{u}$ is the displacement field for $\mathcal{S}_p \rightarrow \mathcal{S}_d$. Inserting (2.12) into (2.11) and adopting the same notation conventions for the prestressed and deformed

configurations, we obtain

$$(2.13) \quad U_{rim} = U_{rim}^p + \delta U_{rim}^{p\delta} + U_{rim}^\delta$$

where U_{rim}^p is the strain energy due to \mathbf{u}_p alone, U_{rim}^δ is the strain energy due to $\delta\mathbf{u}$ alone, and the cross-term is defined as

$$(2.14) \quad \delta U_{rim}^{p\delta} = \int_0^{2\pi R} EA\varepsilon_c^p \delta\varepsilon_c + EI_1\kappa_1^p \delta\kappa_1 + EI_2\kappa_2^p \delta\kappa_2 + GJ\kappa_3^p \delta\kappa_3 + EI_w(\kappa_3^p)' \delta\kappa_3' ds$$

This term is the first variation of the strain energy U_{rim} in the prestressed configuration with respect to a virtual displacement $\delta\mathbf{u}$.

2.1.2. Deformation of the spoke system

The behavior of the spokes conforms to the following assumptions:

- (1) The material behavior is linear-elastic.
- (2) Each spoke is an ideal bar which only deforms along its length.
- (3) The connections between the spoke and the hub and rim behave as ideal moment-free ball joints.

As a consequence of (2) and (3), the force exerted on the spoke by the rim is given by

$$(2.15) \quad \mathbf{f} = -T\mathbf{n}$$

where T is the instantaneous tension in the spoke, and \mathbf{n} is the unit vector pointing from the spoke nipple to the hub connection point. As a consequence of (1), the strain energy in a single spoke is equal to the work done by a force \mathbf{f} applied to the spoke nipple. The strain energy in the deformed configuration can be decomposed into the work done in moving from the unstressed configuration \mathcal{S}_0 to the prestressed

configuration \mathcal{S}_p , and then from the prestressed configuration to the deformed configuration \mathcal{S}_d .

$$\begin{aligned}
(2.16) \quad U_{spoke} &= \int_{\mathcal{S}_0}^{\mathcal{S}_d} \mathbf{f} \cdot d\mathbf{u}_n \\
&= \int_{\mathcal{S}_0}^{\mathcal{S}_p} \mathbf{f} \cdot d\mathbf{u}_n + \int_{\mathcal{S}_p}^{\mathcal{S}_d} (\mathbf{f}_p + \delta\mathbf{f}) \cdot d\mathbf{u}_n \\
&= U_{spoke}^p + \mathbf{f}_p \cdot \delta\mathbf{u}_n + \int_0^{\delta\mathbf{u}_n} \delta\mathbf{f} \cdot d\mathbf{u}_n \\
&= U_{spoke}^p + \mathbf{f}_p \cdot \delta\mathbf{u}_n + U_{spoke}^\delta
\end{aligned}$$

where \mathbf{f}_p is the force on the spoke in the prestressed configuration and $\delta\mathbf{f}$ is the incremental force in moving to the deformed configuration. I assume that the incremental displacement $\delta\mathbf{u}_n$ is small enough such that $\delta\mathbf{f}$ can be linearized with respect to $\delta\mathbf{u}_n$.

The displacement $\delta\mathbf{u}_n$ can be decomposed into a component parallel to the spoke axis and a component transverse to the spoke axis. The parallel component leads to a force change in the axial direction $K_s\delta u_{n\parallel}$, where K_s is the axial stiffness of the spoke (the *material stiffness*). The transverse component produces a net restoring force in the transverse direction of $(T_p/l_s)\delta u_{n\perp}$ due to the rotation of the spoke through an infinitesimal angle $\delta u_{n\perp}/l_s$, where l_s is the spoke length. This is the same effect (tension stiffness, membrane stiffness, or *geometric stiffness*) which gives a tensed string or thin, taut membrane its transverse stiffness. Taking the vector sum of these components gives

$$(2.17) \quad \delta\mathbf{f}_s = K_s(\delta\mathbf{u}_s \cdot \mathbf{n})\mathbf{n} + \left(\frac{T_p}{l_s}\right) ((\delta\mathbf{u}_n \cdot \mathbf{n}_{\perp 1})\mathbf{n}_{\perp 1} + (\delta\mathbf{u}_n \cdot \mathbf{n}_{\perp 2})\mathbf{n}_{\perp 2})$$

where \mathbf{n} is the spoke vector in the prestressed configuration, and $\mathbf{n}_{\perp 1}, \mathbf{n}_{\perp 2}$ complete an orthonormal triad. Using the identity that $\mathbf{n} \otimes \mathbf{n} + \mathbf{n}_{\perp 1} \otimes \mathbf{n}_{\perp 1} + \mathbf{n}_{\perp 2} \otimes \mathbf{n}_{\perp 2} = \mathbf{I}$, we obtain the spoke force stiffness tensor:

$$(2.18) \quad \mathbf{k}_f = \mathbf{k}_f^{matl} + \mathbf{k}_f^{geom} = K_s\mathbf{n} \otimes \mathbf{n} + \frac{T_p}{l_s}(\mathbf{I} - \mathbf{n} \otimes \mathbf{n})$$

such that $\delta\mathbf{f}_s = \mathbf{k}_f\delta\mathbf{u}_n$. The tensor product (or dyadic product) $\mathbf{n} \otimes \mathbf{n}$ of two vectors is conveniently calculated in matrix form by the matrix product $\mathbf{n}\mathbf{n}^T$, where \mathbf{n} is a column vector and $()^T$ denotes the matrix transpose.

The displacement of the spoke nipple $\delta \mathbf{u}_n$ is related to the displacement of the shear center $\delta \mathbf{u}_s$ through Eqn. (2.1), where the vector $[x, y - y_0, 0]^T = \mathbf{b}_s$. In general, Eqn. (2.1) leads to a displacement with components in the $\mathbf{e}_1, \mathbf{e}_2, \mathbf{e}_3$ directions, where the $\mathbf{e}_1, \mathbf{e}_2$ displacements are proportional to $\delta \phi$ and the \mathbf{e}_3 displacement depends on gradients of $\delta \mathbf{u}_s$. The \mathbf{e}_3 displacement will have a small contribution to the strain energy (2.16) due to the small tangential projection of the spokes. Furthermore, wheels with spokes significantly offset from the shear center tend to have wide, shallow rims, meaning that the spoke offset vector \mathbf{b}_s has a large \mathbf{e}_1 component and a small \mathbf{e}_2 component. Therefore I use a simplified version of (2.1) dropping the \mathbf{e}_3 displacement.

$$(2.19) \quad \delta \mathbf{u}_n = \delta \mathbf{u}_s + \phi(\mathbf{e}_3 \times \mathbf{b}_s)$$

Substituting Eqns. (2.17), (2.18), and (2.19) into (2.16) gives

$$(2.20) \quad U_{spoke}^\delta = \frac{1}{2}(\delta \mathbf{u}_s \mathbf{k}_f \delta \mathbf{u}_s) + \phi(\mathbf{b}_s \times \mathbf{e}_3) \mathbf{k}_f \delta \mathbf{u}_s + \frac{1}{2} \phi^2 (\mathbf{e}_3 \times \mathbf{b}_s) \mathbf{k}_f (\mathbf{e}_3 \times \mathbf{b}_s)$$

Next we define an augmented shear center displacement vector and augmented spoke stiffness matrix:

$$(2.21) \quad \mathbf{d} = [\delta u, \delta v, \delta w, \phi]^T$$

$$(2.22) \quad \mathbf{k} = \begin{bmatrix} \mathbf{k}_f & \mathbf{k}_f(\mathbf{e}_3 \times \mathbf{b}_s) \\ (\mathbf{e}_3 \times \mathbf{b}_s) \mathbf{k}_f & (\mathbf{e}_3 \times \mathbf{b}_s) \mathbf{k}_f (\mathbf{e}_3 \times \mathbf{b}_s) \end{bmatrix}$$

Substituting (2.21) and (2.22), and (2.20) into (2.16) and summing over all the spokes, the total strain energy in the spoke system becomes

$$(2.23) \quad U_{spokes} = U_{spokes}^p + \sum_i^{n_s} \left(\mathbf{f}_p^i \cdot \delta \mathbf{u}_n^i + \frac{1}{2} \mathbf{d}_i^T \mathbf{k}^i \mathbf{d}_i \right)$$

2.1.3. Smearred spokes approximation

Equation (2.23) is not amenable to analytical solutions because it requires evaluation of the displacement field at discrete points. Following the approach of Smith [78] and Pippard [66], I approximate the third term in Eqn. (2.23) by replacing the discrete spokes with a continuous elastic foundation, matching the averaged

stiffness per unit length along the rim. The continuous analog of Eqn. (2.22) is obtained by averaging the components of the spoke stiffness matrices in cylindrical coordinates and dividing by the circumference of the rim:

$$(2.24) \quad \bar{\mathbf{k}} = \frac{1}{2\pi R} \sum_i^{n_s} \mathbf{k}_i$$

The incremental strain energy in the spoke system from the prestressed configuration to the deformed configuration is then approximated by

$$(2.25) \quad \bar{U}_{spokes}^\delta = \frac{1}{2} \int_0^{2\pi R} \mathbf{d}^T \bar{\mathbf{k}} \mathbf{d} ds$$

What information is lost in this smeared approach? An actual wheel in which 32 spokes of diameter 2 mm were replaced by 3200 spokes of diameter 0.2 mm will have some differences in behavior. Most obviously, if a solution based on smeared spokes exhibits length scales comparable to spoke spacing, such solutions would not be expected to be accurate for the realistic wheel. This problem appears most particularly for concentrated radial loads, where the affected length includes very few spokes. The affected length for a straight beam on an elastic foundation is $2(4EI_1/\bar{k}_{vv})^{1/4}$ [37]. Provided that this length is much less than the radius of the wheel, the straight beam approximation is sufficiently accurate for assessing the validity of the smeared-spokes approximation. The number of spokes within the affected length (twice the characteristic length scale), defined here as the Smith-Pippard number, is

$$(2.26) \quad n_{SP} = \frac{n_s}{\pi R} \left(\frac{4EI_1}{\bar{k}_{vv}} \right)^{1/4}$$

Figure 2.2 (a) shows the radial stiffness calculated with and without the smeared-spokes approximation for wheels with different numbers of spokes but the same total spoke cross-sectional area $n_s A_s$. The smeared-spokes approximation always gives a lower stiffness than the true stiffness. As long as there is more than one spoke in the affected length, the smeared-spokes approximation is quite accurate. The affected length is longer for lateral loads, and significantly longer for tangential loads, and accurate solutions may be obtained in these cases even when the spoke density is not high enough for calculating radial displacements.

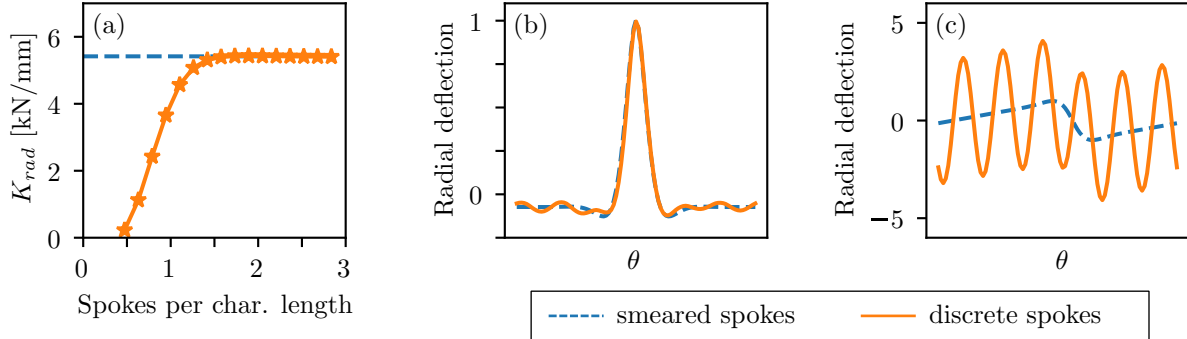


Figure 2.2. Comparison of results using smeared spokes and discrete spokes. **(a)** Radial stiffness wheels with identical total spoke cross-sectional area $n_s A_s$, but different numbers of spokes. **(b)** Normalized radial displacement under a radial load for a 24-spoke wheel calculated with and without the smeared-spokes approximation. **(c)** Normalized radial displacement under lateral load (braking or accelerating) for the same wheel. The displacements in (b) and (c) are normalized such that the maximum radial displacement from the smeared-spokes approximation is 1.

Perhaps the most surprising effect of discrete spokes has to do with local coupling between radial, lateral, and tangential displacements and forces, which is lost when the spoke stiffness is homogenized [58]. Since spokes are not purely radial in a tangent-spoke wheel, an inward motion at the end of one spoke will actually give rise to lateral and tangential reaction forces on the rim. The very next spoke, under a similar deformation, will switch signs of the lateral or tangential reaction. So one result is that a concentrated radial load gives rise to both tangential and lateral displacement at the same point, and vice-versa. Furthermore, whenever a loading gives rise to displacements around the entire wheel, those displacements give rise to period-four sinusoidally varying radial, tangential, and lateral loads. Thus one observes small-scale sinusoidal variations in spoke tension or rim deflection around the entire wheel, as illustrated in Fig. 2.2. Although this variation is small compared with the peak deflection under radial load, the difference is significant under tangential load. Such behavior is entirely suppressed by the smeared stiffness approach. Three-dimensional finite-element analysis—which preserves the discrete nature of the spokes—will accurately capture these effects [73].

2.1.4. Spoke stiffness $\bar{\mathbf{k}}$ for common wheel configurations

In the most general case, $\bar{\mathbf{k}}$ is a symmetric, positive-definite matrix with 10 unique entries. For many wheels of practical interest, some of these entries may be identically or approximately zero. Spoke stiffness matrices are given for some common wheel configurations below. The geometric terms are calculated in terms of the direction cosines for a left leading (or “pushing”) spoke, $\mathbf{n}_p = [c_1, c_2, c_3]^T$. The sign of c_1 will alternate for left and right spokes while c_3 will alternate for leading and trailing spokes.

Left-right symmetric, radial-spoked wheel with no spoke offset. The front wheel on most bicycles is symmetric across the plane of the wheel (modulo a rotation by one spoke about the axle). If the spokes are radial, as is common on high-end road bikes with rim brakes, the stiffness matrix takes a very simple form:

$$(2.27) \quad \bar{\mathbf{k}} = \frac{n_s K_s}{2\pi R} \begin{bmatrix} c_1^2 & 0 & 0 & 0 \\ 0 & c_2^2 & 0 & 0 \\ 0 & 0 & 0 & 0 \\ 0 & 0 & 0 & 0 \end{bmatrix} + \frac{n_s T_p}{2\pi R l_s} \begin{bmatrix} 1 - c_1^2 & 0 & 0 & 0 \\ 0 & 1 - c_2^2 & 0 & 0 \\ 0 & 0 & 1 & 0 \\ 0 & 0 & 0 & 0 \end{bmatrix}$$

For typical wheel dimensions, $c_2 \approx 1$ and $c_1^2 \ll c_2^2$.

Left-right symmetric, radial spokes with offset nipples. If the spokes are significantly offset from the shear center by a lateral distance $\pm b_1$ as is now common for “fat bike” wheels, but the left-right symmetry of the previous case is retained, lateral-torsional coupling terms are introduced:

$$(2.28) \quad \bar{\mathbf{k}} = \frac{n_s K_s}{2\pi R} \begin{bmatrix} c_1^2 & 0 & 0 & c_1 c_2 b_1 \\ 0 & c_2^2 & 0 & 0 \\ 0 & 0 & 0 & 0 \\ c_1 c_2 b_1 & 0 & 0 & c_2^2 b_1^2 \end{bmatrix} + \frac{n_s T_p}{2\pi R l_s} \begin{bmatrix} 1 - c_1^2 & 0 & 0 & -c_1 c_2 b_1 \\ 0 & 1 - c_2^2 & 0 & 0 \\ 0 & 0 & 1 & 0 \\ -c_1 c_2 b_1 & 0 & 0 & (1 - c_2^2) b_1^2 \end{bmatrix}$$

It is interesting to note that although the elastic component of the (u, v, w) sub-matrix has strictly positive eigenvalues, one of the eigenvalues of the elastic component of the (u, ϕ) sub-matrix vanishes identically.

This can be seen by computing the determinant:

$$(2.29) \quad (1 - c_1^2)(1 - c_2^2)b_1^2 - c_1^2 c_2^2 b_1^2 = b_1^2(1 - c_1^2 - c_2^2) = 0$$

where the last step is made by noting that c_1 and c_2 are direction cosines (and $c_3 = 0$). The consequence of this zero-eigenvalue is that there exists a combination of lateral and torsional motion of the rim for which the spokes and rim cross-section rotate as a rigid linkage and offer no resistance².

Left-right symmetric, tangent spokes. The spokes on most bicycles are attached roughly tangent to the hub to confer rotational stiffness. The left-right symmetry extinguishes the $u - v$ coupling and the leading-trailing symmetry extinguishes the $v - w$ coupling, but a tangential term appears in the material stiffness.

$$(2.30) \quad \bar{\mathbf{k}} = \frac{n_s K_s}{2\pi R} \begin{bmatrix} c_1^2 & 0 & 0 & 0 \\ 0 & c_2^2 & 0 & 0 \\ 0 & 0 & c_3^2 & 0 \\ 0 & 0 & 0 & 0 \end{bmatrix} + \frac{n_s T_p}{2\pi R l_s} \begin{bmatrix} 1 - c_1^2 & 0 & 0 & 0 \\ 0 & 1 - c_2^2 & 0 & 0 \\ 0 & 0 & 1 - c_3^2 & 0 \\ 0 & 0 & 0 & 0 \end{bmatrix}$$

The stiffness matrix for an asymmetrically-dished wheel with tangent spokes is given in Appendix A.

2.2. Stresses and deformation of the pretensioned wheel

In the absence of external loads, the bicycle rim is loaded primarily radially loaded by the system of spokes. The rim shrinks due to the compressive hoop stress induced by the pull of the spokes and bows inwards at each spoke due to the bending moment introduced by the spacing between spokes. The average radial tension per unit length exerted by the spokes is

$$(2.31) \quad \bar{T} = \frac{1}{2\pi R} \sum_i^{n_s} T_p^i \mathbf{n}_p^i \cdot \mathbf{e}_2$$

For simplicity, we will consider a wheel with purely radial, uniformly-tensioned spokes. Consider the unit cell containing a single spoke, as shown in Fig. 2.3 (a). By symmetry, the axial force and moment must be equal at the two ends. Equilibrium of forces in the horizontal direction immediately requires $F_2 = 0$.

²See Section 2.6.3

Sum of forces in the vertical direction gives

$$(2.32) \quad F_3 = \frac{\pi R \bar{T}}{n_s \sin(\pi/n_s)} \approx R \bar{T}$$

where the second result, first derived by Sharp [77], is obtained by noting that $\sin \pi/n_s \approx \pi/n_s$ for sufficiently large n_s . The internal forces F_3', F_2', M_1' at an arbitrary section at $\theta < \pi/n_s$ are obtained from equilibrium of the segment shown in Fig. 2.3 (a).

$$(2.33a) \quad F_3' = R \bar{T} \cos \theta$$

$$(2.33b) \quad F_2' = R \bar{T} \sin \theta$$

$$(2.33c) \quad M_1' = M_1 + R^2 \bar{T} (1 - \cos \theta)$$

Following our previous assumption that shear deformations are negligible, the strain energy in terms of internal forces is

$$(2.34) \quad U = 2 \int_0^{\pi/n_s} \left(\frac{(M_1')^2}{2EI_1} + \frac{(F_3')^2}{2EA} \right) R d\theta$$

The strain energy is composed of U_{EA} , the strain energy due to hoop stress and U_{EI} , the strain energy due to bending. The unknown end moment M_1 is determined from the condition that there can be no rotation of the cross-section at the symmetry point between spokes. By Castigliano's method, the rotation at the point where M_1 is applied is given by $\partial U / \partial M_1$. Setting $\partial U / \partial M_1 = 0$ and solving for M_1 allows us to eliminate M_1 in Eqn. (2.33c):

$$(2.35) \quad M_1' = R^2 \bar{T} \left(\frac{\sin \pi/n_s}{\pi/n_s} - \cos \theta \right)$$

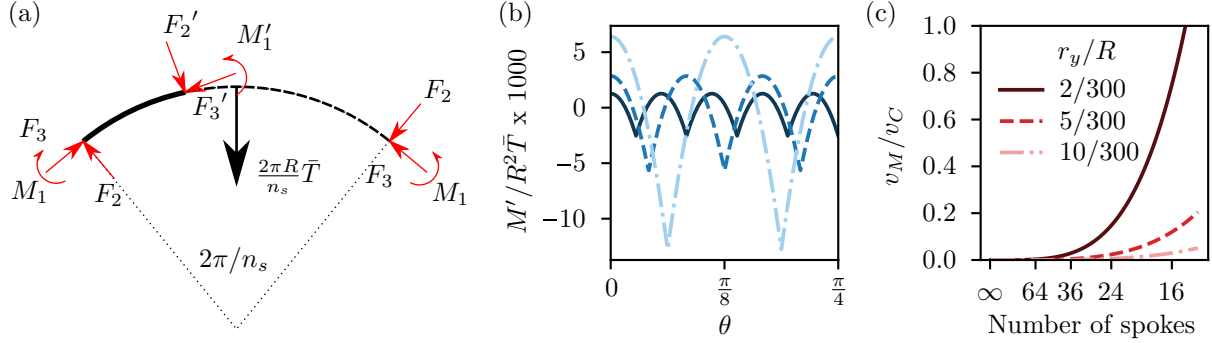


Figure 2.3. Radial deformation of the wheel under uniform tension. (a) Segment of rim containing a single spoke. (b) Bending moment induced by radial spoke pull. solid line = 36 spokes, dashed line = 24, dot-dash line = 16. (c) Ratio of deflection at a spoke due to bending and due to circumferential shrinkage.

Castigliano's method can then be used to determine the displacement at the spoke due to axial compression alone and bending alone. Noting that $T = (2\pi/n_s)\bar{T}$:

$$(2.36) \quad v_C = \frac{\partial U_{EA}}{\partial T} = \frac{R^2 \bar{T}}{2EA} \left(\left(\frac{\pi/n_s}{\sin \pi/n_s} \right)^2 + \frac{\pi/n_s}{\tan \pi/n_s} \right) \approx \frac{R^2 \bar{T}}{EA}$$

$$(2.37) \quad v_M = \frac{\partial U_{EI}}{\partial T} = \frac{R^4 \bar{T}}{2EI_1} \left(\left(\frac{\pi/n_s}{\sin \pi/n_s} \right)^2 + \frac{\pi/n_s}{\tan \pi/n_s} - 2 \right)$$

The relative contribution of v_M is generally very small compared to v_C . Retaining only the first non-vanishing term in the Taylor series for v_M/v_C in terms of π/n_s , we obtain a very close approximation $v_M/v_C \approx (1/45)(R/r_y)^2(\pi/n_s)^4$, where r_y is the radius of gyration of the rim in the radial direction. Bending deformations become significant only if the number of spokes is very low or the rim radial bending stiffness is very small. Low spoke-count wheels generally have very deep cross-sections to minimize bending deformation between spokes.

2.3. Total potential energy of the deformed wheel

2.3.1. Total strain energy and equilibrium constraint

The total strain energy of the combined rim and spokes system is given by the sum of Eqns. (2.13) and (2.23):

$$(2.38) \quad U_{rim} + U_{spokes} = U_{rim}^p + \delta U_{rim}^{p\delta} + U_{rim}^\delta + U_{spokes}^p + \sum_i^{n_s} \left(\mathbf{f}_p^i \cdot \delta \mathbf{u}_n^i + \frac{1}{2} \mathbf{d}_i^T \mathbf{k}_i \mathbf{d}_i \right)$$

The prestressed configuration \mathcal{S}_p is already in static equilibrium, thus the first variation of the total potential energy of the rim must vanish. This gives rise to the constraint equation³

$$(2.39) \quad \delta \Pi^{p\delta} = \delta U_{rim}^{p\delta} + \sum_i^{n_s} \mathbf{f}_p^i \cdot \delta \mathbf{u}_n^i = 0$$

2.3.2. Virtual work of internal forces

Equation (2.38) was derived under the assumption that the rotations of the beam cross-section are small enough that the infinitesimal rotation tensor may be used in (2.1). If a second-order approximation to the rotation tensor is used, the strain-displacement relation (2.4) must be augmented by additional non-linear terms. These strains give rise to couplings between the internal stresses in the prestressed configuration and the incremental displacement $\delta \mathbf{u}, \delta \phi$ which reduce the total strain energy. Though a full derivation of these terms is beyond the scope of this work, there is considerable literature on out-of-plane stability of arches which is relevant to prestressed bicycle rims (the rim can be treated as a special case of an arch for which the subtended angle is 2π).

The literature on stability of curved beams has been reviewed broadly by Pi et. al. [63]. Timoshenko and Gere [85] studied the stability of arches under uniform compression and uniform radial bending from the equilibrium of a deformed arch segment. A similar approach was used by Vlasov [88]. The energy method has been used by far more researchers [91, 87, 65, 41, 64, 48, 72] due to the simplicity of deriving the strain energy from an appropriate approximation for the strain field. This method has been extended

³The force applied to a spoke by the rim \mathbf{f}_p^i is equal and opposite to the force applied to the rim by the spoke, hence the positive sign in Eqn. (2.39).

to investigate special cases including laterally fixed rings [84], arches with discrete and continuous elastic restraints [62, 8], and elastic end restraints.

In order to accurately capture the flexural-torsional buckling phenomenon in bicycle wheels, I adopt the following assumptions:

- (1) The prestressed configuration \mathcal{S}_p can be described by the shear-center displacement field $\mathbf{d}_p = [0, v_p, w_p, 0]^T$.
- (2) The non-uniform in-plane and out-of-plane bending moments M_1 and M_2 are negligible.
- (3) In moving from the prestressed configuration to the deformed configuration \mathcal{S}_d , the non-linear variations of the radial and tangential displacements can be neglected, i.e. only the non-linear variations of δu and $\delta\phi$ will be considered. The linear variations δv and δw have already been accounted for in the strain energy given above.
- (4) The 3rd-order and higher terms involving the initial displacements v_p, w_p can be neglected.

Assumptions (1) and (2) result from neglecting the discrete nature of the spokes in the prestressing system. As shown in Section 2.2, the periodic variation in the radial displacement is generally much smaller than the uniform contraction of the rim under compression. A similar argument justifies neglecting the periodically-varying lateral displacement and twist between spokes.

Assumption (3) is a consequence of the large difference in radial and lateral stiffness of the bicycle wheel (the radial stiffness is generally about two orders of magnitude larger). The spoke stiffness for purely radial spokes is proportional to $\cos^2 \alpha$, while the lateral stiffness is proportional to $\sin^2 \alpha$. The possibility of in-plane buckling modes—such as those present in a prestressed ring with no bracing—is precluded by the large radial stiffness of the spoke system.

Pi, Papangelis, and Trahair [64] show that under the assumptions given above, the strain energy is given by $U_{rim}^{\delta*} = U_{rim}^{\delta} - V_{rim}^{\delta}$, where U_{rim}^{δ} is the strain energy due to the linearized strain given in Section 2.1.1 and V_{rim}^{δ} is given by⁴

$$(2.40) \quad V_{rim}^{\delta} = \frac{1}{2} \int_0^{2\pi R} F_3 \left[(\delta u')^2 + r_0^2 \left(\delta\phi' - \frac{\delta u'}{R} \right)^2 + y_0 \left(2\delta u' \delta\phi' - \frac{\delta\phi^2}{R} \right) \right] ds$$

⁴See Eqn. (41) in [64]. In this thesis, the higher-order terms associated with the pre-buckling displacements v_0, w_0 are neglected (Assumption 4).

where $r_0^2 = r_x^2 + r_y^2 + y_0^2$, and $r_x^2 = I_2/A$, $r_y^2 = I_1/A$ are the radii of gyration in the x and y directions. The first term (which has the largest effect on the strain energy) arises due to the change in projected length of a differential element along the beam axis, relative to the undeformed circumferential line. This is the same effect which gives rise to Euler buckling in a straight column. All other formulations reviewed in the literature include this term in an identical form [64, 48, 72, 87, 33, 62].

The second term represents the “Wagner effect,” in which an axial torque produced by finite rotations of axial fibers interacts with the beam twist. This is the effect which causes torsional buckling of a straight column. There are minor differences between authors in this term depending on exactly what approximation is used for the curvature, and at what point in the analysis they discard higher-order terms. Pi, Papangelis, and Trahair [64] calculate the longitudinal strain including the terms $\sin \phi, \cos \phi$, compute the variations, and then discard higher-order terms while Pi and Trahair [65] first approximate $\sin \phi \approx \phi, \cos \phi \approx 1$, and then compute the variations of the strain. Pi, et. al. [63] compared the critical loads for arches resulting from several different formulations and found very minor variations⁵, except in the case of Yoo [91], who approximated the curvature effect by substituting ad-hoc curvature terms into the energy equation for a straight beam.

The third term arises due to the fact that the effective center-of-pressure of the net axial stress is located at the centroid, not the shear center. This term is consistent across the papers reviewed which treat monosymmetric beams [64, 65, 72, 87], except in Pi and Trahair [65], possibly due to an unintended omission or due to the approximations employed. Trahair and Papangelis [87] include the term $2y_0u''\phi$ instead of $2y_0u'\phi'$. However, these terms differ only by a sign change through integration-by-parts, noting that the boundary term vanishes exactly due to periodicity of the rim⁶.

⁵See Fig. 9 in [63]

⁶ $\int u''\phi = [u'\phi] - \int u'\phi'$

2.3.3. Virtual work of external loads and total potential

The rim is loaded by distributed forces f_u, f_v, f_w and a distributed moment m acting at the shear center. The total potential energy in the deformed configuration under this system of loads is

$$(2.41) \quad \Pi = U^p + U_{rim}^\delta + U_{spokes}^\delta - V_{rim}^\delta - \int_0^{2\pi R} (f_u u + f_v v + f_w w + m\phi) ds$$

where the δ symbol has been dropped from the displacements for clarity. Throughout the remainder of this thesis, the un-subscripted displacements u, v, w, ϕ will be taken to mean the incremental displacements from the prestressed configuration to the deformed configuration.

2.4. Equilibrium equations

Equation (2.41) is our starting point for investigating the deformation, stresses, and stability of the prestressed bicycle wheel. As a result of the assumptions already employed, Eqn. (2.41) has a quadratic form suitable for linear-elastic analysis, while an approximation of relevant non-linear effects due to the rim prestress are included in the term V_{rim}^δ . The displacements in the deformed configuration are found by minimizing Eqn. (2.41) with respect to u, v, w, ϕ . The initial strain energy U^p does not depend on u, v, w, ϕ and therefore has no effect on the equilibrium or stability of the wheel.

The rim terms U_{rim}^δ and V_{rim}^δ are already in an integral form suitable for continuum analysis. The spoke term U_{spokes}^δ samples the displacement field at discrete points where the spokes are attached. Therefore in its most general form, Eqn. (2.41) represents a set of non-local elasticity equations for which special solution techniques are required.

2.4.1. Mode stiffness matrix method

One can easily obtain approximate solutions to (2.41) of arbitrary accuracy while preserving the full details of coupling between u, v, w, ϕ by the Rayleigh-Ritz method. Rather than requiring that the first variation of the total potential (2.41) be precisely zero, we construct convenient approximations to the deformation variables u, v, w, ϕ and minimize the resulting approximate total potential function.

We approximate the deformation variables with a finite Fourier series:

$$(2.42) \quad u = u_0 + \sum_{n=1}^N u_n^c \cos n\theta + u_n^s \sin n\theta$$

$$(2.43) \quad v = v_0 + \sum_{n=1}^N v_n^c \cos n\theta + v_n^s \sin n\theta$$

$$(2.44) \quad w = w_0 + \sum_{n=1}^N w_n^c \cos n\theta + w_n^s \sin n\theta$$

$$(2.45) \quad \phi = \phi_0 + \sum_{n=1}^N \phi_n^c \cos n\theta + \phi_n^s \sin n\theta$$

Increasing the maximum mode number N results in higher accuracy. The deformation mode coefficients are collected into a single vector of length $4 + 8N$:

$$(2.46) \quad \mathbf{d}_m = [u_0, v_0, w_0, \phi_0, u_1^c, u_1^s, v_1^c, v_1^s, w_1^c, w_1^s, \phi_1^c, \phi_1^s, u_2^c, u_2^s, \dots]^T$$

The augmented displacement vector $\mathbf{d} = [u, v, w, \phi]^T$ at a point θ is given by

$$(2.47) \quad \mathbf{d} = \mathbf{B}(\theta)\mathbf{d}_m$$

where

$$(2.48) \quad \mathbf{B}(\theta) = \begin{bmatrix} 1 & 0 & 0 & 0 & c\theta & s\theta & 0 & 0 & 0 & 0 & 0 & 0 & c2\theta & s2\theta & \dots \\ 0 & 1 & 0 & 0 & 0 & 0 & c\theta & s\theta & 0 & 0 & 0 & 0 & 0 & 0 & \dots \\ 0 & 0 & 1 & 0 & 0 & 0 & 0 & 0 & c\theta & s\theta & 0 & 0 & 0 & 0 & \dots \\ 0 & 0 & 0 & 1 & 0 & 0 & 0 & 0 & 0 & 0 & c\theta & s\theta & 0 & 0 & \dots \end{bmatrix}$$

where $c\theta = \cos \theta$, $s\theta = \sin \theta$, etc. Inserting the series approximations (2.42) into (2.11) and (2.40) and integrating yields a quadratic form for the strain energy and virtual work of internal forces in the rim:

$$(2.49) \quad \Pi_{rim} = \frac{1}{2} \mathbf{d}_m^T \mathbf{K}_{rim} \mathbf{d}_m$$

where \mathbf{K}_{rim} is the rim mode stiffness matrix. Since the Fourier basis functions are orthogonal on the unit circle, \mathbf{K}_{rim} has the block diagonal structure:

$$(2.50) \quad \mathbf{K}_{rim} = \begin{bmatrix} \mathbf{K}_0^{rim} & & & \\ & \mathbf{K}_1^{rim} & & \\ & & \ddots & \\ & & & \mathbf{K}_N^{rim} \end{bmatrix}$$

The zero-mode matrix is

$$(2.51) \quad \mathbf{K}_0^{rim} = \begin{bmatrix} 0 & 0 & 0 & 0 \\ 0 & 2\pi \frac{EA}{R} & 0 & 0 \\ 0 & 0 & 0 & 0 \\ 0 & 0 & 0 & 2\pi \frac{EI_2}{R} + 2\pi R \bar{T} y_0 \end{bmatrix}$$

The subsequent mode matrices take the form

$$(2.52) \quad \mathbf{K}_{n \geq 1}^{rim} = \begin{bmatrix} k_{uu} & 0 & 0 & 0 & 0 & 0 & -k_{u\phi} & 0 \\ 0 & k_{uu} & 0 & 0 & 0 & 0 & 0 & -k_{u\phi} \\ 0 & 0 & k_{vv} & 0 & 0 & -k_{vw} & 0 & 0 \\ 0 & 0 & 0 & k_{vv} & k_{vw} & 0 & 0 & 0 \\ 0 & 0 & -k_{vw} & 0 & 0 & k_{ww} & 0 & 0 \\ -k_{u\phi} & 0 & 0 & 0 & 0 & 0 & k_{\phi\phi} & 0 \\ 0 & -k_{u\phi} & 0 & 0 & 0 & 0 & 0 & k_{\phi\phi} \end{bmatrix}$$

$$\begin{aligned}
k_{uu} &= \frac{\pi EI_2}{R^3} n^4 + \frac{\pi EI_w}{R^5} n^4 + \frac{\pi GJ}{R^3} n^2 - \pi n^2 \bar{T} \left(1 + \frac{r_0^2}{R^2} \right) \\
k_{vv} &= \frac{\pi EI_1}{R^3} n^4 + \frac{\pi EA}{R} \left(1 + \frac{y_0}{R} n^2 \right)^2 \\
k_{ww} &= \frac{\pi EI_1}{R^3} n^2 + \frac{\pi EA n^2}{R} \left(1 + \frac{y_0}{R} \right)^2 \\
k_{vw} &= \frac{\pi EI_1}{R^3} n^3 + \frac{\pi EA n}{R} \left(1 + \frac{y_0}{R} (1 + n^2) + \frac{y_0^2}{R^2} n^2 \right) \\
k_{\phi\phi} &= \frac{\pi EI_2}{R} + \frac{\pi EI_w}{R^3} n^4 + \frac{\pi GJ}{R} n^2 + \pi R^2 \bar{T} \left(\frac{y_0}{R} - \frac{r_0^2}{R^2} n^2 \right) \\
k_{u\phi} &= \frac{\pi EI_2}{R^2} n^2 + \frac{\pi EI_w}{R^4} n^4 + \frac{\pi GJ}{R^2} n^2 + \pi n^2 R \bar{T} \left(\frac{y_0}{R} - \frac{r_0^2}{R^2} n^2 \right)
\end{aligned}$$

Inserting (2.47) into (2.23) yields the strain energy stored in the spokes:

$$\begin{aligned}
(2.53) \quad U_{spokes} &= \frac{1}{2} \sum_{i=1}^{n_s} \mathbf{d}_i^T \mathbf{k}_i \mathbf{d}_i \\
&= \frac{1}{2} \sum_{i=1}^{n_s} \mathbf{d}_m^T (\mathbf{B}_i^T \mathbf{k}_i \mathbf{B}_i) \mathbf{d}_m \\
&= \frac{1}{2} \mathbf{d}_m^T \left(\sum_{i=1}^{n_s} \mathbf{B}_i^T \mathbf{k}_i \mathbf{B}_i \right) \mathbf{d}_m \\
&= \frac{1}{2} \mathbf{d}_m^T \mathbf{K}_{spk} \mathbf{d}_m
\end{aligned}$$

Due the discrete nature of the spokes, the spoke stiffness matrix \mathbf{K}_{spk} has non-zero elements outside of the block diagonal shown in Eqn. (2.50). If, on the other hand, the smeared-spokes approximation to the strain energy (2.23) is used, then the modes decouple and the strain energy is given by

$$(2.54) \quad \bar{U}_{spokes} = \frac{1}{2} \mathbf{d}_m^T \bar{\mathbf{K}}_{spk} \mathbf{d}_m$$

where the zero-mode block (upper-left 4x4 matrix) is equal to $2\pi R \bar{\mathbf{k}}$. The remaining 8x8 blocks are given by the relation $\bar{\mathbf{K}}_{spk}(2i-1, 2j-1) = \bar{\mathbf{K}}_{spk}(2i, 2j) = \pi R \bar{k}_{ij}$.

If the external loads are given as a series of point loads (and couples), the virtual work of external loads is obtained in a straightforward manner:

$$\begin{aligned}
 V_{ext} &= \sum_{i=1}^{n_f} \mathbf{f}_{ext}^i \cdot \mathbf{d}(\theta_i) \\
 &= \sum_{i=1}^{n_f} \mathbf{f}_{ext}^i \cdot \mathbf{B}_i \mathbf{d}_m \\
 (2.55) \quad &= \left(\sum_{i=1}^{n_f} \mathbf{f}_{ext}^i \mathbf{B}_i \right) \mathbf{d}_m \\
 &= \mathbf{F}_{ext} \mathbf{d}_m
 \end{aligned}$$

Combining Eqns. (2.49), (2.53), and (2.55), the total potential energy is

$$(2.56) \quad \Pi = \frac{1}{2} \mathbf{d}_m^T (\mathbf{K}_{rim} + \mathbf{K}_{spk}) \mathbf{d}_m - \mathbf{F}_{ext} \mathbf{d}_m$$

Minimizing the total potential energy (2.56) with respect to the mode coefficients \mathbf{d}_m yields the modal Rayleigh-Ritz equations:

$$(2.57) \quad (\mathbf{K}_{rim} + \mathbf{K}_{spk}) \mathbf{d}_m = \mathbf{F}_{ext}$$

Equation (2.57) suggests an analogy with the finite-element method, in which the displacement field is approximated with appropriately-constructed shape functions which interpolate the displacements at discrete points throughout the body. By contrast, the mode-matrix method described here approximates the displacement field with a finite set of functions chosen such that the strain energy is approximately additively decomposed. If the smeared-spokes approximation (2.54) is used, the stiffness matrix is guaranteed to have a sparse, block-diagonal form, while still retaining possible coupling (through the spoke geometry) between in-plane and out-of-plane deformations.

2.4.2. Differential equilibrium equations

If the smeared-spokes approximation is employed, the spoke strain energy is converted to an integral form. The Euler-Lagrange equations which guarantee minimization of Eqn. (2.41) give a set of four coupled

differential equations for the displacement variables:

$$(2.58) \quad \begin{bmatrix} \mathcal{D}_{vv} + \bar{k}_{vv} & \mathcal{D}_{vw} + \bar{k}_{vw} & \bar{k}_{uv} & \bar{k}_{v\phi} \\ -\mathcal{D}_{vw} + \bar{k}_{vw} & \mathcal{D}_{ww} + \bar{k}_{ww} & \bar{k}_{uw} & \bar{k}_{w\phi} \\ \bar{k}_{uv} & \bar{k}_{uw} & \mathcal{D}_{uu} + \bar{k}_{uu} & \mathcal{D}_{u\phi} + \bar{k}_{u\phi} \\ \bar{k}_{v\phi} & \bar{k}_{w\phi} & \mathcal{D}_{u\phi} + \bar{k}_{u\phi} & \mathcal{D}_{\phi\phi} + \bar{k}_{\phi\phi} \end{bmatrix} \begin{bmatrix} v \\ w \\ u \\ \phi \end{bmatrix} = \begin{bmatrix} f_v \\ f_w \\ f_u \\ m \end{bmatrix}$$

where

$$\begin{aligned} \mathcal{D}_{vv} &= (EI_1 + EAy_0^2)\mathcal{D}^4 - 2EA\left(\frac{y_0}{R}\right)\mathcal{D}^2 + \frac{EA}{R^2} \\ \mathcal{D}_{ww} &= -\left(\frac{EI_1}{R^2} + EA\left(1 + \frac{y_0}{R}\right)^2\right)\mathcal{D}^2 \\ \mathcal{D}_{vw} &= \left(\frac{EI_1}{R} + EAy_0\left(1 + \frac{y_0}{R}\right)\right)\mathcal{D}^3 - \frac{EA}{R}\left(1 + \frac{y_0}{R}\right)\mathcal{D} \\ \mathcal{D}_{uu} &= \left(EI_2 + \frac{EI_w}{R^2}\right)\mathcal{D}^4 - \frac{GJ}{R^2}\mathcal{D}^2 + RT\left(1 + \frac{r_0^2}{R^2}\right)\mathcal{D}^2 \\ \mathcal{D}_{\phi\phi} &= EI_w\mathcal{D}^4 - GJ\mathcal{D}^2 + \frac{EI_2}{R^2} + Rr_0^2\bar{T}\mathcal{D}^2 + y_0\bar{T} \\ \mathcal{D}_{u\phi} &= -\frac{EI_w}{R}\mathcal{D}^4 + \left(\frac{EI_2}{R} + \frac{GJ}{R}\right)\mathcal{D}^2 + \bar{T}(Ry_0 - r_0^2)\mathcal{D}^2 \end{aligned}$$

and $\mathcal{D}^n \equiv (d/ds)^n$. Due to the spoke stiffness parameters \bar{k}_{ij} , all of the displacement variables appear in each of the equilibrium equations. In the most general case with no further simplifications or symmetries, the combined governing equation is a 14th order linear ordinary differential equation with constant coefficients.

In most cases relevant to real wheels many of the coupling terms $\bar{k}_{ij}(i \neq j)$ are identically zero or are small compared to other relevant quantities. For example, in a wheel with either mirror symmetry or mirror-rotational symmetry across the plane of the wheel, all the off-diagonal terms $\bar{k}_{ij}(i \neq j)$ are identically zero, except $\bar{k}_{u\phi}$. In the case where $\bar{k}_{uv} = \bar{k}_{uw} = \bar{k}_{v\phi} = \bar{k}_{w\phi} = 0$, the equilibrium equations decouple into a pair of equations for radial-tangential deformations and a pair of equations for lateral-torsional deformations. Previous theoretical studies on the bicycle wheel by Smith [78], Pippard, et. al. [66, 67, 68], and Burgoyne and Dilmaghanian [12] were derived by implicitly assuming a decoupled form of (2.58).

2.5. Loads in the plane of the wheel

The radial-tangential equations are

$$(2.59a) \quad (EI_1 + EAy_0^2) \left(\frac{d^4v}{ds^4} + \frac{1}{R} \frac{d^3w}{ds^3} \right) - \frac{EA}{R} \left(\frac{dw}{ds} - \frac{v}{R} + y_0 \left(2 \frac{d^2v}{ds^2} + \frac{1}{R} \frac{dw}{ds} - R \frac{d^3w}{ds^3} \right) \right) + \bar{k}_{vv}v = f_v$$

$$(2.59b) \quad - \left(\frac{EI_1}{R} + EAy_0 \left(1 + \frac{y_0}{R} \right) \right) \left(\frac{d^3v}{ds^3} + \frac{1}{R} \frac{d^2w}{ds^2} \right) - EA \left(1 + \frac{y_0}{R} \right) \left(\frac{d^2w}{ds^2} - \frac{1}{R} \frac{dv}{ds} \right) + \bar{k}_{ww}w = f_w$$

Combining these two equations (by taking the determinant of the v, w submatrix in Eqn. (2.58)) results in a single governing equation for v :

$$(2.60) \quad \frac{d^6v}{d\theta^6} + \left[2 - \lambda_{ww} \left(\left(\frac{y_0}{R} \right)^2 + \left(\frac{r_y}{R} \right)^2 \right) \right] \frac{d^4v}{d\theta^4} \\ + \left[1 + \lambda_{vv} \left(\left(1 + \frac{y_0}{R} \right)^2 + \left(\frac{r_y}{R} \right)^2 \right) + 2\lambda_{ww} \left(\frac{y_0}{R} \right) \right] \frac{d^2v}{d\theta^2} - \lambda_{ww} \left[1 + \lambda_{vv} \left(\frac{r_y}{R} \right)^2 \right] v = 0$$

where $\lambda_{vv} = \bar{k}_{vv}R^4/EI_1$ and $\lambda_{ww} = \bar{k}_{ww}R^4/EI_1$. The tangential spoke stiffness \bar{k}_{ww} is related to the projection of the spoke stiffness along the tangential direction. For practical wheels, \bar{k}_{ww} is at least 2 orders of magnitude smaller than \bar{k}_{vv} . Analytical solutions to Eqn. (2.60) are possible because the roots of the characteristic equation come in three pairs, $\pm r_i$.

Further simplification is possible for most practical cases by noting that $y_0, r_y \ll R$. These conditions are equivalent to assuming that the beam is doubly-symmetric, and that extension of the centerline can be neglected, respectively.

$$(2.61) \quad \frac{d^6v}{d\theta^6} + 2 \frac{d^4v}{d\theta^4} + (1 + \lambda_{vv}) \frac{d^2v}{d\theta^2} - \lambda_{ww}v = 0$$

Equation (2.61) is the same as Pippards result obtained from equilibrium of a differential element of the rim [68]. The boundary conditions and solution procedure is identical for (2.61) and (2.60).

2.5.1. Loading case I: radial point load

The vertical reaction force from the road is represented by a radial point load at $\theta = 0$. The radial displacement closely resembles the classical solution of a point load acting on a beam supported by an elastic

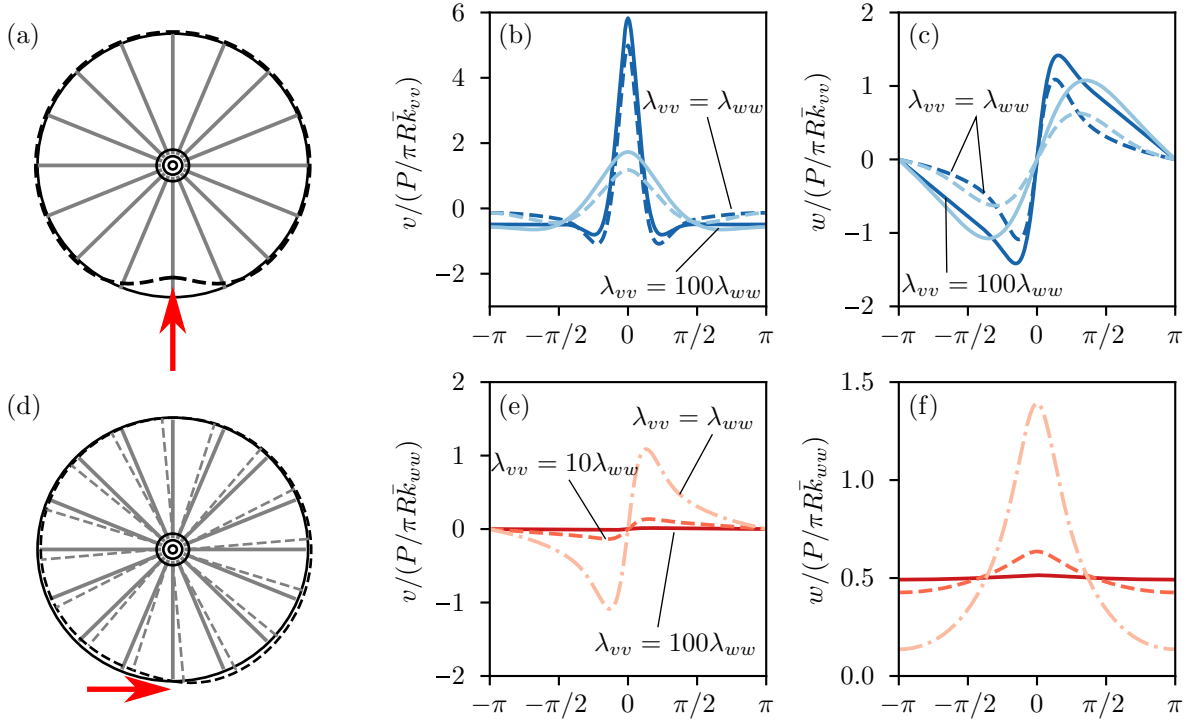


Figure 2.4. (a)-(c) Deformation of a wheel subject to a radial point load, normalized by $P/\pi R \bar{k}_{vv}$. For the dark lines $\lambda_{vv} = 1000$ and for the light lines $\lambda_{vv} = 10$. (d)-(f) Deformation of a wheel subject to a tangential point load.

foundation [37]. The rim bends inwards in a narrow arc near the load and squashes outwards on either side of this region due to the tendency of the rim to maintain a constant total circumference⁷. Far from the load, spoke tensions generally change by a very small amount on the order of 5% of the applied load. This has led some to claim that “the hub stands on the spokes beneath it,” despite the counter-intuitive image this conjures [10, 27]. Others insist that the hub “hangs from the spokes above it” due to the fact that the spoke tensions above the hub are higher than those below it [23]. Both statements are mathematically equivalent, but it is clear that the lower spokes play the most significant dynamic role in supporting the bicycle and are most prone to loosening or buckling under load.

⁷The spoke tensions on either side of the affected length can increase significantly if the bottommost lose tension. In one test on a 20” wheel, the spoke nipples in this region failed, ejecting the spokes like arrows from a bow. No one was injured.

If, as is generally the case for practical wheels, $\lambda_{vw} \ll \lambda_{vv}$, Eqn. (2.61) simplifies to

$$(2.62) \quad \frac{d^4 v}{d\theta^4} + 2\frac{d^2 v}{d\theta^2} + (1 + \lambda_{vv})v = 0$$

Since all the derivatives have even order, a relatively simple analytical solution to (2.62) exists. The radial displacement under a point load P at $\theta = 0$ is given by

$$(2.63) \quad v = \frac{PR^3}{4abEI_1} \left(\frac{2ab}{\pi\eta^2} + \frac{b \sinh a\theta \cos b\theta}{\eta} - \frac{a \cosh a\theta \sin b\theta}{\eta} + A \cosh a\theta \cos b\theta + B \sinh a\theta \sin b\theta \right)$$

where

$$\begin{aligned} \eta &= \sqrt{\lambda_{vv} + 1}, \quad a = \sqrt{\frac{\eta - 1}{2}}, \quad b = \sqrt{\frac{\eta + 1}{2}} \\ A &= -\frac{a \sin 2\pi b + b \sinh 2\pi a}{2\eta(\sinh^2 \pi a + \sin^2 \pi b)} \\ B &= \frac{a \sinh 2\pi a - b \sin 2\pi b}{2\eta(\sinh^2 \pi a + \sin^2 \pi b)} \end{aligned}$$

This solution for radial spokes was first given in slightly different form by Smith [78] in 1901 and later by Pippard [66] and Hetenyi [37]. The radial stiffness is

$$(2.64) \quad K_{rad} = \frac{\pi R \bar{k}_{vv}}{\pi \lambda_{vv}} \left(\frac{1}{2\pi\eta^2} - \frac{b \sinh a\pi \cosh a\pi + a \sin b\pi \cos b\pi}{4ab\eta(\sinh^2 a\pi + \sin^2 b\pi)} \right)^{-1}$$

2.5.2. Loading case II: tangential point load

During acceleration (or deceleration with disc brakes⁸), the reaction force from the road has a component in the tangential direction. The tangential displacement is primarily controlled by the stiffness \bar{k}_{ww} , while the ratio $\lambda_{ww}/\lambda_{vv}$ controls the degree to which radial displacement is also involved.

A very satisfactory approximation to the problem of a tangential load can be obtained by noting that $\lambda_{vv} \gg \lambda_{ww}$ and therefore the radial displacement is very small compared with the tangential displacement. Under this approximation, the rim rotates about the axle as a rigid body and the tangential stiffness is

$$(2.65) \quad K_{tan} = 2\pi R \bar{k}_{ww}$$

⁸With rim brakes, the torque from the road force is reacted by the force applied by the brake pads. The spokes at the front of the wheel lose tension while the spokes at the back gain tension.

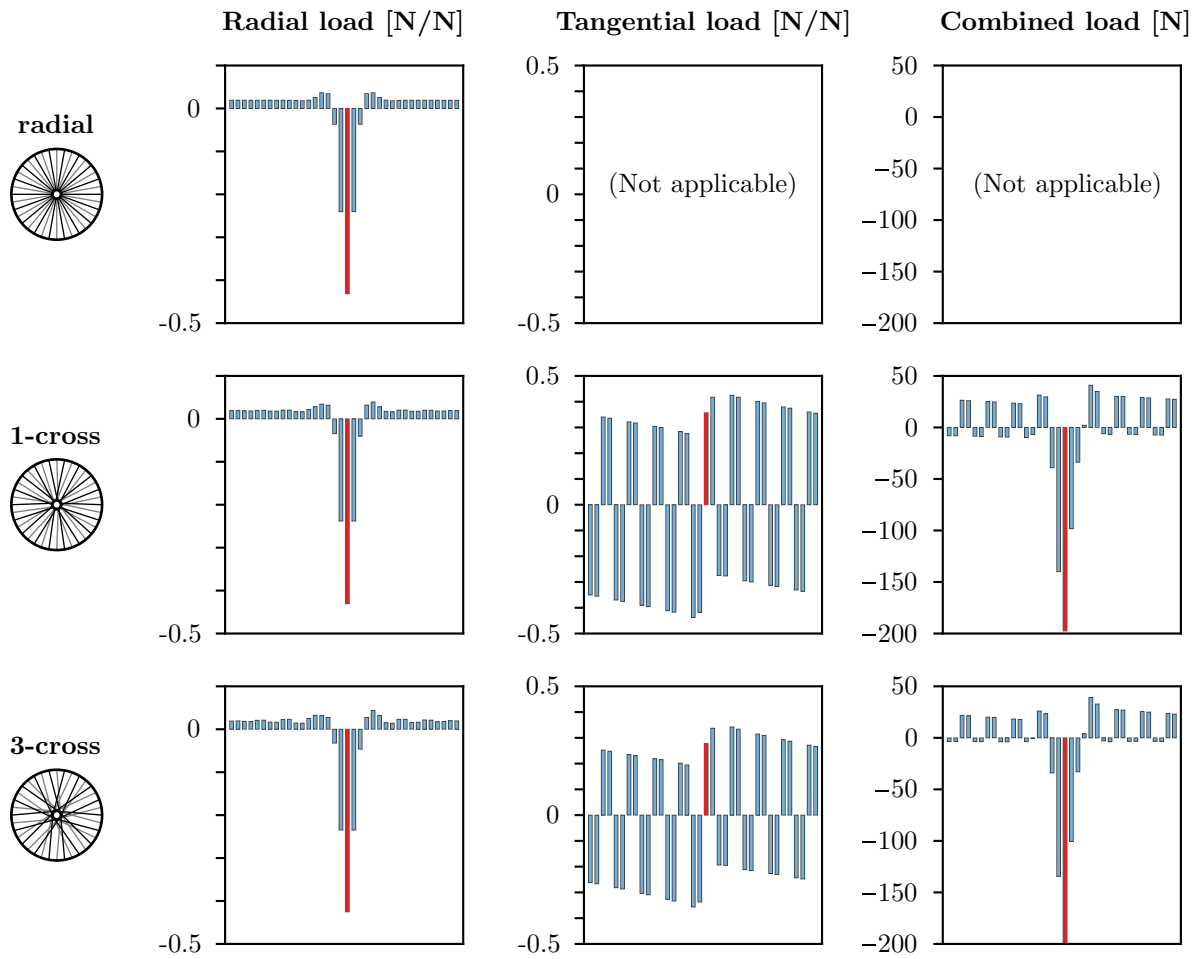


Figure 2.5. Change in spoke tension under different loading scenarios: unit radial load (left column), unit tangential load (center column), 500 N radial load and 50 N tangential load (right column). Each row corresponds to a different spoke pattern. The red bar represents the spoke at the load point. (A wheel with radial spokes cannot support tangential loads without significant non-linear deformation, therefore those plots have been omitted.)

2.5.3. The role of spoke tension in supporting in-plane loads

The model considered here depends on the assumption that a pretensioned spoke can equally support tension or compression (or rather, loss of tension). In order for this assumption to be valid, all of the spokes must maintain positive tension at all times. This condition may be violated if an excessive load is applied to the wheel.

Figure 2.5 shows the change in spoke tension for a typical road bike wheel⁹ under different loading scenarios. The spokes are given an initial pretension of 800 N. Under a radial load, the most critical spoke supports 44 % of the applied load, while the load sharing fractions for the nearest-neighbor and next-nearest-neighbor spokes are about 24 % and 3 %, respectively. In a properly tensioned wheel spokes should not go slack under typical loads.

On a typical wheel with tangent spokes, half of the spokes are inclined forward in the plane of the wheel, while the other half are inclined backwards. These are referred to as “pushing” and “pulling” or “leading” and “trailing” spokes due to their behavior under torque. Pulling spokes increase their tension under acceleration torque while pushing spokes decrease their tension, as shown in Fig. 2.5 (middle column). Under a combined radial load and acceleration torque, the primary factor causing spokes to slacken is the radial load, while the primary factor causing spokes to tighten is the tangential load. Therefore, both types of loads should be accounted for when making fatigue calculations.

2.6. Loads out of the plane of the wheel

Under lateral loads, the rim bends and twists into a non-planar shape. The wheel is considerably more flexible in the lateral direction than in the radial direction due to the small lateral projection of the spokes. When the rim undergoes lateral deformation, the potential energy of the compressive load induced by the spoke pretension is reduced. Due to the large lateral compliance, this reduction in potential energy can be significant compared to the increase in strain energy due to lateral bending and twisting. This leads to larger lateral deflections with the possibility of lateral-torsional instability at a sufficiently high spoke tension.

The lateral-torsional equations are

$$(2.66a) \quad EI_2 \left(\frac{d^4 u}{ds^4} + \frac{1}{R} \frac{d^2 \phi}{ds^2} \right) - \frac{EI_w}{R^2} \left(R \frac{d^4 \phi}{ds^4} - \frac{d^4 u}{ds^4} \right) + \frac{GJ}{R^2} \left(R \frac{d^2 \phi}{ds^2} - \frac{d^2 u}{ds^2} \right) + RT \left(\frac{d^2 u}{ds^2} + y_0 \frac{d^2 \phi}{ds^2} - \frac{r_0^2}{R^2} \left(R \frac{d^2 \phi}{ds^2} - \frac{d^2 u}{ds^2} \right) \right) + \bar{k}_{uu} u + \bar{k}_{u\phi} \phi = f_u$$

$$(2.66b) \quad \frac{EI_2}{R} \left(\frac{d^2 u}{ds^2} + \frac{1}{R} \phi \right) + EI_w \left(\frac{d^4 \phi}{ds^4} - \frac{1}{R} \frac{d^4 u}{ds^4} \right) - GJ \left(\frac{d^2 \phi}{ds^2} - \frac{1}{R} \frac{d^2 u}{ds^2} \right) + RT \left(r_0^2 \left(\frac{d^2 \phi}{ds^2} - \frac{1}{R} \frac{d^2 u}{ds^2} \right) + y_0 \left(\frac{d^2 u}{ds^2} + \frac{\phi}{R} \right) \right) + \bar{k}_{\phi\phi} \phi + \bar{k}_{u\phi} u = m$$

⁹See Appendix B.1 for complete wheel properties.

This coupled system leads to an eighth-order ordinary differential equation with constant coefficients and all even-order derivatives. Analytical formulae for the roots are possible, but impractical due to the need to find roots of a quartic characteristic polynomial. Neglecting warping stiffness and defining the non-dimensional groups $\lambda_{uu} = \bar{k}_{uu}R^4/EI_2$, $\mu = GJ/EI_2$, and $\tau = R^3\bar{T}/EI_2$, Eqns. (2.66) become:

$$(2.67) \quad \left(1 - \frac{\tau r_0^2}{\mu R^2}\right) \frac{d^6 u}{d\theta^6} + \left(2 - \frac{\lambda_{\phi\phi}}{\mu} + \tau + \tau \frac{y_0}{R} \left(2 + \frac{1}{\mu}\right) - 2\frac{\tau}{\mu} \left(\frac{r_0^2}{R^2}\right) - \frac{\tau^2}{\mu} \left(\frac{r_0^2}{R^2} - \frac{y_0^2}{R^2} + \frac{r_0^2 y_0}{R^3}\right)\right) \frac{d^4 u}{d\theta^4} + \left(1 + \lambda_{uu} + \lambda_{\phi\phi} + 2\lambda_{u\phi} \left(1 + \frac{1}{\mu}\right) - \frac{\tau}{\mu} \left(1 + \lambda_{\phi\phi} - \frac{y_0}{R}(\mu + 2\lambda_{u\phi}) + \frac{r_0^2}{R^2} (1 + \lambda_{uu} + \lambda_{\phi\phi} + 2\lambda_{u\phi})\right) - \frac{\tau^2 y_0}{\mu R} \left(1 + \frac{r_0^2}{R^2}\right)\right) \frac{d^2 u}{d\theta^2} - \frac{1}{\mu} \left(\lambda_{uu} \left(1 + \tau \frac{y_0}{R}\right) + \lambda_{uu} \lambda_{\phi\phi} - \lambda_{u\phi}^2\right) u = 0$$

The terms arising from the Wagner moment are vanishingly small. The ratio r_0^2/R^2 is on the order of $10^{-4} \sim 10^{-3}$ for a typical rim, while τ is of order $1 \sim 10$. Neglecting second-order quantities r_0^2, y_0^2 compared to R^2 , Eqn. (2.67) becomes:

$$(2.68) \quad \frac{d^6 u}{d\theta^6} + \left(2 - \frac{\lambda_{\phi\phi}}{\mu} + \tau + \tau \frac{y_0}{R} \left(2 + \frac{1}{\mu}\right)\right) \frac{d^4 u}{d\theta^4} + \left(1 + \lambda_{uu} + \lambda_{\phi\phi} + 2\lambda_{u\phi} \left(1 + \frac{1}{\mu}\right) - \frac{\tau}{\mu} \left(1 + \lambda_{\phi\phi} - \frac{y_0}{R}(\mu + 2\lambda_{u\phi})\right) - \frac{\tau^2 y_0}{\mu R}\right) \frac{d^2 u}{d\theta^2} - \frac{1}{\mu} \left(\lambda_{uu} \left(1 + \tau \frac{y_0}{R}\right) + \lambda_{uu} \lambda_{\phi\phi} - \lambda_{u\phi}^2\right) u = 0$$

Dropping the terms in Eqn. (2.68) involving $\tau, y_0, \lambda_{u\phi}, \lambda_{\phi\phi}$, one recovers the differential equation derived by Pippard [67]. The dimensionless tension τ can be interpreted as the spoke tension divided by the spoke tension which would create a compressive stress in the rim equal to the buckling load of a straight fixed-fixed column of length $2\pi R$. The stiffness ratio λ_{uu} is a sum of two parts: λ_{uu}^{matl} , a term proportional to the elastic stiffness of the spokes and λ_{uu}^{geom} , a term proportional to the spoke tension. For most bicycle wheels, the geometric stiffness is well approximated as $\lambda_{uu}^{geom} = R^2 l_s \bar{T}/EI_2 \approx \tau$.

2.6.1. Solutions to (2.66) by the equivalent springs method.

Equation (2.68) is a sixth-order linear ordinary differential equation with constant coefficients. Since all the derivatives have even order, the roots of the characteristic equation can be solved analytically by solving a cubic equation. However, a straightforward approximation of arbitrary accuracy which preserves warping stiffness is possible using the mode matrix method described in Section 2.4.1. Furthermore, if coupling between in-plane and out-of-plane deformations is precisely zero or neglected (i.e. $\bar{k}_{uv} = \bar{k}_{uw} = 0$), the spoke offset vector is sufficiently small ($\mathbf{b}_s = 0$), and the rim shear center offset y_0 is neglected, then the lateral stiffness of the wheel can be modeled as a system of equivalent springs with clear physical interpretations.

Under a lateral point load P applied at $\theta = 0$, the modal approximation (2.47) to the lateral displacement becomes

$$(2.69) \quad u = u_0 + \sum_{n=1}^N u_n \cos n\theta$$

The lateral stiffness $K_{lat} = P/u(0)$ is found by combining the individual mode stiffnesses P/u_n using the series-spring rule:

$$(2.70) \quad \frac{1}{K_{lat}} = \frac{1}{K_0} + \frac{1}{K_1} + \frac{1}{K_2} + \dots$$

The mode stiffnesses are found by solving the appropriate block of the mode matrix $\mathbf{K}_{rim} + \mathbf{K}_{spk}$ with the simplifying assumptions described above:

$$(2.71a) \quad K_0 = 2\pi R \bar{k}_{uu}$$

$$(2.71b) \quad K_1 = \pi R \bar{k}_{uu} - \pi \bar{T}$$

$$(2.71c) \quad K_{n \geq 2} = \pi R \bar{k}_{uu} + \frac{K_b K_t}{K_b + K_t} - \pi n^2 \bar{T}$$

where

$$K_b = \frac{\pi E I_2}{R^3} (n^2 - 1)^2$$

$$K_t = \frac{\pi \widetilde{G} J}{R^3} n^2 (n^2 - 1)^2$$

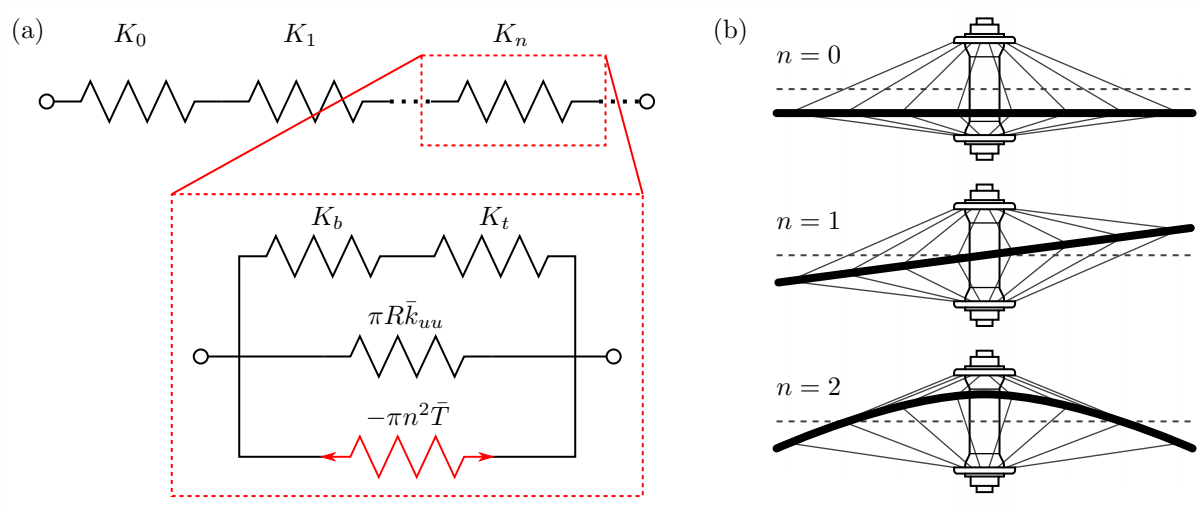


Figure 2.6. Equivalent springs model for lateral stiffness. **(a)** Mode stiffnesses represented as springs. **(b)** Illustrated mode shapes for the first three modes.

where $\widetilde{GJ} = GJ + EI_w n^2 / R^2$ is the effective torsional stiffness of the n th mode. This model corresponds to the diagram shown in Fig. 2.6. The $n = 0$ mode is a rigid-body displacement of the rim along the \mathbf{e}_1 direction. The $n = 1$ mode is a rigid-body rotation of the rim about an axis in the plane of the wheel passing through the hub. The $n = 2$ mode is the well-known ‘‘taco’’ shape that a wheel typically takes on when buckled. Each mode stiffness is composed of three springs in parallel: (1) a spring representing the stiffness of the spokes, (2) a spring representing the stiffness of the rim, itself composed of two springs in series for the effective bending and torsional stiffnesses, and (3) a destabilizing (negative stiffness) spring representing the tendency of the wheel to buckle under excessive tension. Because the rim stiffness increases dramatically with n , a satisfactory approximation can usually be obtained by only including three or four terms in the series (2.70).

A few observations can be gleaned from the equivalent spring model: First, the bending and torsion stiffness of the rim combine like springs connected in series, and the total rim stiffness is dominated by the smaller spring constant. If the torsional stiffness GJ is significantly less than the lateral bending stiffness EI_2 (e.g. in a single-wall rim or a wide ‘‘fat-bike’’ rim), the wheel stiffness will be dictated by the torsional stiffness and the lateral stiffness will have an insignificant effect. The equivalent springs model also makes

clear the dominant role that the spoke system plays in lateral stiffness. The first two modes represent rigid-body motions of the rim and only involve the spoke stiffness. If the rim is made infinitely stiff (compared to the spokes), a rigorous upper-bound for the wheel stiffness is given by

$$(2.72) \quad \max K_{lat} = \frac{2}{3} \pi R \bar{k}_{uu}$$

Bicycle wheels are often marketed on their stiffness, which is prized for its presumed benefits to performance and durability. However, as modern rims have become stiffer, wheel manufacturers have followed a trend towards fewer spokes as a way to save weight, reduce drag, and cut costs [11]. How might a modern wheel compare with a typical road wheel from the 1970s?

Table 2.1. Example wheel properties.

Wheel	GJ [N m ²]	EI_2 [N m ²]	$\pi R \bar{k}_{uu}$ [N/mm]	K_{lat} [N/mm]
Modern	80	200	190	82.4
Vintage	15	150	244	84.3

As an example calculation, let us consider two hypothetical front wheels with the same hub width (50 mm): (a) a modern racing bicycle wheel constructed from a modern 700C double-wall rim with 24 1.8 mm spokes, and (b) a vintage road bicycle wheel constructed from a 27" single-wall rim with 36 1.8 mm spokes. The rim properties and spoke system stiffnesses are given in Table 2.1. Equation (2.70) gives a theoretical lateral stiffness of 82.4 N/mm for wheel (a) and a stiffness of 84.3 N/mm for wheel (b). The greater number of spokes in wheel (b) make up for its relatively flexible rim. In the modern racing bike wheel, the first two modes (spokes alone) account for 65% of the total wheel flexibility, compared with 52% for the vintage road wheel.

2.6.2. Lateral stiffness vs. spoke tension

A common misconception among cyclists holds that increasing spoke tension results in a stiffer wheel. This theory likely stems from an intuitive association between “tight” and “stiff,” and possibly from the fact that a spoke, when plucked, produces a pitch proportional to its tension [5]. However, the conventional wisdom among wheelbuilders and bike industry professionals holds that spoke tension has no effect on

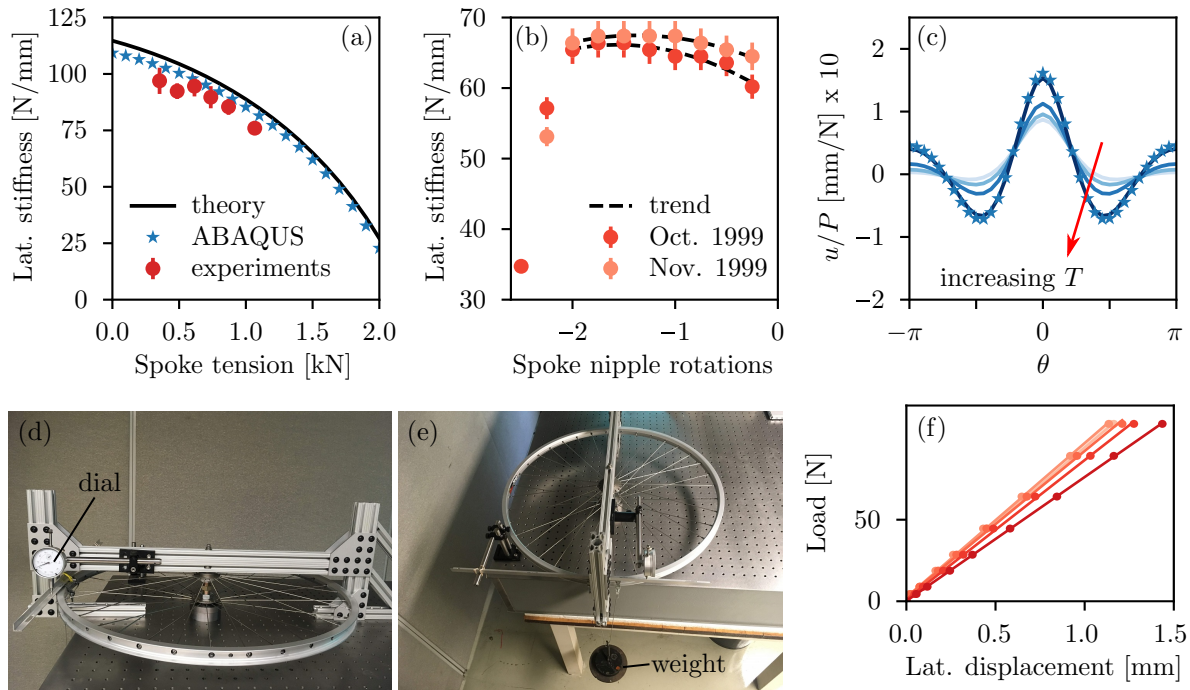


Figure 2.7. Influence of spoke tension on lateral stiffness. **(a)** Comparison of lateral stiffness vs. spoke tension calculated from non-linear finite-element simulations (ABAQUS Standard), Eqn. (2.70), and my own experiments. **(b)** Experimental results by Damon Rinard, conducted twice on the same wheel (adapted from [70] with permission). **(c)** Deformed shape of the rim under a unit load under increasing spoke tensions. $T = 0, 500, 1000,$ and 1500 N. **(d)-(e)** Experimental setup. **(f)** Load-displacement curves for the six tensions.

stiffness provided that spokes do not go slack under external loads. [70, 45, 38, 30]. Both of these views are incorrect.

Spoke tension appears in the equilibrium equations in two ways: (1) the “tension-stiffness” (geometric stiffness) of the spokes—the phenomenon responsible for the stiffness of guitar strings—and (2) the tendency of the rim to buckle under the compressive load induced by the spoke tension. These two effects are in opposition and roughly balance out at low spoke tensions. However, at sufficiently high tension, the negative stiffness term $-\pi n^2 \bar{T}$ begins to dominate and cause the lateral stiffness to decrease. (At a critical tension, the lateral stiffness vanishes entirely and the wheel buckles into a non-planar shape. This phenomenon will be explored in Chapter 4).

Damon Rinard measured the lateral stiffness of a wheel at different tensions and concluded that tension has no significant impact on stiffness, unless the tension is so low that the spokes on the loaded side of the rim buckle [70]. Rinard measured stiffness by hanging a 25 lb weight and recording the deflection with a dial indicator. He did not report the tension for each configuration, but rather reported the number of quarter turns of the spoke nipple below “full tension.” Although the relationship between turns and tension depends on wheel parameters that he did not report, it can be assumed that the relation is linear.

Rinard’s results¹⁰ are re-plotted in Fig. 2.7 (b) (his original data was reported as deflections rather than stiffness). At low tension, his measured stiffness drops by about 50 % due to buckling of spokes under his relatively large test load. At higher tensions, he measured a decrease of about 9 %¹¹. It is difficult to increase the spoke tension in a typical wheel to much more than about 50 % of the buckling tension due to friction at the spoke nipple and the magnification of geometric imperfections in the rim which make it difficult or impossible to keep it laterally true. Thus the most likely explanation for the conventional wisdom that spoke tension does not affect stiffness is that no one has tested rims at sufficiently high tensions or additional compliance in the hub or bearings obscured the effect.

I measured the lateral stiffness of a wheel at six different spoke tensions. The hub was clamped into a custom fixture mounted to a rigid table. To remove compliance in the hub and bearings I built a custom research hub consisting of steel flanges screwed onto a 3/4-inch threaded axle¹². The load was applied by hanging weights from the rim. The tension in every spoke was measured using the technique described in Appendix D and averaged. The displacement was measured using a dial indicator positioned on a pivoting bar at a point 10 cm away from the load point. The bar magnified the displacement and enabled the use of smaller loads. The load-displacement curves are shown in Fig. 2.7 (f).

The experimental results¹³ are shown in Fig. 2.7 (a), compared against Eqn. (2.70) and ABAQUS simulations. The stiffness recorded at 1067 N spoke tension (76.0 N/mm) is about 22 % lower than the maximum recorded stiffness (97.0 N/mm). At higher tensions, the spoke nipples become difficult to turn and

¹⁰The error bars in Fig. 2.7 (b) include Rinard’s reported displacement uncertainty of ± 0.002 in and an assumed 1 % load uncertainty.

¹¹He repeated the experiment on a different day and measured a tension decrease of only 4 %, but it’s not clear if the tensions were identical between the two experiments.

¹²See Appendix B.1 for complete wheel properties.

¹³The error bars in Fig. 2.7 (a) include the confidence interval on the linear fit parameter, the displacement uncertainty of ± 0.001 in, and an assumed 1 % load uncertainty.

the rim begins to take on a distorted shape. To my knowledge, these are the first reported measurements of lateral stiffness which are quantitatively compared with theory and simulations.

2.6.3. Wheels with offset spokes: “fat bikes”

A recent trend towards extremely wide tires has led to the development of lightweight rims with widths on the order of 50–100 mm. Bikes equipped with such wheels, referred to as “fat bikes,” have gained popularity for their ability to handle mud, snow, and sand. A typical fat bike rim is extremely wide compared with its depth, giving it a very small torsional stiffness compared with its lateral bending stiffness. To prevent the rim cross-section from easily rotating, the spoke nipples are commonly offset from the centerline as shown in Fig. 2.8 (a) (blue dashed lines).

In this case, the mode stiffnesses include contributions from the lateral stiffness \bar{k}_{uu} as well as the torsional stiffness $\bar{k}_{\phi\phi}$ and the lateral-torsional coupling stiffness $\bar{k}_{u\phi}$. Solving Eqn. (2.57) for a lateral point load with the smeared-spokes approximation and neglecting y_0, r_x, r_y , we obtain the mode stiffnesses analogous to Eqn. (2.71):

$$(2.73a) \quad K_0 = 2\pi R \left(\bar{k}_{uu} - \frac{R^2 \bar{k}_{u\phi}^2}{EI_2 + R^2 \bar{k}_{\phi\phi}} \right)$$

$$(2.73b) \quad K_1 = \pi R \bar{k}_{uu} + \pi \left(\frac{\left(\frac{EI_2}{R^3} + \frac{GJ}{R^3} + \frac{EI_w}{R^5} \right) \left(\frac{\bar{k}_{\phi\phi}}{R} + 2R \bar{k}_{u\phi} \right) - \bar{k}_{u\phi}^2}{\frac{EI_2}{R^3} + \frac{GJ}{R^3} + \frac{EI_w}{R^5} + \frac{\bar{k}_{\phi\phi}}{R}} \right) - \pi \bar{T}$$

$$(2.73c)$$

$$K_{n \geq 2} = \pi R \bar{k}_{uu} + \left(\frac{K_b K_t + (\pi \bar{k}_{\phi\phi}/R)(K_b n^4 + K_t) + 2\pi \bar{k}_{u\phi}(K_b n^2 + K_t) - (n^2 - 1)^2 \pi^2 \bar{k}_{u\phi}^2}{K_b + K_t + (n^2 - 1)^2 \pi \bar{k}_{\phi\phi}/R} \right) - \pi n^2 \bar{T}$$

Like Eqn. (2.71), the mode stiffness with offset spokes includes a term representing the lateral stiffness of the spokes system, a term representing the reduction in stiffness caused by the compressive stress in the rim, and a term representing the stiffness of the rim, but in the case of Eqn. (2.73) the rim bending and torsion stiffness terms are combined with $\bar{k}_{\phi\phi}$ and $\bar{k}_{u\phi}$. The diagonal terms \bar{k}_{uu} and $\bar{k}_{\phi\phi}$ are strictly positive, but the coupling term $\bar{k}_{u\phi}$ may be positive or negative depending on the arrangement of the spokes. If the spokes are connected to the rim centerline (Fig. 2.8 (a), black lines), then $\bar{k}_{u\phi} = \bar{k}_{\phi\phi} = 0$, and Eqn. (2.73) reduces to (2.71). If the spoke nipples are offset towards the hub flanges (blue dashed lines), the coupling

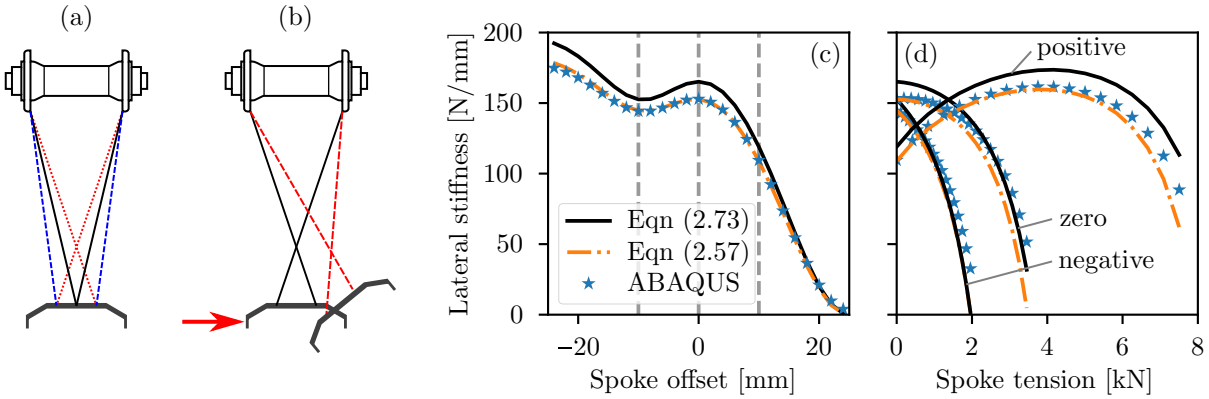


Figure 2.8. **(a)** Schematic showing a fat bike wheel with no spoke offset (black solid lines), positive spoke offset (blue dashed lines), and negative spoke offset (red dotted lines). **(b)** Rigid mechanism rotation mode afforded by the negative spoke offset arrangement. **(c)** Lateral stiffness as a function of spoke offset. **(d)** Lateral stiffness as a function of spoke tension for zero offset, and ± 10 mm offsets.

term $\bar{k}_{u\phi}$ is positive. This is the standard method for lacing fat bike wheels. If the spoke nipples are offset away from the hub flanges (red dotted lines), the coupling term $\bar{k}_{u\phi}$ is negative.

It has been suggested that the cross-over lacing pattern (negative offset, Fig. 2.8 (a), red dotted lines) could increase the lateral stiffness of a wheel by increasing the lateral bracing angle, α . Shimano marketed a road bike wheel (Dura-Ace WH7700) with a narrow road rim in which the spokes were attached to the outside edge of the rim opposite the hub flange [70]. More recently, the cross-over lacing pattern has been discussed as a possible improvement to fat bike wheels¹⁴. Since the spoke holes on many fat bike rims are already offset from the centerline this design does not require specialized components.

While it is true that a negative spoke offset increases the lateral spoke stiffness \bar{k}_{uu} , it also introduces a deformation mode which allows the rim to deflect laterally and rotate while producing no reaction in the spokes. Figure 2.8 (b) shows an example of this mechanism rotation. In this mode, the spokes and rim act like a four-bar linkage: the spokes in the deformed configuration (red dashed lines) do not change length and therefore offer no resistance to deformation¹⁵.

¹⁴See, for example <http://forums.mtbr.com/fat-bikes/anybody-ever-cross-their-spokes-other-side-rim-799284.html>

¹⁵A wheel with positive spoke offset also admits a free rotation mechanism, but the rim rotates in the opposite sense. This is mode is suppressed by the natural coupling between bending and torsion in the rim.

Despite its apparent advantages, the cross-over spoke lacing pattern has a dubious effect on lateral stiffness and makes the wheel highly sensitive to spoke tension. Figure 2.73 (c) shows the lateral stiffness of an example fat bike wheel¹⁶ (at zero tension) calculated using Eqn. (2.73) (black line), using the mode matrix method with discrete spokes (orange dashed line), and the finite-element method (blue stars). Stiffness vs. tension curves are shown in Fig. 2.8 (d) for a wheel with positive, negative, and zero offsets. Although the cross-over wheel has a higher stiffness at zero tension than the wheel with positive offset, it is significantly more sensitive to tension. Such a wheel would be very difficult to build and true with adequate spoke tension.

Another possible design is to alternate conventional spokes with cross-over spokes in a hybrid design. This strategy was used in the Singapore Flyer, a Giant Observation Wheel (i.e. Ferris wheel) completed in 2008 and the largest such structure in the world at the time of its completion¹⁷ [6]. The rim is a ladder truss with its minor axis in the plane of the wheel, resulting in a large lateral bending stiffness but small torsional stiffness. The spokes are connected in groups of four (left-left, left-right, right-left, right-right) near the mount point for each observation pod. Although the wheel does not need to support concentrated external loads as the bicycle wheel does, the rim must be stabilized against lateral buckling under the spoke prestress.

This hybrid spoke pattern may be unsuitable for a typical fat bike wheel. A standard tangent-spoked wheel already has four distinct spoke types (left and right, leading and trailing). This pattern lends itself to wheels with a multiple of four spokes (e.g. the common 24, 32, and 36 spoke counts). Adding an additional factor (conventional or cross-over) increases this to eight. Such a wheel would either need to be built with a multiple of eight spokes, or with unequal numbers of each type of spoke. Furthermore, a hybrid 32-spoke wheel would have only four-fold rotational symmetry—an undesirable property for a structure which should have similar properties at every point around its circumference¹⁸.

¹⁶See Appendix B.2 for complete wheel properties.

¹⁷The Singapore Flyer has since been surpassed by the High Roller in Las Vegas. The Dubai Eye, currently under construction as of September 2018, will be even larger.

¹⁸These problems could possibly be overcome by using twice the number of spokes with a narrower gauge. One could imagine a “double hub” having two flanges on either side: an outer flange with conventionally-offset tangential spokes, and an inner flange with radial cross-over spokes.

2.7. Radial–lateral coupling

An inwards radial force at a spoke gives rise to both a radial displacement in the direction of the load and a lateral displacement opposite the hub flange to which the spoke is connected. In a symmetric wheel, this reaction is equal and opposite at adjacent spokes and this radial-lateral coupling disappears when the spoke stiffness is homogenized. However, if the spoke inclination angle is different one side of the wheel, these reactions will be opposing but not equal, giving rise to a net radial–lateral coupling.

Rear wheels and wheels for disk brakes are commonly built with one hub flange closer to the rim centerline than the other due to the need to create space for the gear cluster or the disk rotor. The out-of-plane spoke angle is steeper on the side of the wheel with the gear cluster or disk rotor. Additionally, the spokes on the steep side must be tighter by a factor of c_1^l/c_1^r . For a typical wheel, this factor is on the order of 1.5, but can be higher depending on the flange width and number of sprockets.

It is often erroneously assumed that the lateral stiffness is different in the left and right directions on such a wheel. Damon Rinard demonstrated that the stiffness is indistinguishable [70], but it should also be clear from a theoretical perspective because the stiffness is the instantaneous slope of the load-displacement curve and the spokes on each side give the same stiffness in tension as in “compression” (or more precisely, loss of tension)¹⁹.

How does the wheel stiffness depend on the degree of offset? There are two competing effects which determine the lateral stiffness. First, the change in spoke angles increases the spoke system stiffness *provided that the total hub width remains constant*. This seems counterintuitive at first since the spokes on the right side will have a very small lateral projection. However, this is more than made up for by the increase in lateral stiffness of the left spokes²⁰. Second, as the degree of offset is increased, the degree of coupling between radial and lateral deformations increases. This causes some of the force which would have been supported by the lateral mode to “leak” into a radial deformation mode which produces its own lateral displacement.

¹⁹The behavior under large displacement will, of course, be different in the left and right directions and if the stiffness is measured with too large a test load, the stiffness will appear to differ.

²⁰The lateral stiffness is proportional, to second order, to $(c_1^l)^2 + (c_1^r)^2$, where c_1 is the direction cosine of the spoke vector in the lateral direction. The direction cosine is approximately equal to the lateral distance from rim to hub flange divided by the radius. If the total hub flange width is constrained, then $(c_1^l)^2 + (c_1^r)^2$ takes on its minimum value when $c_1^l = c_1^r$, i.e. a symmetric wheel. Considering only the spokes, an asymmetrically-dished wheel should be *stiffer* than a symmetric wheel.

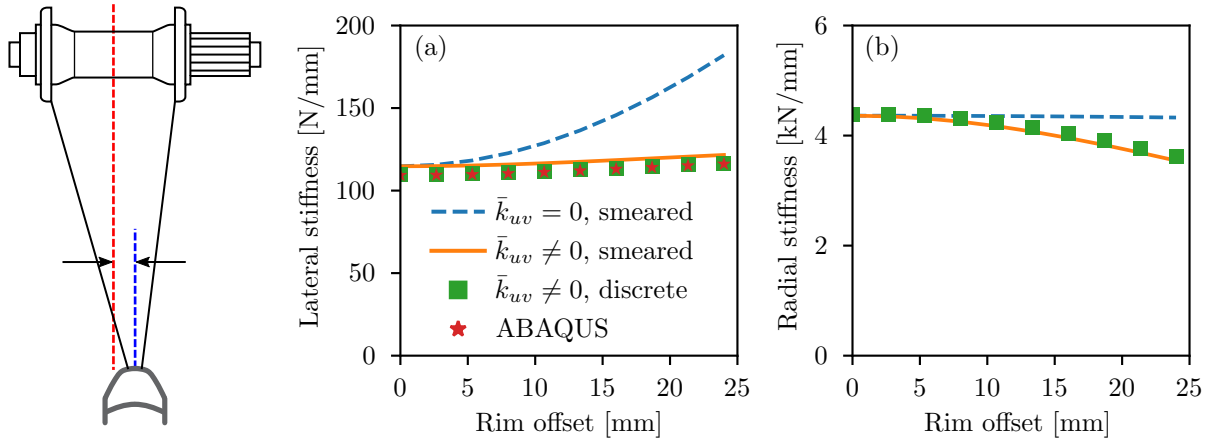


Figure 2.9. Stiffness of an asymmetrically-dished wheel with a hub flange spacing of 50 mm. **(a)** Lateral stiffness under the assumptions of no coupling and smeared-spokes (blue dashed line), full coupling and smeared spokes (orange line), and full coupling and discrete spokes (green squares). Results are compared with ABAQUS simulations (red stars). **(b)** Radial stiffness (same labels).

Figure 2.9 (a) shows the lateral stiffness as a function of rim offset (the maximum offset is $w_h/2$, where w_h is the hub width)²¹. If the coupling is neglected (i.e., the coupling terms \bar{k}_{uv} and \bar{k}_{uw} are set to zero) the lateral stiffness increases due to the increasing angle of the left spokes. However, if the coupling terms are included, the lateral stiffness is roughly constant with hub offset. This holds regardless of whether the smeared-spokes approximation is used or if the discrete spokes are retained, demonstrating that this effect is not simply an artifact of the spoke homogenization technique. The radial stiffness decreases with increasing coupling because unlike the lateral stiffness, the change in spoke angle does not increase the stiffness.

2.8. Concluding remarks

The theoretical framework developed in this chapter is sufficiently rich to capture important aspects of the mechanics of the wheel that were either ignored or incorrectly treated by previous authors. The effect of spoke tension, ignored by Pippard and Smith and widely misunderstood, is easily incorporated into analysis of the wheel with no increase in complexity of the solution through the use of modal analysis.

²¹Aside from the rim offset, the properties are identical to those of the Standard Research Wheel, Appendix B.1.

I have already alluded to the problem of buckling of the wheel under spoke tension. The lateral stiffness given by the equivalent springs model, Eqn. (2.70), goes to zero at a critical tension which represents a bifurcation instability. The nature of this instability will be explored in Chapter 4. The effect of tension on lateral stiffness also has consequences for the failure of the wheel under external loads. The competition between the distinct failure modes of rim buckling and spoke buckling leads to a simple analytical model for the radial strength of the wheel, described in Chapter 5.

The theory described here depends on physical parameters of the rim, spokes, and hub. Some are readily available or easily measured, such as the rim radius or hub dimensions. The rim stiffness parameters— EI_1 , EI_2 , and GJ —are not given in manufacturer datasheets and must be obtained by more advanced methods. A method for measuring these properties with high accuracy using only a smartphone, a tape measure, and a piece of string is described in the following chapter.

CHAPTER 3

Acoustic characterization of bicycle rims

In the preceding analysis, we have assumed prior knowledge of EI_1 , EI_2 , GJ and EI_w . Rim cross-sections typically have complicated shapes with multiple open and closed regions and the exact shape and wall thickness cannot be easily determined without a destructive test. Furthermore, the spoke holes reduce the stiffness over relevant length scales in a complex manner. Therefore, it is desirable to obtain the rim section properties experimentally and with minimal assumptions or computation¹.

Pippard and Francis [66] undertook the first quantitative experimental investigations of the stiffness of spoked wheels and compared their results with an analytical solution. For the special case of radial loads, they determined the in-plane bending stiffness of bare rims by diametral extension. The rims that they tested were cut from a steel plate and all had rectangular cross-sections of varying aspect ratio and did not resemble the complicated cross-sections of modern rims. Due to the difficulty of determining the out-of-plane bending stiffness and torsional stiffness of a circular beam, their investigation of lateral deformations was limited to theory alone. Burgoyne and Dilmaghanian [12] performed experiments on bicycle wheels and compared their results with Pippard's theory. They calculated the radial bending stiffness of the rim from geometric analysis of its cross-section, but their study was limited to radial loads. Gavin [28] noted that the out-of-plane bending stiffness and torsional stiffness are coupled in curved beams and require at least two independent measurements to determine. He performed out-of-plane deflection tests while clamping the rim at two points with various arc lengths. This method requires rigid clamps and neglects warping of the cross-section.

Experimental Modal Analysis (EMA) [21] is a technique for inspecting structures to predict the dynamic response, assess the quality of a manufactured product, or monitor the health of an existing structure [74]. In one variant of EMA, the structure is impulsively excited and then monitored using one or more accelerometers

¹The content of this chapter is adapted from [26].

or contact transducers. With enough transducers, both the natural frequencies and mode shapes may be estimated. If spatial information is not required and the modes of interest have sufficiently high acoustic coupling in air, a microphone may be used to obtain a spectrum, allowing for non-contact measurement.

The ubiquity, connectivity, and computational power of smartphones have inspired applications in non-destructive evaluation (NDE) and structural health monitoring (SHM). The built-in accelerometer has been used to identify natural modes of buildings and bridges [22], measure inclination angles [55], and detect and quantify seismic events [44]. Smartphone accelerometers generally have a maximum frequency of 50–100 Hz, and thus are limited to measuring seismic activity or natural modes of large structures.

The microphone picks up where the accelerometer leaves off: the one used in this study has a relatively flat frequency response above 100 Hz. Although the microphone has received limited attention for NDE applications, smartphone microphones have been used for close-range sonar measurements [55], detecting roller bearing failures [32], and measuring bicycle spoke tension [61]. Other potential applications in the audible range include concrete bridge deck inspections, which often rely on the operator’s trained ear to detect anomalies, and rapid inspection of automotive assemblies during manufacturing.

We have developed a method for measuring the stiffness of bicycle rims for both in-plane and out-of-plane loads using quantitative model-based EMA. Our method is fast, non-destructive, and can be performed with only simple household tools including a tape measure, a piece of string, and a smartphone. To validate the technique I compare the calculated stiffness from the acoustic test with quasistatic load-displacement tests in both the radial and lateral directions.

3.1. Resonant frequencies of a bicycle rim

A bicycle rim without spokes will resonate at its natural frequencies when struck. These resonant modes are within the audible range and can be easily recorded with a standard smartphone microphone. The modes are classified into radial bending modes (rim moves entirely within its plane) and lateral-torsional modes (rim moves out of its plane). Although both types will be present in an experimental spectrum, they can be preferentially excited by striking the rim at different angles, much like how a percussionist can control the timbre of a gong or drum.

Table 3.1. Rim properties

Rim	Type ^a	R [mm]	m_{rim} [g]
Alex ALX295	DDW	305	480
DT Swiss R460	DDW	304	459
Sun Ringle CR18 20"	DW	217	380
Sun Ringle CR18 700c	DW	304	538
Alex Y2000 26"	SW	271	460
Alex Y2000 700c	SW	302	551
Alex X404 27"	SW	307	594

^a Cross-section type: DDW=deep double-wall, DW=double-wall, SW=single-wall.

The natural frequencies of the radial bending modes depend on the rim properties as follows [86]:

$$(3.1) \quad f_n^{rad} = \frac{n(n^2 - 1)}{\sqrt{n^2 + 1}} \sqrt{\frac{EI_1}{2\pi R^3 m_{rim}}}$$

where f_n^{rad} is the n th harmonic frequency and m_{rim} is the total mass of the rim. The first mode $n = 1$ corresponds to a rigid-body motion with zero frequency. The fundamental vibration mode is $n = 2$. Having measured m_{rim} and R and identified several modes from the frequency spectrum, the in-plane bending stiffness EI_1 can be determined by solving Eqn. (3.1) and averaging the result from several different modes.

If warping is neglected, the frequencies of the lateral-torsional modes depend on the rim properties as follows [86]:

$$(3.2) \quad f_n^{lat} = \frac{n(n^2 - 1)}{\sqrt{\mu n^2 + 1}} \sqrt{\frac{GJ}{2\pi R^3 m_{rim}}}$$

where $\mu = GJ/EI_2$. Unlike Eqn. (3.1), Eqn. (3.2) depends on two independent stiffness parameters μ and GJ which must be determined simultaneously.

3.2. Experimental procedure

3.2.1. Acoustic Test

The impulse responses of seven aluminum rims of unknown properties were obtained by the following procedure: the rim was suspended by a string from the valve stem hole and struck with a screwdriver handle wrapped in rubber. The rim was struck first on the inside circumference and then on the sidewall at a

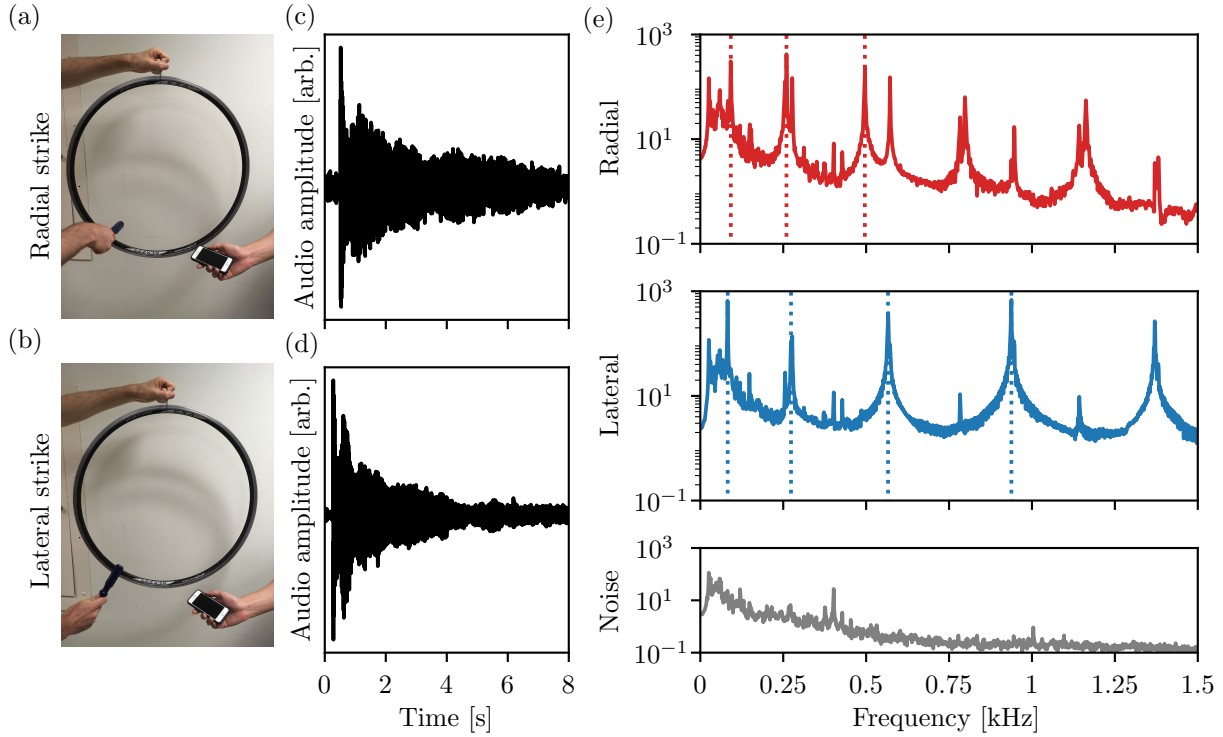


Figure 3.1. **(a)-(b)** Experimental setup for radial and lateral strike test. **(c)-(d)** Time-domain signals for radial and lateral strike test. **(e)** Fourier spectrum for radial strike (top), lateral strike (middle), and background noise (bottom).

point between two spoke holes approximately 10° from the bottom of the wheel to excite as many modes as possible. Audio was recorded with the “Recorder+” app on an iPhone SE using the built-in microphone at a sampling rate of 44.1 kHz. The frequency spectrum was estimated by averaging eight spectra calculated using the Fast Fourier Transform with a bandwidth of 1.35 Hz. A noise spectrum was also obtained by recording several seconds of silence in the same room. The frequency response of the built-in microphone was measured in an anechoic chamber and found to be sufficiently flat over the frequency range of interest (see Appendix C.1).

The peaks with a signal-to-noise ratio greater than 10 were identified and classified as radial or lateral modes depending on their relative magnitude in the two spectra. The frequency of each peak was determined by fitting a Lorentzian function in the neighborhood of the maximum value. The two peaks at 27 Hz and

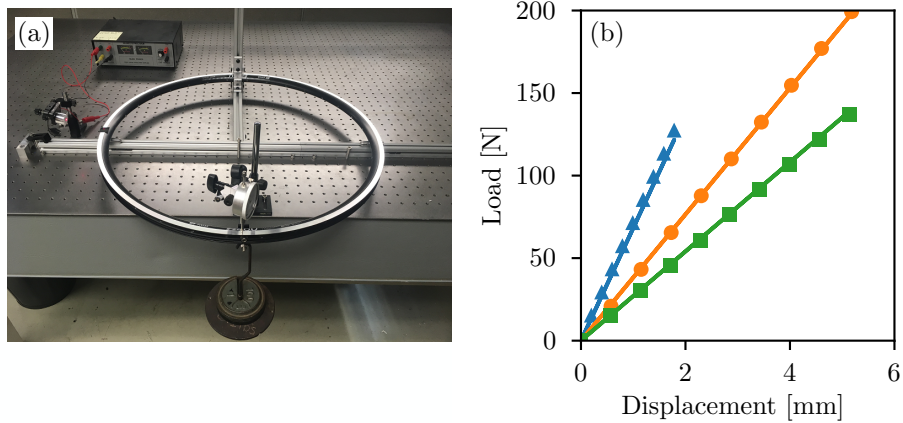


Figure 3.2. (a) Four-point bending test. A small mirror resting on the rim at 9 o'clock reflects the laser spot onto a grid (to the right, not shown). The unbalanced configuration effectively doubles the lateral displacement at the load point and increases sensitivity. (b) Selected radial load-displacement curves under diametral compression. Blue triangles = Alex ALX295, orange circles = Alex Y2000 26", green squares = Sun CR18 700C.

60 Hz were also present in the noise spectrum and therefore rejected. A detailed peak-fitting procedure is given in Appendix C.2.

3.2.2. Diametral compression

The rims were then loaded in diametral compression under displacement control in an Instron MTS (Fig. 3.2 (b)). The valve hole was placed at 45° from the load point where the bending moment is minimized to reduce its effect on the measurement. Castigliano's method gives the deflection of a ring subjected to radial point loads [85]:

$$(3.3) \quad \delta = \frac{PR^3}{4EI_1} \left(\pi - \frac{8}{\pi} \right)$$

3.2.3. Four-point bending test

The lateral stiffness of each bicycle rim was also measured using a four-point bending test [90] (Fig. 3.2 (a)). The rim was supported at 3 and 9 o'clock by cylindrical rods and constrained against a rigid bracket on the top surface of the rim at 12 o'clock. The rim was then loaded by hanging a weight from the spoke hole

(or valve hole) at 6 o'clock. The vertical deflection at 6 o'clock was measured using a dial indicator. The rotation of the cross-section at 9 o'clock was measured by tracking the movement of a laser spot, reflected off of a mirror resting on the rim and projected onto a screen with a printed grid.

If warping is neglected and only the strain energy due to lateral bending and uniform torsion are considered, Castigliano's method yields the displacement u_l at the load point and the rotation of the cross-section ϕ_s at the left support:

$$(3.4) \quad \begin{aligned} u_l &= -\left(\frac{PR^3}{2GJ}\right) [(2(3 - \pi) + \mu(2 - \pi))] \\ \phi_s &= -\left(\frac{PR^3}{8GJ}\right) (1 + \mu)(2 - \pi) \end{aligned}$$

By simultaneously measuring the deflection and rotation, GJ and μ can be determined from a single test.

3.3. Results and discussion

3.3.1. Radial stiffness

After identifying the first several mode frequencies in each spectrum, $\sqrt{EI_1/2\pi R^3 m_{rim}}$ was estimated from the fundamental ($n = 2$) mode. With knowledge of R and m_{rim} , the radial bending stiffness was determined from Eqn. (3.1).

The results for the radial stiffness EI_1 are shown in Fig. 3.3. The error estimates are made on the assumption that the mass and radius are both known to within 1%. The uncertainty in the frequency is the greater of either the estimated parameter variance from the Lorentzian fit, or the frequency resolution of the spectral average. Multiple modes may be averaged together to estimate EI_1 , however the deviation from Eqn. (3.1) grows steadily larger with higher mode number due to the fact that shorter wavelengths interact with spoke holes and other inhomogeneities.

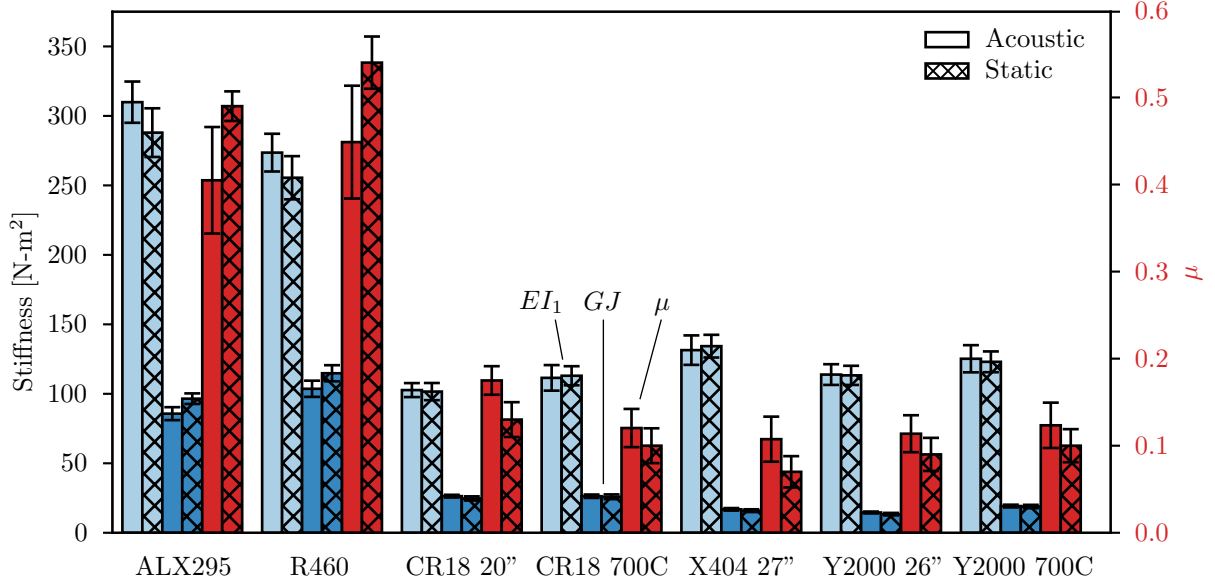


Figure 3.3. Comparison of stiffness parameters calculated from the acoustic test vs. load-displacement tests. For EI_1 and GJ , refer to the left scale. For μ , refer to the right scale.

3.3.2. Lateral-torsional stiffness

Lateral bending and torsion are coupled in out-of-plane deformation modes of circular beams. Therefore, information from multiple modes must be used to calculate GJ and μ . Taking the ratio of two lateral-torsional frequencies and solving for μ in Eqn. (3.2) gives

$$(3.5) \quad \mu = \frac{16 - (f_3^{lat}/f_2^{lat})^2}{9(f_3^{lat}/f_2^{lat})^2 - 64}$$

After calculating μ , GJ is calculated from Eqn. (3.2) by setting $n = 2$:

$$(3.6) \quad GJ = \left(\frac{4\mu + 1}{18} \right) \pi R^3 m_{rim} (f_2^{lat})^2$$

Qualitatively, GJ scales the magnitude of the frequencies and μ scales the spacing between modes. However, the situation is further complicated by the fact that the cross-section of the rim does not remain perfectly planar. This additional warping deformation introduces a length scale into the torsional stiffness

which depends on the rim radius and mode number. In this case the effective torsional response involves both GJ and EI_w , where I_w is the warping constant.

Results from the acoustic test and four-point bending test are shown in Fig. 3.3 and tabulated in Appendix C.3. The error estimates in Fig. 3.3 are made on the same assumptions as for EI_1 . Due to the non-linearity of Eqn. (3.5), error estimates for μ are calculated using the Monte-Carlo method. The lateral bending stiffness and torsion stiffness are geometrically coupled in lateral deformations. The total lateral-torsional stiffness depends on EI_2 and GJ as though they were springs connected in series. Since GJ is generally smaller than EI_2 , it dominates the total rim flexibility and can be determined with much higher precision than EI_2 or μ . Even a small uncertainty on f_3^{lat}/f_2^{lat} results in a large estimated uncertainty on μ and EI_2 , but not GJ .

The results plotted in Fig. 3.3 are tabulated in Appendix C.3.

3.3.3. Lateral-torsional mode stiffness

An acoustic test is sufficient to calculate GJ to within 11% of the results from the four-point bending test. However, both models assume that warping is negligible. In fact, the acoustic test may be even more accurate than the four-point bending test because it directly measures the mode stiffness of the rim, which includes bending, pure torsion, and warping. In order to account for warping, we derive the frequency equation for lateral-torsional vibrations with an additional term for the warping resistance:

The differential equations of dynamic equilibrium, including warping but neglecting the rotary inertia of the rim cross-section, are

$$(3.7a) \quad \frac{EI_2}{R^4} \left(\frac{d^4 u}{d\theta^4} - R \frac{d^2 \phi}{d\theta^2} \right) + \frac{EI_w}{R^6} \left(\frac{d^4 u}{d\theta^4} + R \frac{d^4 \phi}{d\theta^4} \right) - \frac{GJ}{R^4} \left(\frac{d^2 u}{d\theta^2} + R \frac{d^2 \phi}{d\theta^2} \right) + \left(\frac{m_{rim}}{2\pi R} \right) \frac{d^2 u}{dt^2} = 0$$

$$(3.7b) \quad \frac{EI_2}{R^3} \left(\frac{d^2 u}{d\theta^2} - R\phi \right) - \frac{EI_w}{R^5} \left(\frac{d^4 u}{d\theta^4} + R \frac{d^4 \phi}{d\theta^4} \right) + \frac{GJ}{R^3} \left(\frac{d^2 u}{d\theta^2} + R \frac{d^2 \phi}{d\theta^2} \right) = 0$$

We are seeking free vibrations of the form

$$(3.8a) \quad u(\theta, t) = u_n e^{in\theta} e^{2\pi i f_n^{lat} t}$$

$$(3.8b) \quad \phi(\theta, t) = \phi_n e^{in\theta} e^{2\pi i f_n^{lat} t}$$

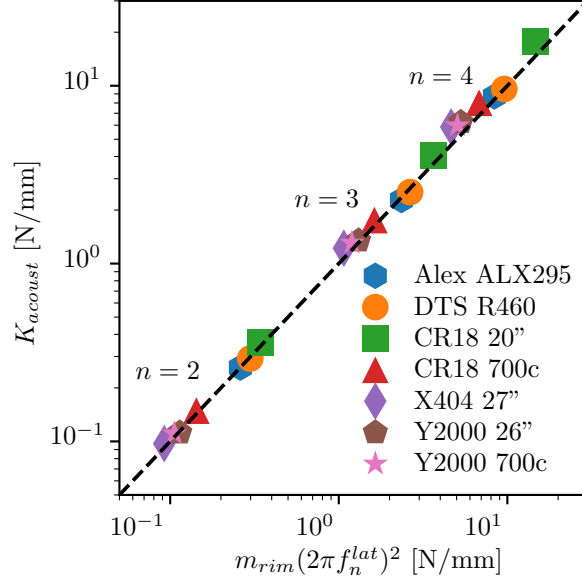


Figure 3.4. Comparison of mode stiffness from the acoustic test (x-axis) and the mode stiffness calculated from Eqn. (3.10).

Inserting Eqns. (3.8) into Eqns. (3.7) yields a linear system of the form $\mathbf{A} \cdot [u_n, \phi_n]^T = \mathbf{0}$. Non-trivial solutions exist when the determinant of the matrix \mathbf{A} vanishes. Using this condition to solve for the angular frequency $2\pi f_n^{lat}$ yields the frequency equation:

$$(3.9) \quad (2\pi f_n^{lat})^2 = \frac{2\pi n^2(n^2 - 1)^2 EI_2 (GJ + \frac{EI_w}{R^2} n^2)}{m_{rim} R^3 (EI_2 + GJ n^2 + \frac{EI_w}{R^2} n^4)}$$

Exploiting the analogy with the simple harmonic oscillator, for which $(2\pi f_n^{lat})^2 = K/m$, allows us to calculate an effective rim stiffness for the n th mode:

$$(3.10) \quad K_{acoust} = 2 \left(\frac{R^3}{\pi n^2 (n^2 - 1)^2 (GJ + \frac{EI_w}{R^2} n^2)} + \frac{R^3}{\pi (n^2 - 1)^2 EI_2} \right)^{-1}$$

Comparing Eqn. (3.10) with Eqn. (2.71), it's clear that the acoustic stiffness is twice the series combination of the rim bending stiffness and torsion stiffness. Even if EI_2 and GJ cannot be reliably determined independently, the lateral rim mode stiffness used in Eqn. (2.71) can be directly determined from the relation

$$(3.11) \quad K_n^{rim} = \frac{K_b K_t}{K_b + K_t} = \frac{m_{rim}}{2} (2\pi f_n^{lat})^2$$

CHAPTER 4

Flexural-torsional buckling under uniform tension

If the spokes are tensioned beyond a critical value the circular shape of the wheel becomes unstable and the rim buckles into a non-planar shape. The post-buckling configuration is generally stable and the original shape of the wheel can be recovered by reducing the spoke tensions. Despite its implications for wheel stiffness and strength, the buckling problem has never received a rigorous treatment. Jobst Brandt alludes to buckling in his practical manual for wheelbuilding [10]:

“If the wheel becomes untrue in two large waves during stress relieving, the maximum, safe tension has been exceeded. Approach this tension carefully to avoid major rim distortions. When the wheel loses alignment from stress relieving, loosen all spokes a half turn before retrueing the wheel.”

Stress relieving is the practice of laterally loading the rim (or the spokes directly) so that the spokes temporarily increase their tensions, which is presumed to relieve residual stresses in the spoke elbows and prevent fatigue failures.

Flexural-torsional buckling of the rim can be treated as a special case of buckling of an arch with an included angle of 2π and appropriate periodic boundary conditions. Timoshenko and Gere [85] studied the stability of arches and rings and gave a formula for the critical load for a ring with a doubly-symmetric cross-section subjected to a line load directed towards the ring’s center. The theory of flexural-torsional buckling of monosymmetric arches has been studied by many researchers using the virtual work approach [91, 87, 65, 41, 64, 48, 72]. The stability theory has been extended to arches with continuous [62] or discrete [8] elastic supports and elastic end restraints [33].

The problem of the prestressed bicycle wheel is unique for a number of reasons. First, the buckling load is internal to the structure. Second, the spokes act both as elastic restraints resisting buckling and as prestressing elements promoting buckling. Third, the lateral, radial, tangential, and torsional restraining

actions of the spokes are commonly coupled: lateral deflection at a spoke may produce a mix of those reactions on the rim section. These considerations extend to other structural systems. Large observation wheels such as the London Eye [49] and the Singapore Flyer [6] resemble bicycle wheels and achieve lateral stability by bracing the rim with prestressed cables, and must be designed against flexural-torsional buckling. At the biological scale, the cellular fragmentation process which leads to platelet formation may also be driven by a flexural-torsional buckling instability of a growing ring of bundled actin fibers loaded by an elastic membrane which both promotes buckling and provides elastic restraint [81].

4.1. Elastic stability criterion

I showed previously (Section 2.4.1) that the deformed shape of the wheel under external loads could be found by solving the mode matrix equation (2.57). One form of the elastic stability criterion states that for any admissible deformation, the second variation of the total potential (2.56) must be positive. Since any rim deformation must be periodic and continuous, the modes in (2.42) form a set of kinematically admissible deformations. Therefore the buckling tension is the tension at which (2.57) admits nontrivial solutions for $\mathbf{F}_{ext} = \mathbf{0}$.

The spoke stiffness comprises a term proportional to the elastic stiffness K_s of the spokes and a term proportional to the spoke tension T . Additionally, the rim stiffness comprises a term depending on the bending, torsion, and warping constants, and a term proportional to the net radial spoke tension per unit length, \bar{T} . In order to make the dependence on \bar{T} explicit, the buckling criterion is written as follows:

$$(4.1) \quad \det \left[\mathbf{K}_{rim}^{matl} + \mathbf{K}_{spk}^{matl} + \bar{T}(\mathbf{K}_{spk}^{geom} - \mathbf{K}_{rim}^{geom}) \right] = 0$$

If the complete details of discrete spokes and possible radial-lateral coupling are retained, a numerical solution to (4.1) can be obtained by including enough modes such that the relevant length scales (e.g. the distance between spokes) are correctly approximated, and then either numerically solving the characteristic polynomial of (4.1), or iteratively increasing \bar{T} until the determinant is minimized. Under more restrictive assumptions, analytical solutions are possible, as shown in Table 4.1.

Table 4.1. Simplifying assumptions for elastic buckling criterion.

Smeared spokes	Symmetry	Rim	Complexity	Analytical solution
No	None	Monosymmetric ^b	det of (4+8N)x(4+8N) matrix	None
Yes	None	Monosymmetric	det of 4x4 matrix	Impractical
Yes	Left-right ^a	Monosymmetric	Quadratic equation for \bar{T}_c	Solution of (4.3)
Yes	Left-right	Bi-symmetric ^c	Linear equation for \bar{T}_c	(4.4)
Yes	Left-right, no spoke offset	Bi-symmetric	Linear equation for \bar{T}_c	(4.5)

^a Left-right symmetry implies no radial/lateral coupling.

^b Monosymmetry implies $y_0 \neq 0$

^c Bi-symmetry implies $y_0 = 0$, i.e. the shear center and centroid coincide.

If the smeared-spokes approximation is used, the stiffness matrix $\mathbf{K}_{rim} + \bar{\mathbf{K}}_{spk}$ has a block diagonal form, with each block corresponding to a different mode n . The first two modes $n = 0$ and $n = 1$ are rigid-body motions of the rim and do not admit buckling. The buckling criterion then becomes

$$(4.2) \quad \det \left[\mathbf{K}_{rim,n}^{matl} + \bar{\mathbf{K}}_{spk,n}^{matl} + \bar{T}(\bar{\mathbf{K}}_{spk,n}^{geom} - \mathbf{K}_{rim,n}^{geom}) \right] = 0$$

In its most general form, Eqn. (4.2) results in a quadratic equation for \bar{T} which can be solved to find the critical tension $\bar{T}_{c,n}$ for a given mode n . The critical buckling tension \bar{T}_c for the wheel is the minimum $\bar{T}_{c,n}$ over all integer modes.

The spoke axial stiffness $E_s A_s$ is much greater than the spoke tension. Therefore, the tension components of the spoke stiffness matrix \bar{k}_{ij}^{geom} can generally be neglected compared with \bar{k}_{ij}^{matl} , except for \bar{k}_{uu} due to the small lateral projection of the spoke vector. In this section I will neglect the tension component of all stiffness parameters except for \bar{k}_{uu}^{geom} .

No radial/lateral coupling. If the radial/lateral spoke coupling terms are neglected ($\bar{k}_{uv} = \bar{k}_{uw} = \bar{k}_{v\phi} = \bar{k}_{w\phi} = 0$), the buckling criterion (4.2) reduces to

$$(4.3) \quad (R^2 \bar{k}_{uu}^{geom} y_0 - n^2 R y_0) \bar{T}^2 - \left[\frac{EI_2}{R} \left(n^2 - 3n^4 \frac{y_0}{R} + R \bar{k}_{uu}^{geom} \right) + \frac{\widetilde{GJ} n^2}{R} \left(n^2 - \frac{y_0}{R} (2n^2 - 1) - R \bar{k}_{uu}^{geom} \right) + R \bar{k}_{\phi\phi} (n^2 - R \bar{k}_{uu}^{geom}) + 2R y_0 \bar{k}_{u\phi} n^2 - R^2 \bar{k}_{uu}^{matl} y_0 \right] \bar{T} + \left[\frac{EI_2 \widetilde{GJ} n^2}{R^4} (n^2 - 1)^2 + EI_2 \left(\bar{k}_{uu}^{matl} + 2 \frac{\bar{k}_{u\phi}}{R} n^2 + \frac{\bar{k}_{\phi\phi}}{R^2} n^4 \right) + \widetilde{GJ} n^2 \left(\bar{k}_{uu}^{matl} + 2 \frac{\bar{k}_{u\phi}}{R} + \frac{\bar{k}_{\phi\phi}}{R^2} \right) \right] = 0$$

where $\widetilde{GJ} = GJ + EI_w n^2 / R^2$ is the effective torsional stiffness.

No radial/lateral coupling, bi-symmetric rim. The quadratic term in (4.3) is proportional to y_0 . If the rim cross-section is assumed to be symmetric across both the \mathbf{e}_1 and \mathbf{e}_2 axes, then the buckling criterion (4.3) reduces to a linear equation for \bar{T} . Using the non-dimensional parameters defined in Section 2.6, the non-dimensionalized critical buckling tension is given by

$$(4.4) \quad \tau_{c,n} = \left(\frac{1}{n^2 - R \bar{k}_{uu}^{geom}} \right) \left(\lambda_{uu}^{matl} + \frac{\tilde{\mu} n^2 (n^2 - 1)^2 + (n^4 + \tilde{\mu} n^2) \lambda_{\phi\phi} + 2n^2 (\tilde{\mu} + 1) \lambda_{u\phi} - \lambda_{u\phi}^2}{1 + \tilde{\mu} n^2 + \lambda_{\phi\phi}} \right)$$

where $\tilde{\mu} = \widetilde{GJ} / EI_2$ is the effective torsion stiffness ratio, including warping. The first term $(n^2 - R \bar{k}_{uu}^{geom})^{-1}$ reflects the fact the spokes (and therefore the direction of the applied tension at the rim) rotates under a buckling displacement. This term accounts for the difference between buckling under dead loads (e.g. gravity) and directed loads (e.g. tensioned cables). For typical wheels, $R \bar{k}_{uu}^{geom} \approx 1$.

No radial/lateral coupling, bi-symmetric rim, no spoke offset. If the spokes are assumed to connect to the rim through the shear center, the lateral/torsional coupling terms vanish, i.e. $\lambda_{u\phi} = \lambda_{\phi\phi} = 0$. The critical buckling tension is given by [25]

$$(4.5) \quad \tau_{c,n} = \left(\frac{1}{n^2 - R \bar{k}_{uu}^{geom}} \right) \left(\lambda_{uu}^{matl} + \frac{\tilde{\mu} n^2 (n^2 - 1)^2}{1 + \tilde{\mu} n^2} \right)$$

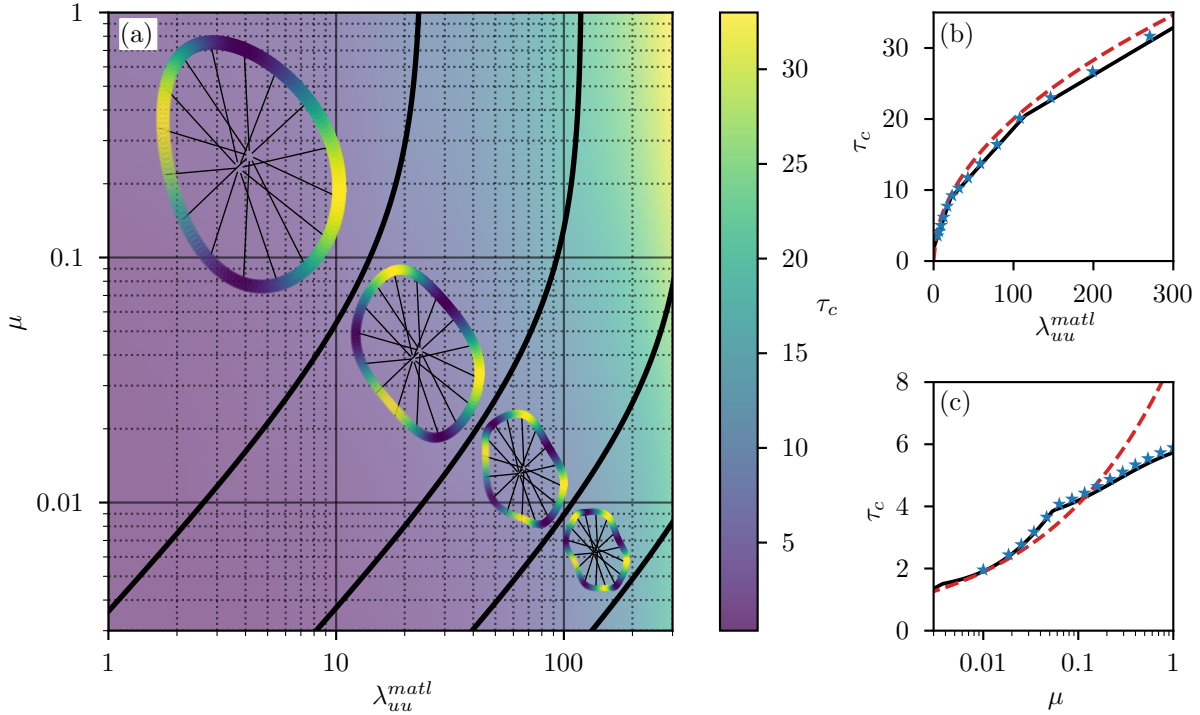


Figure 4.1. **(a)** Parameter map of preferred buckling mode. Normalized buckling tension τ_c is given by the color scale on the right. **(b)**-**(c)** Comparison between Eqn. (4.5) (black line), ABAQUS simulation results (blue stars), and power law approximations: (4.12) for (b) and (4.9) for (c). Parameters held constant are $\mu = 0.38$ for (b) and $\lambda_{uu}^{matl} = 10$ for (c).

The critical tension $\tau_{c,n}$ for a given mode depends on n , $\tilde{\mu}$, and λ_{uu}^{matl} . Therefore, the critical mode n_c only depends on $\tilde{\mu}$ and λ_{uu}^{matl} . Figure 4.1 (a) shows a map of the critical buckling modes and their respective shapes ($\tilde{\mu} = \mu$ for simplicity). Much like the related problem of the straight beam on an elastic foundation, the bicycle wheel buckling problem exhibits a length scale which depends on the ratio of beam stiffness to foundation stiffness. In an infinite beam, the wavelength of the buckling mode varies continuously with stiffness ratio. This relationship is used to estimate the elastic moduli of thin-films [14]. In the bicycle wheel problem, the buckling wavelength must fit around the rim, i.e. the circumference must be an integer multiple of the wavelength. This constraint gives rise to the discrete mode transitions shown in Fig. 4.1.

The equivalent spring model described in Section 2.6.1 provides some insight into Eqn. (4.5). The buckling tension can be found by solving Eqn. (2.71c) such that $K_{n \geq 1} = 0$.

$$(4.6) \quad \bar{T}_{c,n} = \frac{1}{\pi} \left(\frac{1}{n^2 - Rk_{uu}^{geom}} \right) K_n^0$$

where K_n^0 is given by Eqn. (2.71c), evaluated at zero tension. As with the lateral mode stiffness, the spoke stiffness and rim torsional stiffness play a significant role in determining the buckling tension *for a given mode, n* .

Why, with an infinite series of potential buckling modes available, do we only observe the ubiquitous “taco” ($n = 2$) shape? There are several possible explanations: first, it may be that wheels in common use fall into the upper left portion of Fig. 4.1. This is especially likely for modern double-wall rims which are considerably stiffer compared with their spoke systems (low λ_{uu}) than single-wall rims. As an example, a 32-hole Mavic A119 rim laced to a 50 mm wide rim would need a spoke diameter of almost 2.5 mm to cross the boundary into the $n = 3$ region. Second, the buckling tension for such a wheel would be unreasonably high—the wheel in the previous example has a buckling tension of 3.6 kN, or about 3.7 times the maximum recommended tension for most rims (100 kgf).

A third reason has to do with the sub-critical behavior. As shown in Section 2.6.1, the stiffness of each mode decreases linearly with spoke tension. At zero tension, the $n = 2$ mode is always less stiff than the $n = 3$ mode, etc. Even a wheel which falls in the $n = 3$ region of Fig. 4.1 has $K_2 < K_3$ for tensions below a significant fraction of the buckling tension. As the spoke tension is incrementally increased in such a wheel, geometric imperfections in the rim with wavelengths equal to $n = 2$ will be magnified by the decreasing K_2 stiffness. The rim will become severely distorted long before the tension is high enough to see the $n = 3$ mode appear.

4.2. Finite-element buckling calculations

I validated the theoretical predictions of Eqn. (4.5) against non-linear finite-element simulations implemented in ABAQUS Standard 6.14. The spokes and rim were both modeled using 2-node linear beam elements including shear flexibility. A controlled tensioning strain was applied to the spokes starting from zero strain and increasing up to 150% of the strain at which buckling was expected to occur. The rim was

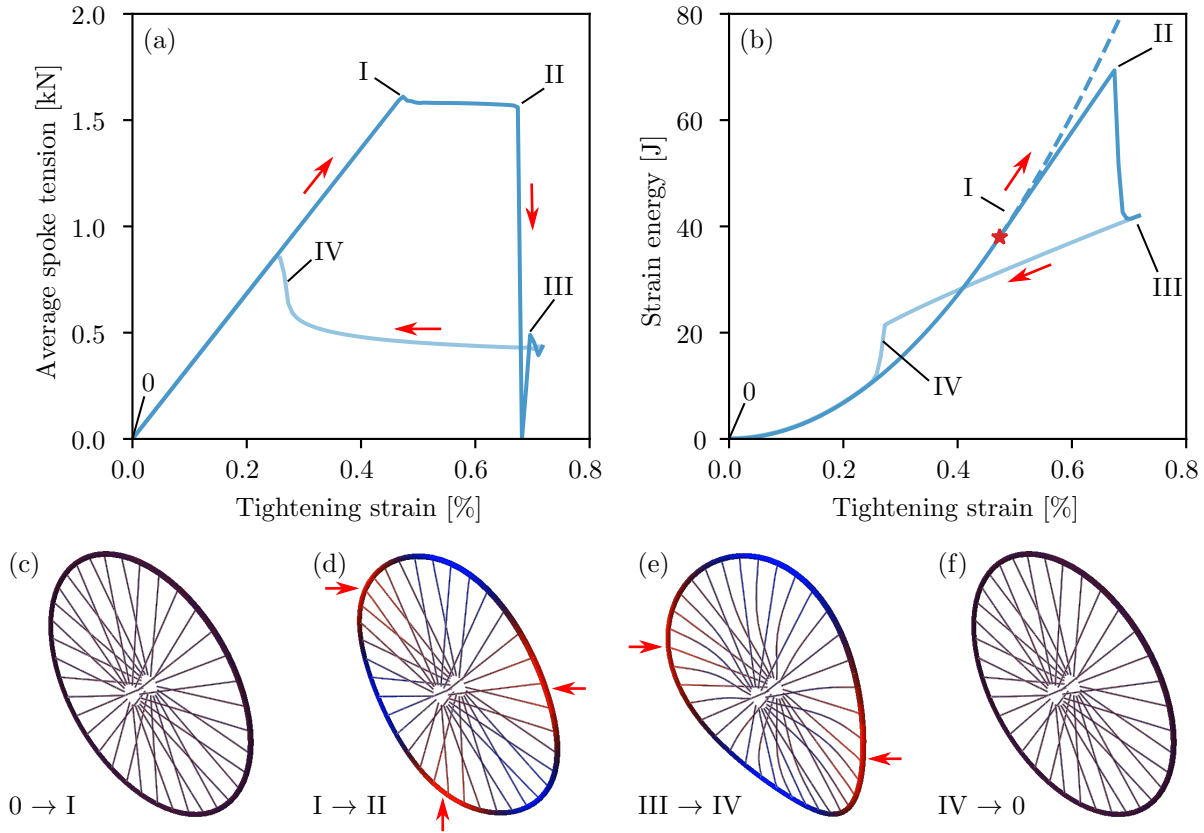


Figure 4.2. Non-linear post-buckling behavior under spoke tensioning. (a) Tension diagram and (b) energy diagram showing a bifurcation instability at I and unstable collapse at II. (c)-(f) Stages of the tensioning-detensioning cycle showing uniform tensioning (0-I) accompanied by radial shrinkage of the rim, bifurcation buckling (I-II) accompanied by lateral-torsional deformation in the $n = 3$ mode, detensioning of spokes (III-IV) along a collapsed equilibrium branch, and recovery of the planar shape (IV-0).

given a geometric imperfection in the lateral coordinate (a “wobble”) including several modes of the form $\cos n\theta$. The solution was obtained by implicit integration including non-linear geometric effects. The average spoke tension was recorded at each loading step. The buckling tension was determined as the point at which the tension vs. strain curve deviated by more than 2% from linearity. Results are plotted against theory in Fig. 4.1 (b) and (c).

In addition to global buckling, the wheel can exhibit local buckling if any of the spokes lose tension during deformation. The initial post-buckling behavior of the bicycle wheel under tension is stable. After

bifurcation, further tensioning of the spokes deforms the rim at roughly constant or slowly rising average tension. Since the buckling load of a spoke is much smaller than the initial tension, it exerts essentially no force on the rim when buckled. Therefore, local buckling of the spokes leads to a loss of stiffness which can cause global collapse. During collapse, strain energy stored during tensioning is released and the system finds a new minimum energy configuration.

Figure 4.2 illustrates a dynamic finite-element simulation of a complete tensioning-detensioning cycle, implemented in ABAQUS Explicit. The spoke tensions increase uniformly until the equilibrium path bifurcates at point I. The rim follows the lower-energy path I \rightarrow II by buckling and twisting out of its initial plane. As the spokes are tightened further, the rim deforms to accommodate the change in length. Although the average spoke tension remains constant, individual spokes increase or decrease their tension depending on which side of the rim they are on. At II, the spoke at the peak of each wave buckles, which reduces the overall stiffness of the structure causing it to collapse to III.

The collapse at point II may also involve a mode transition. Depending on the properties of the wheel, the lowest bifurcation mode may be $n > 2$. A rim with no spokes will always buckle into the lowest mode $n = 2$, however the spoke stiffness may stabilize higher modes. When spokes buckle, the stiffness drops suddenly causing the system to prefer the $n = 2$ mode.

4.3. Closed-form solutions for special cases

The critical tension in Eqn. (4.5) is not in closed form due to the need to minimize $\tau_{c,n}$ with respect to n . In the following sections I will consider several special cases with approximate solutions which transform Eqn. (4.5) into a closed-form power law.

4.3.1. Low torsional stiffness

As the ratio GJ/EI_2 tends towards zero, the mode number n tends towards infinity. When the mode number is large, the buckling mode can then be found by approximating the discrete mode number n with a continuous variable \bar{n} . We will adopt the following ansatz: (a) $\bar{n}^2 \gg 1$, and (b) $\mu\bar{n}^2 \ll 1$. Under these

conditions, Eqn. (4.5) becomes

$$(4.7) \quad \tau_{c,n} = \left(\mu \bar{n}^4 + \frac{\lambda_{uu}}{\bar{n}^2} \right)$$

Minimizing (4.7) with respect to \bar{n} yields

$$(4.8) \quad \bar{n}_c = \left(\frac{\lambda_{uu}}{2\mu} \right)^{1/6}$$

Inserting (4.8) into (4.7), we obtain the critical buckling tension, independent of mode number:

$$(4.9) \quad \tau_c = \left(\frac{1}{2^{2/3}} + 2^{1/3} \right) \mu^{1/3} \lambda_{uu}^{2/3}$$

Substituting definitions for dimensionless quantities τ, μ, λ_{uu} , we obtain a critical buckling tension which is independent of lateral bending stiffness, EI_2 :

$$(4.10) \quad \bar{T}_c = 1.89 \left(\frac{GJ}{R} \right)^{1/3} \bar{k}_{uu}^{2/3}$$

Equation (4.10) further illustrates the consequences of over-designing the bending stiffness while neglecting the torsional stiffness. Since the bending and torsion stiffnesses act like equivalent springs connected in series, the stiffness—and therefore the buckling resistance—will be dominated by the smaller of the two. Thus a very wide, but very shallow rim (e.g. a “fat-bike” rim) will be entirely dominated by its torsional stiffness.

4.3.2. Moderate torsion stiffness, stiff spoke system

Modern rims are often constructed from hollow extruded aluminum profiles. As a result they have high torsional resistance GJ and negligible warping coefficient EI_w ($GJ \sim EI_2$ and $EI_w = 0$). If the spoke stiffness is much higher than the rim stiffness, i.e. $\lambda_{uu} \gg 1$, then we can make a similar argument as in the previous section. Now we will accept as an ansatz that $n^2 \gg 1$ and $\mu \sim 1$. Estimating the discrete variable n with a continuous analog \bar{n} , Eqn. (4.5) becomes

$$(4.11) \quad \tau_{c,n} = \left(\bar{n}^2 + \frac{\lambda_{uu}}{\bar{n}^2} \right)$$

Minimizing (4.11) with respect to \bar{n} gives the scaling law $\bar{n}_c = (\lambda_{uu})^{1/4}$. Inserting into (4.11) gives $\tau_c = 2(\lambda_{uu})^{1/2}$. In terms of the net radial tension per unit length, \bar{T} , this gives

$$(4.12) \quad \bar{T}_c = 2 \left(\frac{\bar{k}_{uu}^{matl} E I_2}{R^2} \right)^{1/2}$$

Noting that the axial force in the rim is $F_3 = R\bar{T}$, we recognize (4.12) as the critical buckling load for an infinite beam on an elastic foundation given by Hetenyi [37]. The rim buckles as if it were a straight beam since λ_{uu} implies that the rim radius is large compared to the characteristic length of the beam on an elastic foundation.

4.3.3. All spokes lie in the plane of the wheel

If all the spokes were laced to the same flange of the hub, the spokes will all lie in the plane of the rim, implying $\bar{k}_{uu}^{matl} = 0$. In this case, the rim will always buckle into the $n = 2$ mode and Eqn. (4.5) simplifies to

$$(4.13) \quad \tau_c = \left(\frac{9\mu}{1 + 4\mu} \right) \left(\frac{4}{4 - R\bar{k}_{uu}^{geom}} \right)$$

If the spokes meet at the center of the rim (i.e. a hub of zero diameter), then $R\bar{k}_{uu}^{geom} = 1$ and the critical reduced tension becomes

$$(4.14) \quad \tau_c = \frac{12\mu}{1 + 4\mu}$$

This is precisely the result obtained by Hencky for the critical distributed radial load for a thin ring [85]. Timoshenko obtained a slightly different result which differs from Eqn. (4.14) by a factor of 3/4, by considering dead loads which do not change direction during buckling. This case illustrates the importance of considering the geometric stiffness when deriving the spoke forces. The change in direction of the spoke force after deflection produces a small restoring force on the rim which increases the buckling load by a factor of $1/(n^2 - R\bar{k}_{uu}^{geom})$, or about 33% for $n = 2$. Wheels with larger R/l_s , and thus a larger change in spoke angle for a given lateral deflection—for example high-flange hubs or hub motors—will receive an even larger benefit from the geometric stiffness term.

4.4. Experimental measurement of buckling tension

Several practical considerations make it difficult to reach the critical tension in a real wheel: (1) the buckling tension can be higher than the yield point of the spoke itself, (2) friction at the spoke nipple/rim interface becomes too great to overcome with a spoke wrench, and (3) the rim goes out of true laterally at around 50% of the critical tension due to imperfections in the rim.

Despite these difficulties, the mode stiffness model described in Section 2.6.1 provides a method of estimating the critical buckling tension by directly measuring the stiffness of a single mode ($n = 2$) as a function of spoke tension. Under the assumptions described in 2.6.1, the stiffness of the n th mode is:

$$(4.15) \quad K_n(T) = K_n^{rim} + \pi R(\bar{k}_{uu}^{matl} + \bar{T}\bar{k}_{uu}^{geom}) - \pi n^2 \bar{T}$$

The linear dependence of \bar{k}_{uu} on \bar{T} is made explicit in Eqn. (4.15) to show that K_n also depends linearly on \bar{T} . By measuring the $n = 2$ mode stiffness at multiple spoke tensions and then extrapolating the data to $K_2 = 0$, the critical tension $\bar{T}_{c,n}$ can be estimated.

4.4.1. Method

I measured K_2 at multiple tensions for five wheels, all constructed with the same rim and spokes but with varying distance between hub flanges¹. For each wheel, I increased the spoke tension until the wheel started to buckle enough to create a significant difference between left and right spoke tensions at the anti-nodes of the rim.

Wheel construction. The rim was a Sun Ringle CR18 700C, a narrow double-wall box-section rim drilled for 36 spokes. The spokes were Wheelsmith double-buttet spokes with an end diameter of 2.0 mm and 1.70 mm along the swaged section. The spokes were attached radially to the hub oriented with the spoke heads on the outside of the hub (inbound spokes). The hub was a custom-built adjustable-width hub designed by a Northeastern University capstone team advised by Jim Papadopoulos [4]. I made no special effort to keep the wheel laterally or radially true to a tight tolerance, but the rim was symmetrically dished and I ensured that no individual spoke deviated in tension by more than 10% of the average tension. This eventually

¹Other than the varying hub flange spacing, the properties are identical to those of the Standard Research wheel with inbound spokes, Appendix B.1.

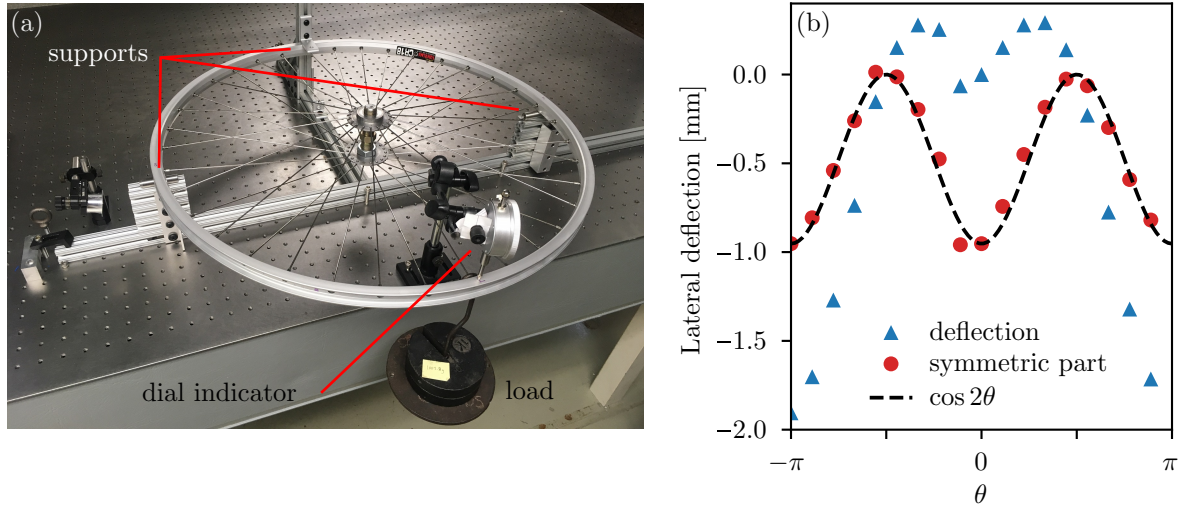


Figure 4.3. Four-point bending test. (a) Experimental setup showing load fixture, applied load, and measurement point. (b) Measured lateral displacement around the rim when loaded at $\theta = -\pi$. The symmetric part of the displacement is found by subtracting $(u_l/2) \cos \theta$ from the measured displacement.

became impossible when the average spoke tension exceeded about 50% of the critical tension and the wheel started to distort into a taco shape.

Four-point bending test. Each wheel was supported on steel pins from the bottom at the 3, and 9 o'clock positions and from the top at 12 o'clock, and loaded by hanging weights at the 6 o'clock position (Fig. 4.3 (a)). The rim was oriented so that the sleeve joint and the valve hole fell midway between supports where the bending moment is minimized. Due to the symmetry of the boundary conditions, the work done against the odd modes ($n = 1, 3, \dots$) and even modes divisible by 4 ($n = 4, 8, \dots$) is identically zero. Since the hub is unsupported, the zero mode is also eliminated. Due to the rapid increase in mode stiffness with n , the $n = 2$ mode accounts for about 95% of the strain energy, while the other 5% is spread across the remaining modes ($n = 6, 10, \dots$).

Figure 4.3 (b) shows the measured lateral displacement around the rim for a point load located at $\theta = -\pi$. After subtracting the rigid body rotation, the measured displacement closely matches $\cos 2\theta$. The second mode stiffness is related to the load-displacement slope of the four-point bend test by $K_2 = 16(P/u_l)$, where P is the applied load and u_l is the deflection of the load point.

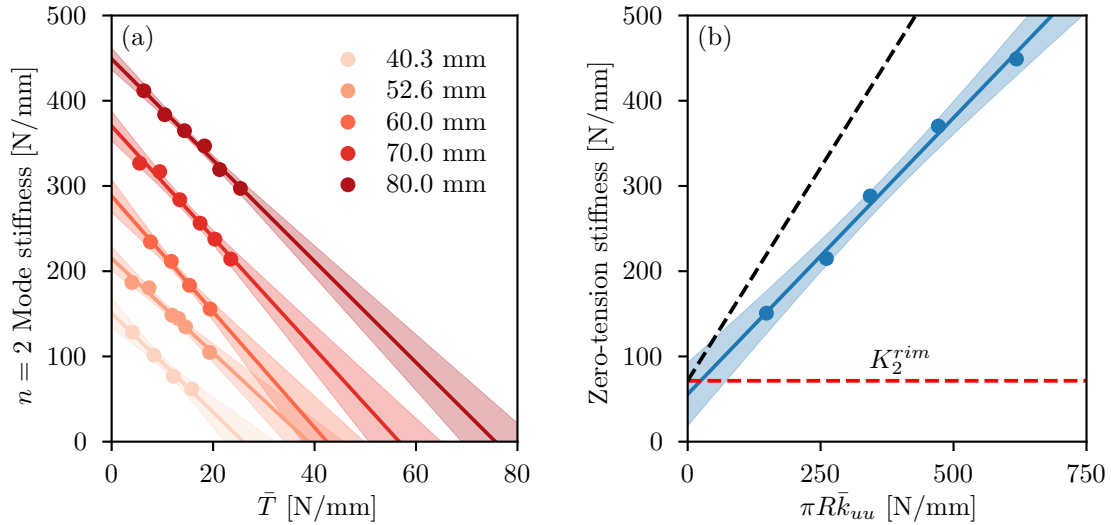


Figure 4.4. Four-point bending test results. **(a)** Measured mode stiffness vs. spoke tension for five different hub flange spacings. **(b)** Extrapolated mode stiffness at zero tension vs. the spoke system stiffness. The red dashed line is the rim mode stiffness, while the black dashed line is the theoretical mode stiffness from Eqn. (4.15). The bounds on all linear fits correspond to the 95% confidence interval.

4.4.2. Results

As predicted by Eqn. (4.15), the measured mode stiffness decreases with applied tension (Fig. 4.4 (a)). The dominant role of the spoke system in determining the wheel stiffness is apparent in the dramatic increase in stiffness from the narrowest hub (40 mm) to the widest hub (80 mm). Although the stiffness cannot be measured at zero tension due to buckling of spokes, the extrapolated zero-tension stiffness was obtained by linear regression. The zero-tension stiffness increases linearly with \bar{k}_{uu} . A theoretical wheel with zero hub width and zero tension has a stiffness equal to the stiffness of the rim alone. The rim stiffness for the CR18 700C rim, 71 N/mm, was measured using the technique described in Chapter 3 (shown as a red dashed line in Fig. 4.4 (b)).

There are two notable discrepancies between the experimental results and the stiffness predicted by Eqn. (4.15). First, the material component of the spoke stiffness (proportional to K_s and independent of tension) is lower than the theoretical stiffness by about 35%. The extrapolated zero-tension stiffness should increase commensurately with $\pi R \bar{k}_{uu}$ (black dashed line in Fig. 4.4 (b)). This is possibly due to the fact that the

J-bend spokes used in this study are able to deform elastically near the spoke due to the loose fit of the spoke elbow in the hub flange.

Second, the dimensionless slope K_2 vs. \bar{T} is -6.30 ± 0.25 , while the slope predicted by Eqn. (4.15) is approximately $-3\pi = -9.42$. The positive difference suggests that increasing the tension causes the spokes to recover some stiffness, possibly by increasing the contact force between the spoke elbow and the edges of the hole in the hub flange. The details of the stiffness of J-bend spokes under tension is the subject of an ongoing research project.

CHAPTER 5

Buckling under external loads

Most modes of mechanical failure of the wheel are progressive and preventable: gradual loosening of spokes leads to misalignment, repetitive stressing of the spokes leads to localized failure by fatigue, wear from rim brakes thins the rim sidewalls and increases the likelihood of tire blow-outs. The wheel can also fail suddenly under excessive loads by buckling. Many cyclists know this failure mode as a “taco,” due to the tendency of the wheel to form a saddle-like shape and fold in on itself.

Thus far we have only considered buckling under internal forces (which is primarily a concern of the wheelbuilder, not the rider), and small deformations of the wheel under external loads such that the structural response remains linear. There are two sources of nonlinearity under large deformations: (1) material nonlinearity, in which the constitutive law of the material itself is nonlinear—e.g. plasticity—and (2) geometric nonlinearity, in which the deformation of the structure is large enough such that the small-angle



Figure 5.1. A bicycle with a buckled wheel, spotted on Northwestern’s campus.

approximation is no longer valid. Here we will assume that material nonlinearity is not present. A typical bicycle rim is a slender structure capable of large deformations with small strains. Furthermore, the onset of plasticity will depend on the exact shape of the rim cross-section.

For validation and illustration, I present non-linear finite-element simulations on seven hypothetical wheels. The wheel properties are given in Appendix B.3. The “high wheel” represents the kind of wheel that would be found on an Ordinary, or “penny-farthing,” bicycle popular in the 1880s. The “small” wheel might be found on an adult folding bicycle or a youth bicycle. All of the properties are hypothetical and are not meant to correspond to any particular wheel or product.

5.1. Buckling under lateral force

The wheel is considerably weaker in the lateral direction than the radial direction due to the small out-of-plane bracing angle. Relatively small side loads can buckle spokes or cause the entire rim to collapse. Lateral failure occurs as a result of two complimentary failure mechanisms: buckling of spokes due to insufficient tension, and buckling of the rim due to excessive spoke tension. Increasing the spoke tension increases the lateral displacement required to de-tension spokes, but decreases the lateral stiffness due to the compressive axial stresses in the rim.

To illustrate these two competing failure mechanisms, I performed finite-element simulations in ABAQUS 6.13 using the “vintage road” wheel parameters. The hub is rigidly fixed, while the lateral load and lateral displacement of a point on the rim are simultaneously calculated using a version of the Riks algorithm [16]. Arc-length methods like the Riks algorithm are capable of tracing load-displacement curves which exhibit both snap-through instabilities (unstable under load control) and snap-back instabilities (unstable under displacement control).

Figure 5.2 (b) shows the calculated load-displacement curves for the same wheel at seven different tensions corresponding to $T = 0.1T_c, 0.2T_c, \dots, 0.7T_c$. The initial behavior is linear until the onset of spoke buckling. After the peak load, there is a load drop with a corresponding release of potential energy stored during the prestressing process and the rim buckles into a taco shape. The magnitude of the load-drop (and corresponding snap-back instability) increases with spoke tension. Beyond a critical tension, the load-displacement curve crosses the zero-axis, indicating the existence of a buckled state which can be maintained

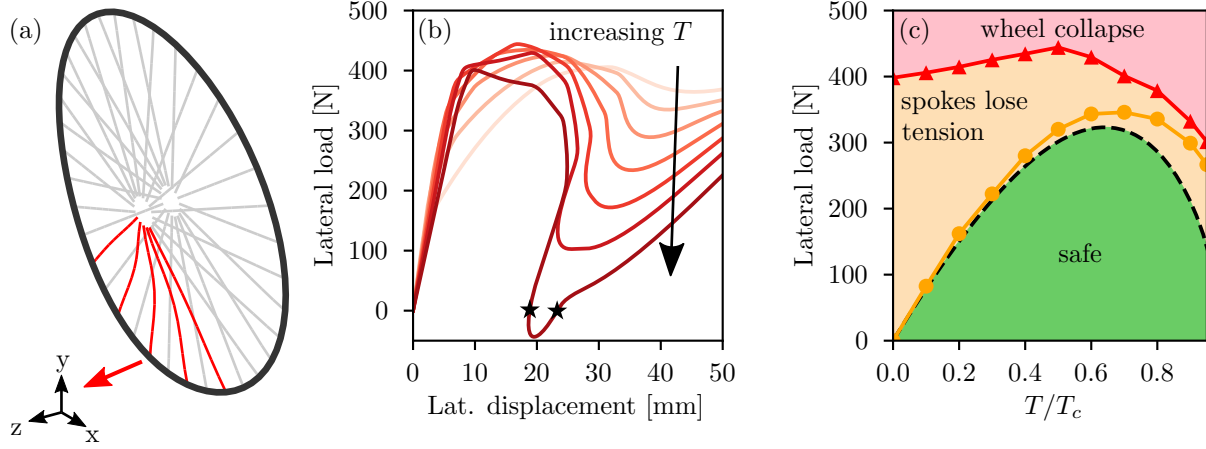


Figure 5.2. Buckling under lateral force. **(a)** Snapshot from ABAQUS simulation. The bottom node is displaced in the z -direction. The spokes opposite the side of the applied load (red) have lost tension. **(b)** Equilibrium load-displacement curves for the “vintage road” bike wheel at several spoke tensions. Lightest: $T = 0.1T_c$, darkest: $T = 0.7T_c$. **(c)** Failure diagram for the same wheel showing the region of no spoke buckling (green), buckled spokes but positive stiffness (yellow), and wheel collapse (red). The markers are from ABAQUS simulations and the dashed line is from Eqn. (5.2).

with no external load. Many a hapless wheelbuilder has discovered this equilibrium solution by vigorously stress-relieving a wheel at high tension. It is likely that Jobst Brandt was referring to this state in his practical advice quoted at the beginning of Chapter 4.

The competition between failure mechanisms of spoke buckling and rim collapse leads to a failure diagram like that shown in Fig. 5.2 (c). The lateral displacement required to buckle spokes is

$$(5.1) \quad u_{sb} = \frac{T}{K_s c_1}$$

where K_s is the axial stiffness of a spoke and c_1 is the direction cosine of the spoke in the \mathbf{e}_1 (lateral) direction. Converting the buckling displacement u_{sb} to a load using the tension-dependent lateral stiffness, $K_{lat}(T)$, we obtain the lateral load to buckle a single spoke:

$$(5.2) \quad P_{sb} = \frac{K_{lat}(T)T}{K_s c_1}$$

The failure diagram shown in Fig. 5.2 (c) suggests a simple rule-of-thumb for the optimum spoke tension for supporting side loads: A rough but satisfactory approximation to the tension-dependent lateral stiffness for a wheel is $K_{lat}(T) = K_{lat}^0(0)(1 - T/T_c)^1$, where K_{lat}^0 is the theoretical lateral stiffness at zero spoke tension. Inserting this approximation into Eqn. (5.2) and maximizing the lateral force gives an optimum spoke tension of $T_{opt} = 0.5T_c$. For typical wheels, this is just below the spoke tension which admits equilibrium buckled states, and just below the tension at which the pre-buckling of the rim due to imperfections becomes intolerable. I therefore propose that Brandt’s tension criterion, developed through practical experience, in fact has a theoretical basis.

5.2. Buckling under radial force

The buckled shape of the wheel under radial load is very similar to the buckled shape under lateral load. At a critical radial load the wheel takes on a non-planar shape by lateral bending and twisting. The subsequent post-buckling stiffness is generally zero or negative (unstable), which leads to collapse under dead loads. In a typically wheel, radial load causes spokes to buckle in a narrow region beneath the hub before global buckling. Therefore, the pre-buckling structural response is non-linear. Furthermore, the pre-buckling displacements can be quite large and so cannot necessarily be neglected.

For these reasons a theoretical prediction of the critical radial load is an extremely challenging task. Nevertheless, a satisfactory approximation may be obtained by separately considering the two competing failure modes: spoke buckling and rim buckling. In this section I will derive an approximate formula [24] for the radial strength based on the following assumptions:

- (1) The maximum radial load does not depend significantly on spoke tension.
- (2) The buckling mode shape is identical to the deformed shape of the wheel under a small lateral load.
- (3) During buckling, the point on the rim where the load is applied moves along a circular trajectory whose center lies at the center of the wheel (inside the hub) in the plane defined by the basis vectors \mathbf{e}_1 and \mathbf{e}_2 .
- (4) The radial load at which spokes begin to buckle is proportional to spoke tension.

¹The approximation is identical to the “knock-down factor” or “amplification factor” used in the design of beams or columns which carry both lateral and compressive axial loads [85]. Although it is almost exact for a straight beam-column laterally loaded at its midpoint, it is only approximately true, and conservative, for the bicycle wheel. See Fig. 2.7 for an illustration of K_{lat} vs. T for a typical wheel.

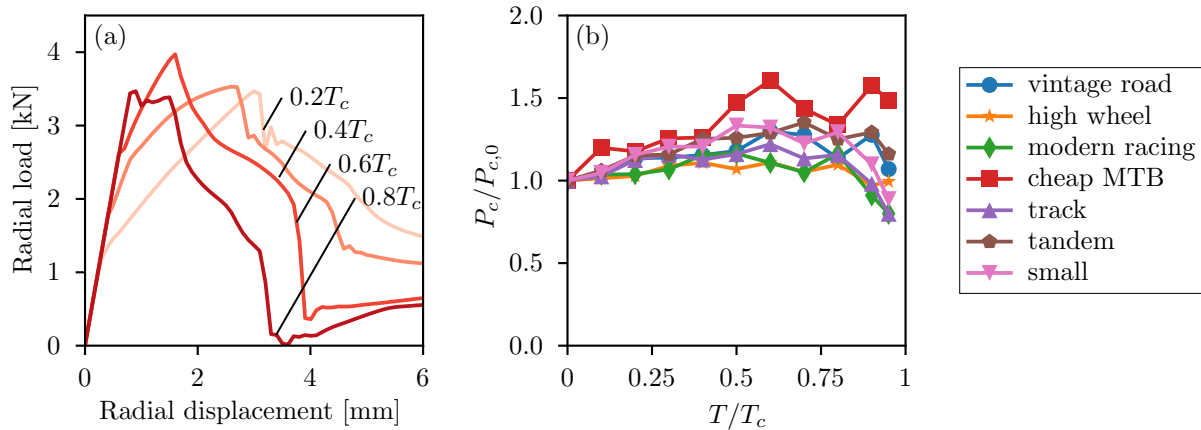


Figure 5.3. ABAQUS simulations of radial buckling at different spoke tensions. **(a)** Load-displacement curves for the vintage road bike wheel at different spoke tensions. **(b)** Buckling load, normalized by buckling load at $T = 0$ vs. normalized spoke tension.

5.2.1. Effect of spoke tension

A range of typical load-displacement curves for symmetric wheels under radial load are shown in Fig. 5.3 (a). Initially, the load is proportional to the radial displacement. At a first critical load P_{sb} depending on the spoke tension, the spoke or spokes directly underneath the hub lose tension causing a sudden change in stiffness. The load continues to rise as nearby spokes participate in balancing the load. At a second critical load P_c , the lateral stiffness of the wheel (now reduced due to the buckled spokes) is no longer sufficient to maintain a planar shape and the rim begins to deflect laterally. Beyond this point, the post-buckling stiffness is negative, leading to unstable collapse under load control. If the spoke tension is sufficiently high, there is a second collapse point at which the inward pull of the spokes on the already-distorted rim causes it to collapse into a fully-developed taco shape. This collapsed shape may remain after the radial load is removed, even if the material behavior is fully elastic.

Increasing the spoke tension increases P_{sb} because the spokes can lose more tension before going slack. However, it also reduces the lateral stiffness. These two effects very roughly balance each other so that changing the spoke tension does not have a large effect on the peak radial load (Fig. 5.3 (b)). A low-tension wheel buckles at a much higher radial displacement, but at roughly the same force as a high-tension wheel. This trade-off is the basis of assumption (1).

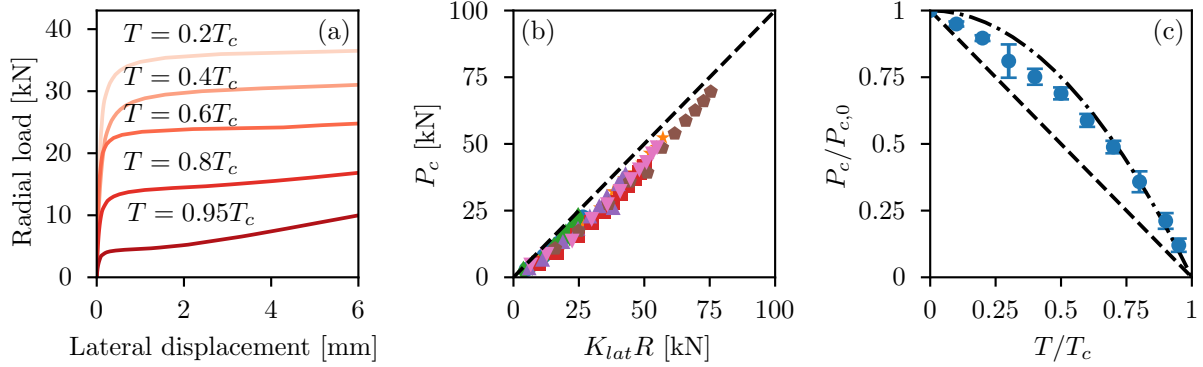


Figure 5.4. ABAQUS simulations of radial buckling with laterally restrained spokes. (a) Radial load vs. lateral displacement for cheap MTB wheel at several tensions. The lateral displacement follows a classical bifurcation buckling path, dependent on spoke tension. (b) For a wide range of wheel types and spoke tensions, the critical radial load is well approximated by $P_c = K_{lat}R$. Markers and colors same as Fig. 5.3 (b). (c) Critical radial load normalized by critical radial load for the same wheel at $T = 0$.

5.2.2. Rim buckling with laterally constrained spokes

If the spokes are laterally constrained so that they do not buckle, the structural response remains linear up to the point of rim buckling. At a critical load, the rim undergoes a bifurcation instability and the lateral displacement increases sharply. The critical load decreases with tension, as shown in Fig. 5.4 (c).

Single-degree-of-freedom rim buckling model. Since spoke buckling no longer plays a role when the spokes are laterally constrained, we can isolate the rim buckling failure mode. Under the assumptions outlined above, an analytical solution for the bifurcation load is possible.

As the rim deflects laterally, the radial load projects a small lateral component onto the rim. Since the lateral stiffness is much less than the radial stiffness, I assume that the effect of the radial displacement on the deformed lateral shape is negligible, and that the deformed shape of the rim is identical to the deformed shape under a pure lateral load (assumption (2)). Therefore the deformed shape is fully characterized by a single parameter: the lateral deflection of the load point u_l . A direct result of this assumption is that the increase in strain energy under a virtual displacement δu_l is exactly

$$(5.3) \quad U = \frac{1}{2}K_{lat}\delta u_l^2$$

If the extension of the rim centerline during buckling is assumed to be zero, the rim must pull in radially as it deflects laterally. I assume that the buckling path of the load point follows a circular trajectory shown in Fig. 5.5 (b) (assumption (3)). During buckling, the load P moves through a virtual displacement δv_l . The corresponding reduction in potential energy of external loads is

$$(5.4) \quad V = -P\delta v_l = -P\delta u_l \left(R - \sqrt{R^2 - \delta u_l^2} \right) \approx -P \left(\frac{\delta u_l^2}{2R} \right)$$

Taking the second variation of the total potential energy $U - V$ yields the stability criterion:

$$(5.5) \quad \delta^2 \Pi = K_{lat} - \frac{P}{R}$$

The critical bifurcation load is

$$(5.6) \quad P_c = K_{lat} R$$

Finite-element results are compared against Eqn. (5.6) in Fig. 5.4 (b). The single degree-of-freedom buckling model gives a satisfactory approximation over almost two orders of magnitude. Increasing the spoke tension reduces the lateral stiffness (see Section 2.6) in a predictable manner. The buckling load as a function of tension can be approximated with a simple linear model (Fig. 5.4 (c), dashed line):

$$(5.7) \quad \frac{P_c}{K_{lat}^0 R} = 1 - \frac{T}{T_c}$$

where K_{lat}^0 is the lateral stiffness at zero spoke tension.

Hinged-column model. The single degree-of-freedom wheel buckling model suggests an analogy with the system shown schematically in Fig. 5.5 (b). A rigid column, pinned at one end, is restrained by a linear spring at the tip and a torsional spring at the pivot. The deformation is completely characterized by the rotation angle, ϕ .

The total potential energy in the deformed configuration is

$$(5.8) \quad \Pi = \frac{1}{2} k_u (R \sin \phi)^2 + \frac{1}{2} k_\phi \phi^2 - PR(1 - \cos \phi)$$

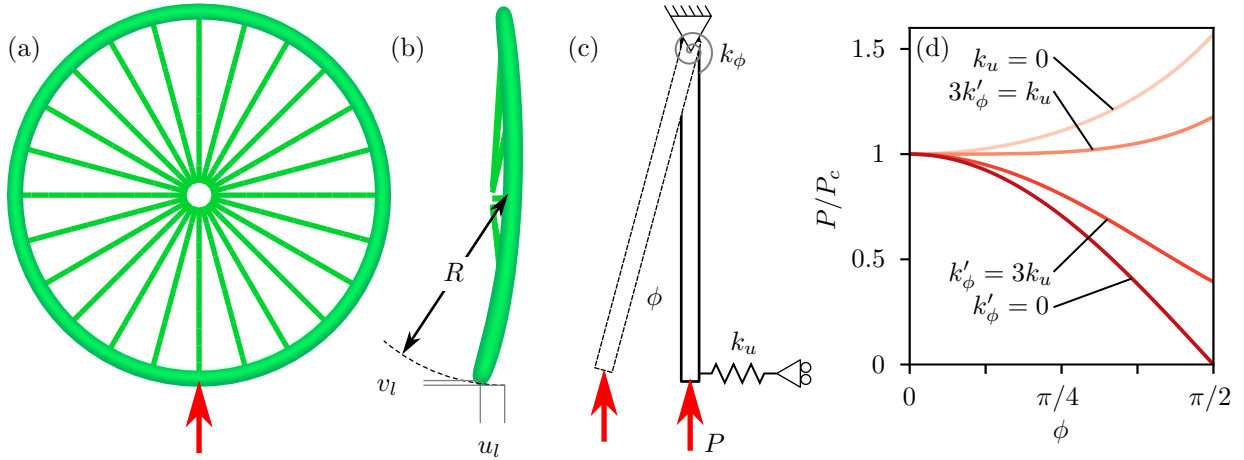


Figure 5.5. **(a)-(b)** Single-degree-of-freedom model of bicycle wheel buckling. The load point is assumed to move along a circular trajectory. **(c)** Buckling of a rigid, hinged, elastically restrained column. **(d)** Post-buckling curves for the rigid hinged column model. The post-buckling stability depends on the relative stiffness of the linear and rotational springs.

Setting the first variation of (5.8) to zero gives the equilibrium condition.

$$(5.9) \quad k_u R^2 \sin \phi \cos \phi + k_\phi \phi - PR \sin \phi = 0$$

The two possible solutions to (5.9) are

$$(5.10) \quad \begin{cases} \phi = 0 \\ P = \frac{k_\phi}{R} \left(\frac{\phi}{\sin \phi} \right) + k_u R \cos \phi \end{cases}$$

The torsional stiffness can be re-expressed in terms of the effective lateral stiffness of the column at its tip $k'_\phi = k_\phi/R^2$. The trivial solution bifurcates at the critical load $P_c = (k'_\phi + k_u)R$. Note the similarity between this result and the critical load for the single degree-of-freedom wheel model, Eqn. (5.6).

Expanding (5.10) about $\phi = 0$ and retaining only up to second-order terms, we obtain

$$(5.11) \quad P = P_c + \left(\frac{1}{6}k'_\phi - \frac{1}{2}k_u \right) R\phi^2 + \dots$$

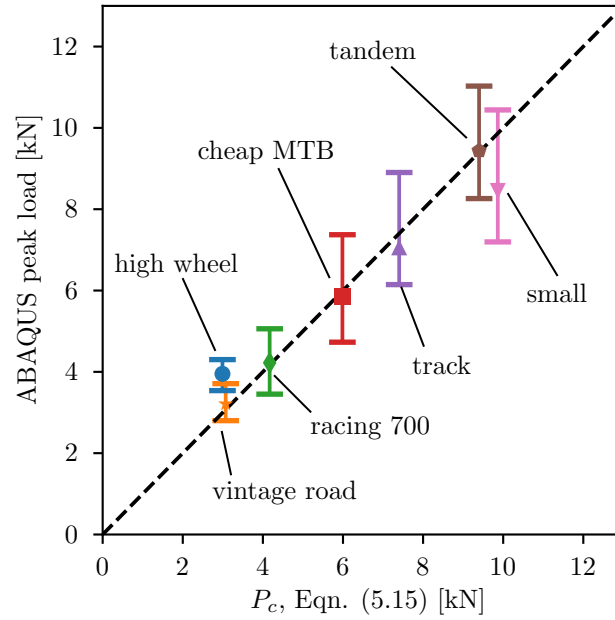


Figure 5.6. Comparison of competing failure modes model, Eqn. (5.15), with ABAQUS radial buckling simulations. The markers represent the mean buckling load for a range of spoke tensions from $T = 0$ to $T = 0.95T_c$, while the error bars correspond to the full range of buckling loads for each wheel.

The post-buckling behavior of the column is stable (increasing load) only if the second term is positive.

This condition can be expressed as

$$(5.12) \quad \begin{aligned} k'_\phi &> 3k_u \text{ stable} \\ k'_\phi &\leq 3k_u \text{ unstable} \end{aligned}$$

5.2.3. Competing failure mode model

Since the load-displacement curve is linear up to the point of spoke buckling (assumption (4)), the load required to buckle the bottom-most spoke is

$$(5.13) \quad P_{sb} = \frac{K_{rad}T}{K_s c_2}$$

where K_{rad} is the radial stiffness of the wheel, K_s is the elastic stiffness of the spoke, and c_2 is the direction cosine of the spoke in the \mathbf{e}_2 (radial) direction. Unlike the lateral stiffness, the radial stiffness is not significantly sensitive to spoke tension.

Combining Eqns. (5.13) and (5.7) and solving for T gives the tension at which spoke buckling and rim buckling will occur simultaneously:

$$(5.14) \quad T^* = \frac{T_c}{\left(1 + \frac{K_{rad}T_c}{K_{lat}^0 K_s R c_2}\right)}$$

Substituting (5.14) into (5.7), substituting the elastic stiffness for a straight-gauge spoke $K_s = E_s A_s / l_s$, and noting that $l_s \approx R$ and $c_2 \approx 1$ yields the critical load for simultaneous spoke and rim buckling:

$$(5.15) \quad P_c = K_{lat}^0 R \left(\frac{1}{1 + \frac{E_s A_s}{T_c} \frac{K_{lat}^0}{K_{rad}}} \right)$$

Equation (5.15) is now independent of spoke tension. The term in the parenthesis is always less than one, reflecting the fact that the wheel strength is reduced by spoke buckling. Despite the extreme simplicity of the model and the many assumptions employed, (5.15) gives a reasonable estimate of the strength of the seven types of bicycle wheels simulated. Furthermore, all the terms in (5.15) can either be directly measured or calculating using the formulas developed in this thesis.

Figure 5.6 compares the theoretical radial strength (Eqn. (5.15)) against results from non-linear finite-element simulations of the wheels described in Appendix B.3. In each simulation the wheel is first prestressed to a prescribed spoke tension by implicit integration in ABAQUS Standard. Next, the radial displacement is ramped linearly to a prescribed value which is beyond the peak load of the wheel. This segment is solved by explicit integration in ABAQUS Explicit. The error bars in Fig. 5.6 represent the full range of peak loads from ABAQUS results for wheels with spoke tensions ranging from $T = 0$ to $T = 0.95T_c$. The black dashed line has a slope of one.

5.2.4. Post-buckling behavior

The single-degree-of-freedom wheel model and the hinged-column model have the same critical behavior (buckling load equal to the lateral stiffness times radius). The post-critical behavior of the hinged-column

5.3. Radial buckling experiments

Mechanical engineering undergraduate students at Northwestern complete a capstone design project as a degree requirement. Each capstone team, consisting of 5-7 students, works with a sponsoring client over the course of 20 weeks to design and implement a solution to a relevant problem. Project sponsors may come from academia, industry, or the non-profit sector. Teams are given broad latitude in the design of their project and work closely with their client to develop a rigorous set of product needs and metrics.

During the Winter/Spring 2018 quarters I sponsored a capstone project to design a mechanical testing machine capable of applying a combination of radial and lateral loads to a bicycle wheel. The team—Tina Dornbusch, Patrick Doyle, Duncan Lamb, Jonathan Sammon, Olivia Schneider, Spencer Simon, and Emma Wilgenbusch²—designed a load frame which integrates into an existing United SFM-50KN Universal tension/compression testing machine.

The Northwestern (NU) capstone project followed a similar capstone project at Northeastern University (NEU) by Joseph Alim, Mehdi Lamnyi, Alexandra Koukhtieva, and Simon Tebbe sponsored by Professor Jim Papadopoulos [4]. The NU project built on some of the successes of the NEU project—particularly the adjustable hub and LVDT radial displacement measurement—and addressed some of its shortcomings such as manual operation, lateral friction, and non-integrated measurement.

5.3.1. Design of the wheel testing machine

The mechanical engineering capstone design course at Northwestern is organized and taught in collaboration with the Segal Design Institute. Teams follow a rigorous design process including patent research, user observation, product specification, mock-up creation, design review, testing and validation, and prototype iteration phases. The Northwestern capstone experience is unique in its rigor: students submit 20 intermediate status reports and 6 product design and testing reports over the course of two academic quarters. A more complete description of the iteration of the project is given in [20].

A list of product needs developed by the team is given in Table 5.1. The team also developed a set of quantitative metrics to address these needs, described in [20]. The testing apparatus is capable of

²Advised by Professor Michael Beltran, Professor J. Alex Birdwell, Ellen Owens, and me.

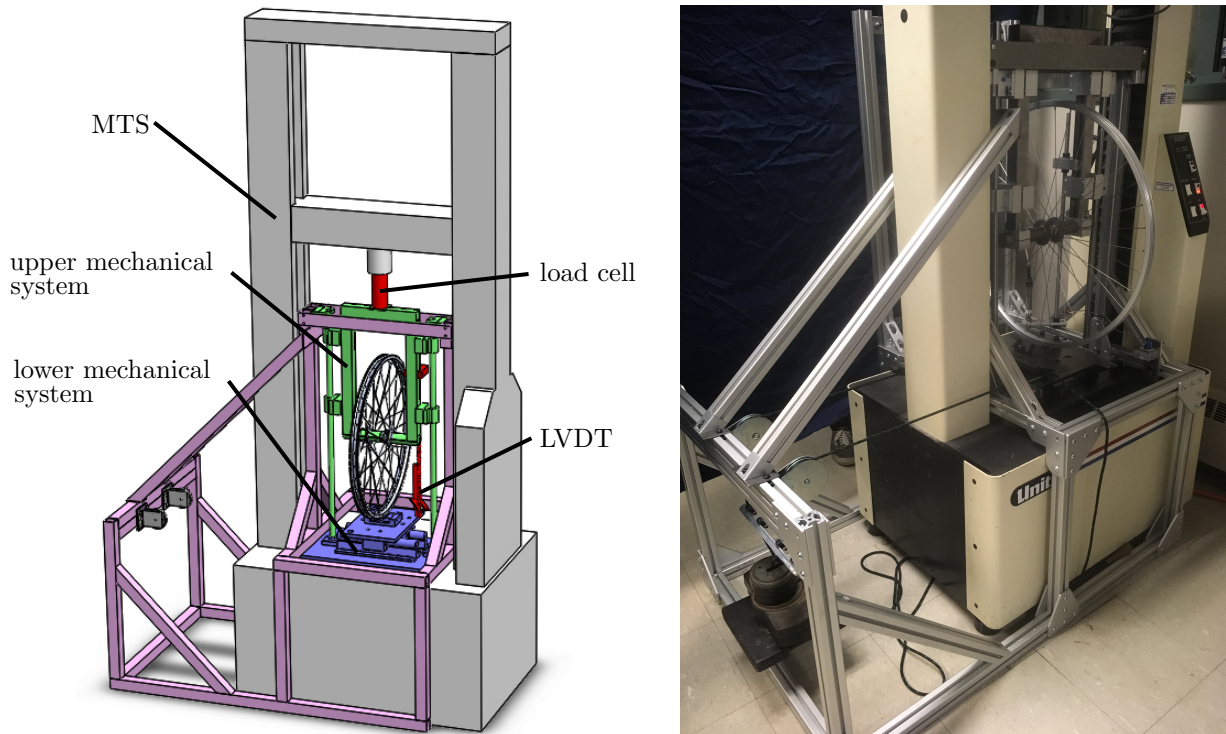


Figure 5.8. NU bicycle wheel testing machine. The pulleys on the left are for lateral load application. A weighted plate is hung from ropes routed over the pulleys and connected to the sliding plate. CAD and photo adapted from [20].

performing a radial-displacement-controlled test on a bicycle wheel, with an optional lateral dead load, while simultaneously measuring radial loads (up to maximum rated load of 12 kN), and radial and lateral displacement of the load point relative to the hub (with a resolution of $<10\ \mu\text{m}$ and $<100\ \mu\text{m}$ respectively). The apparatus is designed to constrain the position and rotation of the hub, but allow unconstrained lateral motion of the load point.

The testing apparatus, shown in Fig. 5.8, comprises the following subsystems: the **upper mechanical system** supports the hub, guides it along a vertical path, and interfaces with the MTS crosshead. The **lower mechanical system** contacts the rim, allows the application of lateral load, and allows lateral motion on precision linear bearings. The **safety subsystem** protects the operator and control system from projectiles³.

³The importance of this subsystem was demonstrated during a test of a 20" wheel when multiple spoke nipples ruptured simultaneously, ejecting the spokes at high velocity like arrows from a bow.

Table 5.1. Product needs developed by the team. Adapted from [20].

#	Need	Importance
<i>Performance Requirements</i>		
1	Is capable of bringing a wheel to the "tacoed" buckling mode	5
2	Provides contact points that accurately simulate real-life boundary conditions of bike wheel	5
3	Can perform a radial displacement-controlled test	5
4	Can apply fixed lateral dead load to wheel	4
5	Is able to position and hold wheel in desired/specified orientation about axle	4
6	Is able to carry out automated testing programs	3
7	Can apply load to a wheel with or without a tire	2
8	Measures and records radial load while testing	5
9	Measures and records radial displacement while testing	5
10	Measures and records lateral displacement while testing	4
11	Facilitates semi-automated or automated live data collection	4
12	Maintains full function after experiencing maximum loads	5
13	Survives repeated use over an extended lifetime	3
14	Accommodates a range of wheel diameters and widths	3
15	Has significantly higher stiffness than test specimens	5
<i>Standards and Compliance</i>		
16	Is able to interface with a variety of MTS machines with minimal reconfiguration/adjustment	4
<i>Manufacturing</i>		
17	Can be manufactured in a university environment	4
18	Can be manufactured within budget	5
<i>Assembly and Serviceability Considerations</i>		
19	Can be moved/transported with two to three people	4
20	Can be easily and accurately aligned for repeatable load application	4
21	Can be maintained/repaired with common tools	3
22	Allows easy access for maintenance and replacement of worn parts	4
<i>Assembly and Serviceability Considerations</i>		
23	Maintains safety of observers, operators, and surroundings	5
24	Prevents damage to MTS (both machine and sensors) when testing wheel	5

Finally the **control and instrumentation subsystem** measures displacements and loads in real time and controls the vertical motion of the MTS crosshead based on a preset control program.

Upper mechanical system. The NEU machine allowed the hub to slide laterally while holding the load point fixed at the top of the load frame. During testing it was discovered that the load point would slip under relatively small lateral loads, potentially applying a bending moment to the load cell. The NU team

chose to constrain the hub laterally, but allow vertical motion along linear bearings. The upper mechanical system comprises an external frame for lateral stiffness, vertical linear bearing rails, and a U-shaped carriage to guide the hub motion. Since friction in these rails would affect the measurement of radial load, the team measured the friction under a variety of lateral loads and determined that it would not affect the radial load measurement by more than 50 N (11.24 lb) under a worst-case loading scenario.

Lower mechanical system. Previously reported radial loading experiments on bicycle wheels constrained the lateral motion of the contact point [12, 1, 51]. This constraint artificially increases the radial stiffness and suppresses the lateral buckling mode of interest. The lower mechanical system allows both rotation of the rim cross-section and lateral displacement of the contact point. The bare rim is supported by a smooth steel pin which is sized to be lightly press-fit between the rim flanges. The pin is supported below between adjustable V-jaws (Fig. 5.9 (a)). The team measured a friction coefficient between the pin and jaws of less than 0.2, which they determined would have no appreciable effect on the test. A wheel with a tire can be tested by removing the pin and V-jaw assembly and placing the tire directly on the sliding plate.

The V-jaws are mounted on a steel plate riding on Thomson Linear SuperSmart pillow block bearings. The linear bearings run on fully-supported steel rails to minimize distortion under load. Lateral friction increases the apparent buckling load. The effect of lateral friction on the buckling load of a fixed-free column has been studied by Lazopoulos [47], who found a significant effect even at very small friction coefficients. Analogously modeling the bicycle wheel buckling problem as a straight column, Lazopoulos's model predicts that a friction coefficient of 0.01 would result in a 10% overprediction of the critical load⁴. The linear bearings used have a load-dependent friction coefficient, decreasing with increasing vertical load. The team experimentally measured the friction coefficient, achieving a minimum coefficient of 0.01 at a load of 2.8 kN (Fig. 5.9 (b)). At higher loads, an even smaller friction coefficient is expected.

Control and instrumentation subsystem. The control and instrumentation subsystem measures the radial displacement, lateral displacement, and radial load in real time and controls the position of the MTS crosshead. The vertical displacement of the U-carriage is measured relative to the load platten with a DC linear variable differential transformer (Schaevitz Sensors GPD-121-250 LVDT). The lateral displacement is measured by a string potentiometer (TE Connectivity SP1-12) connected to the lateral carriage. Optionally,

⁴This is likely conservative due to the presence of additional lateral compliance in the load frame.

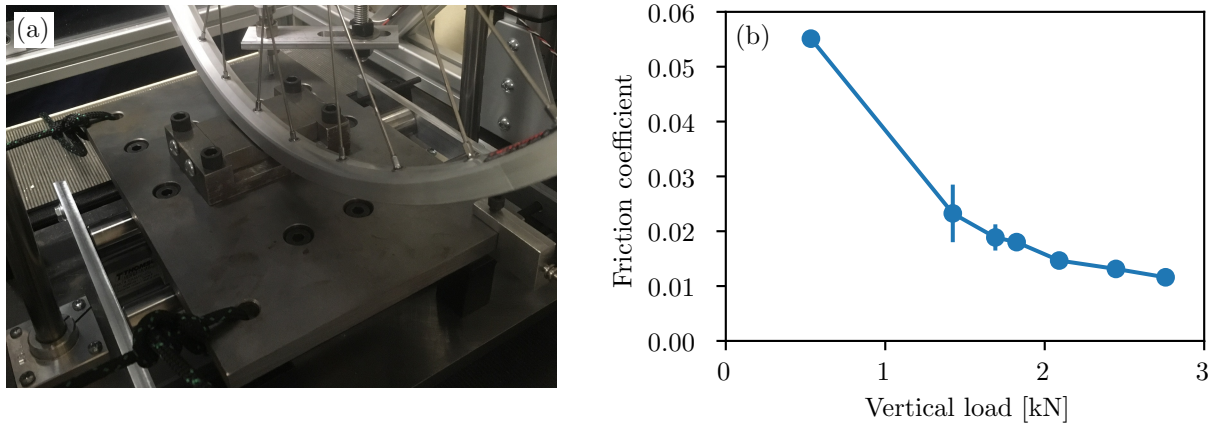


Figure 5.9. **(a)** Lateral carriage assembly without a bicycle wheel mounted. **(b)** Friction coefficient of the lateral bearings as a function of vertical load. The error bars represent the 95 % confidence interval from 4 tests.

the change in tension of a single spoke may be measured using a standard knife-edge extensometer with a 2-inch gauge length.

All sensors are read by the 24-bit analog-to-digital converter provided with the United Testing control hardware. The control software is capable of running preset testing routines with logic driven by sensor inputs (e.g. a program could be designed to load to 100 lb, then unload to 15 lb, then load until failure or a preset displacement).

5.3.2. Experimental procedure

Three bicycle wheels without tires were tested until lateral buckling failure. All three wheels were built from identical components to the same nominal specifications⁵. The maximum and minimum spoke tensions were kept to within $\pm 10\%$ of the mean tension. No special effort was made to make the wheels laterally or radially true, however some adjustment was made to Wheel 2 to remove an excessive lateral wobble without sacrificing tension uniformity. The spokes were stress-relieved prior to testing by the method described by Brandt [10].

⁵See Appendix B.1 for complete wheel properties

Table 5.2. Test parameters, selected results, and post-mortem properties.

	Wheel 1	Wheel 2	Wheel 3
Lateral dead load [N]	58	58	220
Peak radial load [kN]	4.49	4.39	3.51
Radial stiffness [kN/mm]	1.944 ± 0.006	1.999 ± 0.014	2.003 ± 0.005
Onset of non-linearity (5%) [kN]	2.79	1.85	2.14
Before test			
Spoke tension [N]	852 ± 21	862 ± 52	867 ± 33
Lateral tolerance [mm]	± 0.5	± 2.5	± 1
After test			
Spoke tension [N]	638 (1475, 0) ^a	694 (1409, 84)	722 (1150, 195)
Lateral tolerance [mm]	± 6.8	± 5.7	± 4.2

^a (max., min.) tension

The wheel was loaded directly at a spoke position. The wheel was first loaded to 100 lbs radial load to force the load pin to settle into the rim. Prior experiments showed that this load was sufficient to cause the pin to settle, but not sufficient to plastically deform the rim or spokes. Next, a small radial preload was put on the wheel and a lateral dead load was applied using a pulley and hanging weights connected to the lateral carriage. The dead load was applied in the direction opposite the side of the loaded spoke (i.e. if the wheel was loaded at a spoke connected to the left hub flange, the lateral load was acting to the right). Previous experiments had shown that the wheel naturally buckles in this direction without a bias load. The MTS crosshead was then moved downward at a fixed velocity until the radial load dropped below 90 % of the peak load. The wheel was then unloaded until the radial load dropped below 10 lb. After testing, each spoke tension was measured and the deformed lateral shape was measured using a dial indicator mounted to a bicycle wheel truing stand.

5.3.3. Results

Load-displacement and displacement-displacement curves for the three tests are shown in Fig. 5.10. The load-displacement curves exhibit the same three failure points as the ABAQUS simulations: (1) non-linearity caused by spoke buckling, (2) rim buckling associated with a sharp increase in lateral displacement, and (3) unstable rim collapse. In every case, the rim buckled in the direction of the applied lateral load opposite the loaded spoke.

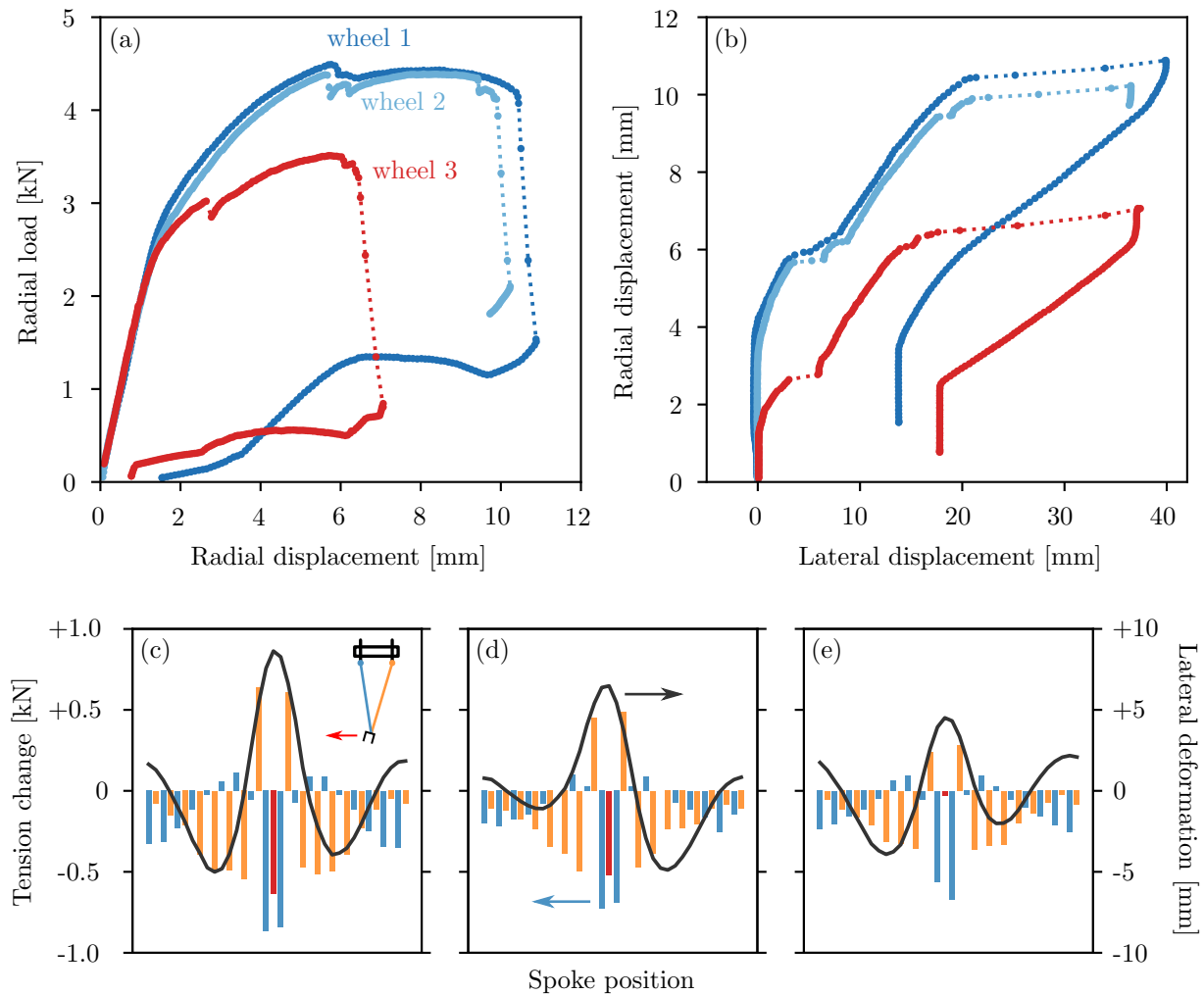


Figure 5.10. Radial buckling experimental results. (a) Load-displacement curves. (b) Displacement diagrams. (c)-(e) Post-mortem inspection of tested wheels showing change in spoke tension (bars) and lateral deformation (line). Blue bars represent the spokes on the same side as the lateral load (and buckling direction), while orange bars represent spokes on the opposite side (see cartoon inset in (c)). The spoke at the load is shown in red.

The lateral dead load significantly decreased the peak load and radial displacement to rim collapse: a +162 N (36.4lb) increase in lateral load decreased the peak radial load by 1000 N (220 lb). There is no obvious trend in spoke buckling load. Radial displacement has a much larger effect on spoke tensions, per unit displacement, than lateral loads due to the orientation of the spokes.

The residual deformed shape (black lines in Fig. 5.10 (c)-(e)) is that of an asymmetric “taco”. The average spoke tension has decreased, likely both due to radial yielding⁶ of the rim and yielding of some spokes. The three spokes near the load point (red bar and adjacent blue bars) for wheels 1 and 2 have lost most or all of their tension due to radial yielding. Away from the load point the pattern in residual spoke tensions follows the lateral displacement: at each “wave” the tensions are higher on the side opposite the direction of rim displacement. The influence of the radial deformation has completely disappeared at this distance. A wheel damaged in such a way is difficult or impossible to true by adjusting spoke tensions alone. The necessary adjustments to true the rim will exacerbate the difference in spoke tensions.

Wheel 3 shows less evidence of radial yielding of the rim than wheels 1 and 2: the spoke tension directly above the load maintained its original tension (the increase due to lateral rim motion is balanced by the decrease due to some possible radial yielding). No spokes in wheel 3 have gone completely slack.

All three tests were performed on wheels without tires in order to isolate the structural behavior of the wheel. The pin, set inside the rim cross-section and oriented with its axis in the plane of the wheel, effectively applied a point load to the rim. The localized loading is at least partially responsible for the localized yielding observed in these wheels. A tire would spread out the radial load to more spokes and possibly delay the onset of nonlinearity. However, since rim buckling and collapse are both global phenomena controlled more by the lateral stiffness of the rim, I speculate that a tire would not appreciably affect the peak load or collapse load.

5.3.4. Comparison with theory

In order to compare the experimentally-determined radial strength with Eqn. (5.15), it is necessary to determine the rim radius R , the effective spoke axial stiffness $E_s A_s$, the lateral stiffness at zero spoke tension K_{lat}^0 , the radial stiffness K_{rad} , and the critical buckling tension T_c . The effective axial stiffness of the butted spokes is calculated by modeling the spoke as a bar with three distinct cross-sections along its length, as described in Appendix B.1. The remaining parameters are estimated from theory: the lateral and radial stiffnesses are calculated using the mode matrix method, Eqn. (2.57), with 36 included modes and the smeared-spokes approximation (equivalent to Eqns. (2.70) and (2.64)). The buckling tension T_c is estimated using Eqn. (4.6).

⁶by radial yielding I mean yielding of the rim by in-plane bending.

Substituting these values into Eqn. (5.15) gives a predicted strength of 4.87 kN, compared with the average strength of wheels 1 and 2, 4.44 kN, a difference of less than 10%. As noted earlier, the experiment may slightly over-predict the true radial strength due to friction in the lateral carriage bearings. Evidently, the competing failure model gives a reasonable prediction for the strength in absence of lateral loads for a wheel with properties typical of those in wide use today.

5.4. Concluding remarks

The problem of buckling under external loads is significantly more complex than the problem of buckling under excessive spoke tension. Failure under external loads is controlled to some extent by a balance of two competing failure modes: buckling of the spokes (localized), and buckling of the rim (global). For lateral loads, an approximate treatment of this competition yields a rule-of-thumb of $T_{opt} = 0.5T_c$ for maximizing the lateral load the wheel can withstand without spokes buckling. For radial loads, the competing mode model gives a prediction of the buckling load which matches well with simulations and experiments.

The critical tension T_c plays an important role in wheel failure. Although the buckling tension for a wheel with a modern double-wall rim is generally too high to approach in practice, the effect of tension on lateral stiffness controls the failure under external loads. The critical tension is an important metric to be optimized through design even if the maximum tension will never be exceeded. The competing failure modes model assumes that the peak load is not sensitive to tension. This assumption has been validated against computational simulations but should also be validated experimentally. It is likely that the tension will have a strong effect on the dominant failure mode. A wheel built with low tension will likely experience significant rim yielding prior to lateral buckling, a failure mode which was ignored in this analysis.

It's difficult to imagine a realistic scenario in which a wheel would collapse under a purely radial load since any misalignment between the load and the plane of the wheel produces a lateral force. The testing apparatus built at Northwestern University has the ability to apply combined loads. The experiments described in this chapter showed a significant effect of lateral load: an increase in lateral force of 162 N resulted in a reduction in radial strength of almost 1 kN. With a few more tests, a failure diagram could be constructed which would define a safe region in lateral force—radial force space. Such a diagram for spoke buckling load rather than peak load could already be constructed with the linear theory described in Chapter 2.

Wheel failure may also depend on the details of the rim cross-section. It has been assumed here that the bending and torsion stiffness of the rim are sufficient for predicting its structural behavior. However, two rims with identical stiffness may vary considerably in their resistance to plastic yielding. A buckled wheel may yield under a combination of bending and torsional strain and the relative importance of these two modes may have implications for the ability to easily repair such a rim [90].

CHAPTER 6

Optimization of bicycle wheels

A thesis entitled “Reinventing the Wheel” would not be complete without delving into the topic of optimization. For 150 years, bicycle designers and wheelbuilders have sought to improve the wheel across multiple performance metrics by changing dimensions, materials, and construction methods. This process occurred largely by trial-and-error, although in recent years component design has been greatly aided by finite-element simulation. My intent in this chapter is not to give an exhaustive optimization routine which can be followed to give the perfect wheel under any set of performance criteria, but rather to explore general trends which emerge when optimizing the wheel under a highly restrictive set of constraints.

Optimization requires at minimum a space of tunable design parameters, an objective function defining the performance characteristic or characteristics to be optimized, and a model which predicts the performance characteristic as a function of the design parameters. Some design parameters are tunable by the wheelbuilder such as lacing pattern, spoke type, and component selection, while others are tunable by the component manufacturer such as rim cross-section shape, material, and hub flange spacing.

Keller tackled the problem of optimizing the spoke geometry in order to maximize a weighted sum of the lateral stiffness and torsional stiffness [42]. With this objective function, most design parameters are trivial (e.g. spoke diameter will always optimize to the maximum possible value) so he limited the design space to the number of spokes on the left and right sides (with the total number fixed) and the in-plane spoke inclination angles (β in this thesis). He used formulas for the lateral and torsional stiffness from Goldberg [31] which are flawed in several respects¹ although they trend in the correct direction. Keller’s optimized wheels have different numbers of spokes on the left and right sides even for symmetrically-dished wheels,

¹First, Goldberg treats the rim as a rigid body. This is a reasonable approximation for the torsional stiffness (Goldberg’s formula is approximately equivalent to Eqn. (2.65) in this thesis), however it is grossly incorrect for the lateral stiffness. Second, even if the rigid-rim approximation is used, Goldberg’s formula gives a value which is approximately 50% higher than the correct result (Eqn. (2.72) in this thesis). This is apparently due to Goldberg’s assumption that the rim translates as a rigid body in the lateral direction without rotation under a point load, which violates equilibrium as well as good sense.

Table 6.1. Comparison of selected references on wheel optimization.

Ref.	Subject	Design space	Objective	Model	Algorithm
[42]	bicycle wheel	spoke lacing pattern	Weighted average of lateral stiffness and rotational stiffness	Rigid rim, linear-elastic spokes ^a	brute-force search over hypercube
[83]	bicycle wheel	spoke lacing pattern	Multi-objective: stiffness and peak spoke force	Rigid rim, linear-elastic spokes ^b	Genetic algorithm NSGA-II and NSGA-III [19, 18]
[92]	automotive wheel	material distribution	Mean compliance ^c	2D (plane stress) finite-element method	Bi-directional evolutionary structural optimization (BESO) [39]

^a Using equations developed by Goldberg [31].

^b Using a video-game multiphysics engine.

^c Minimized the stored strain energy under a fixed loading scenario.

which suggests flaws in implementation². However, it is common to use spokes of different thicknesses on the left and right sides of an asymmetrically-dished wheel.

Svensson optimized spoke lacing patterns using a multi-objective evolutionary approach [83]. The multi-objective framework is attractive for the bicycle wheel problem because the range of sensible objective functions (compliance, peak stress, mass) have different units and do not combine in a straightforward or unique way. Rather than searching for global optimum solutions, Svensson searched for solutions lying near the Pareto-optimal front (sets of solutions in which neither objective function can be minimized without penalizing another one). The lacing pattern was represented as prescribed connections between evenly-spaced hub holes and rim holes, so all of the evolved patterns could conceivably be realized with off-the-shelf components, unlike in Keller’s approach. A major drawback of Svensson’s approach is the simplicity of the wheel model: the rim is represented as a rigid ring, while the spokes are treated as linear springs. The loads were applied at fixed locations, so some solutions evolved highly asymmetric spoke patterns which exploited the simulator by concentrating spokes at the load points. Nevertheless, the optimizer found several conventional spoke patterns including the ubiquitous “3-cross” pattern, and something closely resembling the lesser-known “crows-foot” pattern.

²In calculating the lateral stiffness, he occasionally came across negative values which he incorrectly attributed to buckling. Goldberg’s formulas do not capture elastic instability and the error is more likely due to a misinterpretation.

Zuo, Xie, and Huang optimized the material distribution in automotive wheels using a topology optimization approach [92]. They enforced a circumferential periodicity constraint with a prescribed number of pie-slice-shaped unit cells in order to guarantee realizable solutions. Wheel performance was assessed by a 2-dimensional finite-element model under differently-weighted combined loadings including tire pressure, tangential (braking or acceleration) traction, and distributed radial pressure from the ground reaction. Several of the optimum wheels generated bear striking resemblance to existing designs. Increasing the number of unit cells caused optimal designs for differently-weighted loading scenarios to converge to structurally similar layouts.

Neither of the studies on bicycle wheels [83, 42] reviewed here and no study that I am aware of incorporates the behavior of the rim into an optimization strategy for the bicycle wheel. A system-level approach to optimization of the wheel must consider the realistic mechanics of the wheel, especially given the relative flexibility of the rim compared to the spoke system. Even the wheelbuilder selecting off-the-shelf components has a daunting array of choices in materials and cross-sections. In this chapter I will explore a simplified optimization problem parameterized by only the mass fraction of the rim, and illustrate the trends and scaling laws for size and mass that emerge from this highly constrained problem.

6.1. Performance criteria

This thesis is focused on structural behavior, so the performance criteria here will be restricted to structural characteristics. Many other relevant criteria including aerodynamics, effective inertia³, and even aesthetics could be considered, but are beyond the scope of this thesis. The performance criteria considered here are lateral stiffness, buckling tension, and radial strength.

Lateral stiffness. The lateral stiffness is perhaps the most intuitive parameter to the average consumer. Unlike the radial stiffness, which is orders of magnitude higher than the stiffness of the tire, the lateral stiffness is small enough that it may affect the handling, stability, and “feel” of the bicycle [71, 80]. As discussed in Chapter 5, the lateral stiffness and spoke tension interact to give the maximum lateral force which can be withstood without spoke buckling.

³including translational and rotational inertia with a no-slip condition.

Buckling tension. The spokes must be sufficiently tight to support external loads without buckling, but not so tight that the lateral stiffness of the wheel is severely reduced. As a general rule of thumb, the tension should be around 50% of the critical tension (see Section 5.1). Even though the critical tension is in no danger of being exceeded for most reasonable wheel designs, increasing the critical tension allows the wheelbuilder to safely build to a higher tension.

Radial strength. The radial strength, approximated by the competing failure modes model described in Section 5.2.3, is important for the carrying capacity and ability to withstand radial overload from potholes or steep drops.

The performance criteria described here are not independent—increasing the lateral stiffness generally increases the buckling tension and the radial strength.

6.2. Design space

The design space for a bicycle wheel includes parameters under the control of the wheelbuilder such as the rim type, spoke type, spoke lacing pattern, and average spoke tension, and parameters under the control of the component manufacturer such as hub dimensions and rim cross-section.

6.2.1. Relevant design parameters

The structural characteristics of the wheel should not vary significantly from point to point on the rim. It would do no good to significantly reinforce one segment of the wheel, only to have the wheel buckle after rotating 180°. In this chapter we will restrict our attention to periodic spoke patterns which can be accurately modeled by the smeared-spokes approximation. Furthermore, decades of iteration have failed to produce a spoke pattern which has significant practical benefits over the traditional cross-laced pattern used on the majority of bikes. The lateral and radial stiffness are not significantly affected by the in-plane spoke angle β while the torsional stiffness is maximized when the spokes are tangent or semi-tangent to the hub. It is sufficient to first optimize the design parameters of a radial-spoked wheel and then substitute tangential spokes.

One aspect of the wheel which has been aggressively and successfully optimized is the rim cross-section. The earliest bicycle rims were made of wood, which was later supplanted by strip steel for most consumer

Table 6.2. Wheel design parameters.

Component	Symbol	Name	Optimizes to	Parameterization
Hub	w_h	hub width	$\approx 2R$	w_h/R constrained
	d_h	hub flange diameter	$\approx 2R$	d_h/R constrained
Rim	R	rim radius	zero	constrained
	r	cross-section radius	∞	r/R constrained
	t_w	wall thickness	zero	Eqn. (6.5)
	ρ_r	mass density	N/A	
	E, G	elastic moduli	N/A	
Spokes	n_s	number of spokes	∞	Eqn. (6.7)
	A_s	cross-sectional area	zero	
	ρ_s	mass density	N/A	
	E_s	Young's modulus	N/A	

rims. Wood remained the material of choice for racing until the development of extruded aluminum profiles which allowed the creation of very complex interior geometries⁴. Rims with a hollow channel (double-wall rims) are superior to single wall rims because of their greatly increased torsional stiffness. There may still be opportunities to optimize the particular shape of the rim cross-section, however in the interest of generality I will assume that the rim cross-section is a hollow circle, characterized by its outer radius r and wall thickness t_w . The second moments of area for bending and torsion are:

$$(6.1) \quad I_1 = I_2 = \frac{\pi}{4}[r^4 - (r - t_w)^4], \quad J = \frac{\pi}{2}[r^4 - (r - t_w)^4]$$

The wheel parameters considered are given in the first column of Table 6.2.

6.2.2. Narrowing the design space

The full design space described in Table 6.2 has seven dimensions plus two categorical variables (rim and spoke material). However, many of these parameters are either highly constrained or trivially optimize to one of their extreme limits. The rim radius will go to zero if left unconstrained, or to its minimum value if constrained. Likewise, the rim cross-section radius will optimize to its maximum value. The only remaining non-trivial rim parameter is the cross-section thickness, which can also be parameterized by the rim mass.

⁴Mavic covertly introduced an aluminum rim, painted to look like wood, into the 1934 Tour de France [36].

The rim parameters are linked by the equation

$$(6.2) \quad m_{rim} = 2\pi^2 \rho_r R (2rt_w - t_w^2)$$

where ρ_r is the mass density of the rim material. The spoke parameters are similarly linked. If the smeared spokes approximation is used, the stiffness of the spokes system only depends on the total cross-sectional area of the spokes, $n_s A_s$. If the discrete spokes method is used, n_s will tend towards infinity while A_s tends towards zero. Like the rim parameters, the spoke parameters can be grouped and parameterized by the total mass of the spokes:

$$(6.3) \quad m_{spk} = \rho_s n_s A_s l_s$$

where ρ_s is the mass density of the spoke material. The hub parameters are important for how they affect the geometry of the spoke system. In this thesis it is assumed that the hub is much stiffer than the spoke and rim system. If the hub flange diameter is not constrained it will exploit the hub rigidity assumption by optimizing to a value close to the diameter of the rim, thereby shortening the spokes and increasing the spoke bracing angle. The hub width will always optimize to make the spoke angle approximately 45° to maximize the lateral stiffness for a given volume⁵. The hub width is constrained by the available space in the frame after accommodating the sprockets, and should be fixed.

6.2.3. Rim mass fraction

The complete design vector for a wheel, under the constraints and assumptions described above, can be written as

$$(6.4) \quad \chi = \left\{ f_{rim}, (R, M), \left(\frac{r}{R}, \frac{w_h}{R}, \frac{d_h}{R} \right), (E, G, E_s, \rho_r, \rho_s) \right\}$$

where $f_{rim} = m_{rim}/M$ is the fraction of wheel mass in the rim, and $M = m_{rim} + m_{spk}$ is the total mass of the wheel, not counting the hub. The remaining groups in the design vector are as follows: $\chi_{extent} = (R, M)$

⁵This can be demonstrated by the following argument: noting that if the hub diameter is much smaller than the rim diameter, the rim radius is approximately $R \approx l_s \cos \alpha$. The lateral stiffness of a single spoke is $K_s^{lat} = (E_s A_s / l_s) \sin^2 \alpha$. If the volume $V_s = A_s l_s$ is held fixed, the lateral stiffness becomes $K_s^{lat} = E_s V_s / R^2 \cos^2 \alpha \sin^2 \alpha$. This function is maximized at $\alpha = 45^\circ$, implying a hub width approximately equal to the rim diameter.

are the extensive properties of the wheel (radius and mass). $\chi_{geom} = \left(\frac{r}{R}, \frac{w_h}{R}, \frac{d_h}{R}\right)$ are dimensionless properties governing the geometry of the wheel including the rim slenderness r/R , the dimensionless hub width w_h/R , and the dimensionless hub diameter d_h/R . The material vector $\chi_{matl} = (E, G, E_s, \rho_r, \rho_s)$ describes the relevant material properties of the rim and spokes.

Described in this manner the design vector provides a way to compare wheels of equivalent size, shape, and materials. It does not make sense to compare a wheel with a 50 mm hub width to a wheel with a 70 mm hub width, nor to compare a 700C wheel to a 20" folding bike wheel; one will always outperform the other on the metrics considered here. The remaining relevant parameter, the rim mass fraction, is an intuitive design parameter which can be optimized for a wheel of a given size, geometry, and material. Low f_{rim} means more or heavier spokes with a slender rim while high f_{rim} means a heavier rim supported by fewer or lighter spokes.

In terms of the parameters collected in the design vector, the rim wall thickness, spoke length, and total spoke cross-sectional area are:

$$(6.5) \quad t_w = R \left[\left(\frac{r}{R}\right) - \sqrt{\left(\frac{r}{R}\right)^2 - \frac{f_{rim}M}{2\pi^2\rho_r R^3}} \right]$$

$$(6.6) \quad l_s = R \sqrt{\left[1 - \frac{1}{2} \left(\frac{d_h}{R}\right)\right]^2 + \frac{1}{4} \left(\frac{w_h}{R}\right)^2}$$

$$(6.7) \quad n_s A_s = \frac{M(1 - f_{rim})}{l_s \rho_s}$$

The hub flange diameter clearly cannot exceed twice the rim radius. For the reasons described above, (d_h/R) will be fixed at 0.166 for all the wheels studied here. Nominally, the rim mass fraction f_{rim} may vary from zero (all spokes) to one (all rim). However, if χ_{extent} , χ_{geom} , and χ_{matl} are fixed, f_{rim} may have an upper bound less than one due to the fact that the rim wall thickness cannot be greater than the cross-section radius.

$$(6.8) \quad f_{rim}^{max} = \min \left\{ 1.0, \frac{2\pi^2 R^3 \rho_r}{M} \left(\frac{r}{R}\right)^2 \right\}$$

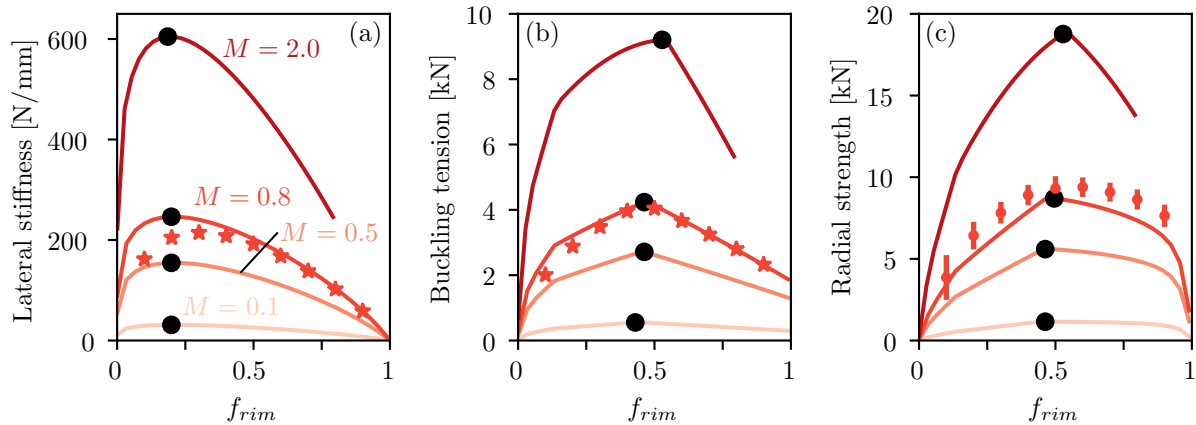


Figure 6.1. Trends in one-parameter optimization. (a) Lateral stiffness. (b) Buckling tension. (c) Radial strength. $M = 0.1, 0.5, 0.8$ and 2.0 kg. $R = 0.3$ m. $n_s = 36$. $r/R = 0.033$. $d_h/R = w_h/R = 0.167$. Rim material: aluminum ($E = 69$ GPa, $G = 26$ GPa, $\rho_r = 2700$ kg m $^{-3}$). Spoke material: steel ($E_s = 200$ GPa, $\rho_s = 8000$ kg m $^{-3}$).

6.3. One-parameter optimization

With χ_{extent} , χ_{geom} , and χ_{matl} fixed, the optimization problem outlined above reduces to a bounded, single-parameter search over f_{rim} . Figure 6.1 shows how the performance criteria outlined in Section 6.1 vary with f_{rim} for wheels with different masses.

The optimum rim mass fraction to maximize the lateral stiffness does not depend on M or R . The lateral stiffness favors a relatively light rim and heavy—or many—spokes. This strategy also has the advantage that concentrating the mass in the spokes decreases the rotational inertia of the wheel for a given mass and radius. The behavior of K_{lat} with f_{rim} reflects the differing roles of the spokes and rim in supporting loads. The spokes support external loads and channel forces to the hub, while the rim acts mainly to spread the load so that it is shared between several spokes. The positive returns on increased rim mass diminish once the rim is sufficiently stiff to involve a few spokes in the load-affected area.

High lateral stiffness is not useful if the spokes cannot withstand service loads without buckling. A strong wheel should be capable of withstanding tensions in excess of the expected loads without significantly reducing the lateral stiffness. The critical buckling tension does not vary smoothly due to the discrete buckling modes, $n = 2, 3, \dots$. As the rim mass approaches zero the buckling tension approaches zero (the

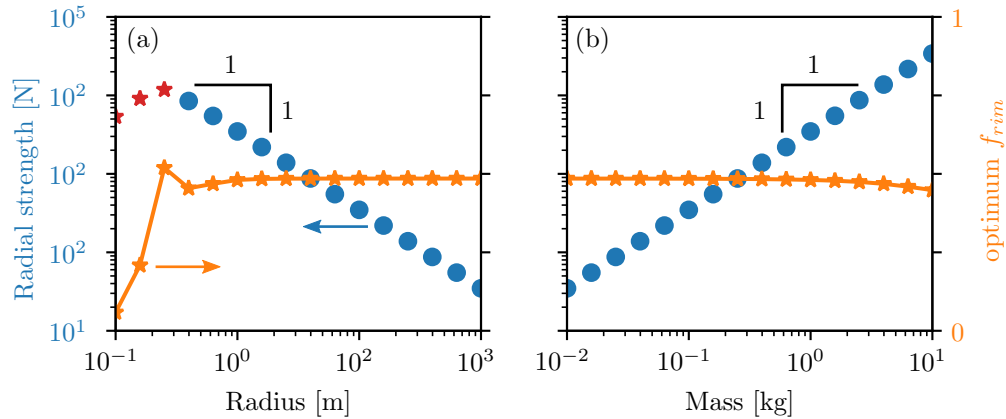


Figure 6.2. Scaling of strength with size and mass. χ_{geom} and χ_{matl} are the same as in Fig. 6.1. (a) Scaling with radius ($M = 1$ kg). (b) Scaling with mass ($R = 1.0$ m).

spokes cannot be tensioned without a rim to support the compressive reaction force). A rim with no spokes *can* support non-zero tension (in this case the wheel reduces to the problem of a radially-loaded ring studied by Timoshenko [85]), but has no ability to channel forces to the hub.

The radial strength involves both the lateral stiffness and the buckling tension, as described in Chapter 5. Following the trend of \bar{T}_c , optimizing the radial strength favors roughly equal mass in the rim and the spokes. An optimum wheel seems to obey Aristotle's advice to seek a happy medium between stiff spokes and a stiff rim.

6.4. Scaling of strength with size and mass

Figure 6.2 shows how the strength varies with radius or mass, holding the other fixed. At each value of R or M , the maximum rim mass fraction and optimum rim mass fraction are calculated. When the total mass M is less than the mass of the fully dense rim, the optimum rim mass fraction is stable and independent of R or M . The red stars in Fig. 6.2 (a) are solutions for which the maximum rim mass fraction is less than one.

Scaling by structural analogy. The radial strength is governed by buckling. We can discover the scaling law for buckling strength by analogy with a familiar structure: the Euler column. The buckling load for an Euler column scales as $P_c \sim EI/L^2$, or alternatively, $P_c \sim K_{lat}L$. If the dimensions of the column (length,

width, depth) are all scaled by the same scaling factor γ , then the buckling load scales as $P_c \sim \gamma^2$. The column mass scales with the volume, i.e. γ^3 . Therefore, the strength scaling can be rewritten $P_c \sim M\gamma^{-1}$.

The bicycle wheel stiffness is a function of both the rim stiffness, which scales as $EI/R^3 \sim \gamma$, and the spoke stiffness, which also scales as $E_s A_s/R \sim \gamma$. By analogy with the hinged column model, the radial buckling load also scales as $K_{lat}R \sim \gamma^2$. We arrive at the same results as for the Euler column, namely:

$$(6.9a) \quad P_c \sim MR^{-1}$$

$$(6.9b) \quad \frac{P_c}{M} \sim R^{-1}$$

Equation (6.9) illustrates how the size of a wheel affects its strength. The structural efficiency of a wheel—its strength-to-weight ratio—is meaningless without accounting for its size, hence the observation by Papadopoulos commenting on Burgoyne and Dilmaghanian [12] that “a furniture caster is several times as ‘efficient’” as a typical bicycle wheel [60]. Smaller is stronger—a fact which explains both the remarkable feats of BMX riders as well as the demise of the Ordinary bicycle.

Concluding Remarks

The pursuit of the perfect bike is generally couched in superlatives: the lightest wheels, the most gears, the stiffest frame (but vertically compliant, please!). But the strength of the wheel is found not in extremes, but in delicate balance; in gentle harmony between competing or opposing forces. The spokes and the rim work together to create a strong wheel. The rim keeps the spokes under tension and spreads out loads to be shared by multiple spokes, while the spokes channel forces to the hub and prevent the rim from buckling. Bending and torsion modes in the rim compete for strain energy, ultimately favoring the mode with the smaller stiffness. These stiffnesses should not differ greatly in an efficient wheel.

The theory developed here, and the experiments validating it, clearly demonstrate for the first time the competing effects of spoke tension: increasing tension prevents the spokes from going slack under load, but decreases the lateral stiffness of the rim. Under external loads, the balance between these two effects determines the dominant failure mode: spoke buckling (loss of stiffness), or rim bucking (unstable collapse).

The bicycle wheel is already a popular subject of study for hobbyists or engineering students learning to use finite-element codes. But experimentation has been hampered by the difficulty of obtaining the section properties of the rim. The four-point bending test, qualitatively described by Jim Papadopoulos and quantitatively analyzed here, can be used to obtain EI_2 and GJ with the help of a dial indicator, a laser pointer, and some known weights. But even these tools or the expertise to use them properly may be out of reach for many enthusiasts. The acoustic test described here can be performed with nothing more than a smartphone and a piece of string and could be easily implemented in an app. It may also be possible to use the acoustic test on a complete wheel to estimate the lateral stiffness or the buckling tension.

A number of interesting questions remain unexplored. The modal stiffness results described in Section 4.4 suggest that spoke behavior may be sensitive to boundary conditions. The stiffness contribution of the J-bend, inbound spokes used in that study fell well-short of their ideal stiffness. The lateral stiffness results

described in Section 2.6.2, (outbound spokes laced to a hub with slightly differently-sized holes) showed no evidence of this non-ideal behavior. A relatively simple test fixture could be designed to measure spoke stiffness at a range of tensions while controlling a variety of variables.

This thesis did not attempt a detailed analysis of stresses over the rim cross-section. Knowledge of the stress distribution under large loads could reveal how and where plastic deformation occurs during buckling. Fatigue can also lead to damage and failure of the rim, especially near spoke holes. The inside surface of the rim at the ground contact point experiences tensile stress due to the bending moment and a reduction in local stresses near the hole as the spoke relaxes. These alternating stresses are superimposed on the static compressive stress due to the average spoke tension. The competition between these stresses could affect the growth of fatigue cracks around spoke nipples.

These and many other questions will continue to engage engineers, wheelbuilders, and students of all types. I hope that the theoretical framework, experimental techniques, and computational tools developed here can be a starting point for new investigations into the mechanics of the bicycle wheel.

References

- [1] Roues artisanales blog. *in French*. <http://www.rouesartisanales.com>.
- [2] Discussion: Stresses in the Ferris Wheel. *Engineering News and American Railway Journal*, 31:349–350, 1894.
- [3] J. A. D. Ackroyd. Sir George Cayley: The Invention of the Aeroplane near Scarborough at the Time of Trafalgar. *Journal of Aeronautical History*, 1:130–181, 2011.
- [4] J. Alim, A. Koukhtieva, M. Lamnyi, and S. Tebbe. MEIE 4702 Capstone Report Fall 2016: Bicycle Wheel Strength Tester. Technical report, Northeastern University Department of Mechanical Engineering and Industrial Engineering, Boston, MA, 2016.
- [5] J. Allen. Check Spoke Tension by Ear. *SheldonBrown.com*, 1997. <https://www.sheldonbrown.com/spoke-pitch.html>.
- [6] A. Allsop, P. Dallard, and B. McNiven. The Singapore Flyer and Design of Giant Observation Wheels, Singapore. *Structural Engineering International*, 19(1):12–16, feb 2009.
- [7] J. R. Barber. Shear and Torsion of Thin-walled Beams. In *Intermediate Mechanics of Materials*, chapter 6, pages 287–352. Springer Science+Business Media B.V., 2nd edition, 2011.
- [8] M. A. Bradford and Y.-L. Pi. Elastic Flexural-Torsional Buckling of Discretely Restrained Arches. *Journal of Structural Engineering*, 128(6):719–727, 2002.
- [9] M. A. Bradford and Y.-L. Pi. Elastic flexural-torsional buckling of circular arches under uniform compression and effects of load height. *Journal of Mechanics of Materials and Structures*, 1(7):1235–1255, 2006.
- [10] J. Brandt. *The Bicycle Wheel*. Avocet, Palo Alto, CA, 3rd edition, 1993.
- [11] S. Brown and J. Allen. Wheelbuilding. *SheldonBrown.com*, 2011. <https://www.sheldonbrown.com/wheelbuild.html>.
- [12] C. J. Burgoyne and R. Dilmaghanian. Bicycle wheel as prestressed structure. *Journal of Engineering Mechanics*, 119(3):439–455, 1993.
- [13] C. F. Caunter. *The History and Development of Cycles*. Her Majesty’s Stationery Office, London, 1955.
- [14] J. Y. Chung, A. J. Nolte, and C. M. Stafford. Surface wrinkling: A versatile platform for measuring thin-film properties. *Advanced Materials*, 23(3):349–368, 2011.

- [15] N. Clayton. The Development of the Suspension Wheel. In *International Cycling History Conference 2*, pages 46–49, Saint-Etienne, France, 1991.
- [16] M. A. Crisfield. A fast incremental/iterative solution procedure that handles "snap-through". *Computers and Structures*, 13(1-3):55–62, 1981.
- [17] J. Crown and G. Coleman. *No Hands: The Rise and Fall of the Schwinn Bicycle Company, an American Institution*. Henry Holt & Co., 1996.
- [18] K. Deb and H. Jain. An Evolutionary Many-Objective Optimization Algorithm Using Reference-Point-Based Nondominated Sorting Approach, Part I: Solving Problems With Box Constraints. *IEEE Transactions on Evolutionary Computation*, 18(4):577–601, aug 2014.
- [19] K. Deb, A. Pratap, S. Agarwal, and T. Meyarivan. A fast and elitist multiobjective genetic algorithm: NSGA-II. *IEEE Transactions on Evolutionary Computation*, 6(2):182–197, apr 2002.
- [20] T. Dornbusch, P. Doyle, D. Lamb, O. Schneider, S. Simon, and E. Wilgenbusch. ME 398 Capstone Design Report: Bicycle Wheel Testing Apparatus. Technical report, Northwestern University, Department of Mechanical Engineering, Evanston, IL, 2018.
- [21] D. J. Ewins. *Modal testing: theory and practice*. Wiley, New York, 1984.
- [22] M. Feng, Y. Fukuda, M. Mizuta, and E. Ozer. Citizen sensors for SHM: Use of accelerometer data from smartphones. *Sensors (Switzerland)*, 15(2):2980–2998, 2015.
- [23] T. A. Fine. Hubs hang from the rim! <http://hea-www.harvard.edu/~fine/opinions/bikewheel.html>, 1998.
- [24] M. Ford and O. Balogun. Analytical Model for the Radial Strength and Collapse of the Bicycle Wheel. In *6th Annual International Cycling Safety Conference*, Davis, CA, Sep 2017.
- [25] M. Ford, J. M. Papadopoulos, and O. Balogun. Buckling of the bicycle wheel. In *Proceedings of the 2016 Bicycle and Motorcycle Dynamics Conference*, 2016.
- [26] M. Ford, P. Peng, and O. Balogun. Acoustic Modal Testing of Bicycle Rims. *Journal of Nondestructive Evaluation*, 37(1):1–7, 2018.
- [27] J. Forester. Held Up By Downard Pull. *American Wheelmen*, Aug 1980. <http://johnforester.com/Articles/BicycleEng/Wheel.htm>.
- [28] H. P. Gavin. Bicycle-Wheel Spoke Patterns and Spoke Fatigue. *Journal of Engineering Mechanics*, 122(8):736–742, 1996.
- [29] P. Ghanta. Fuel Efficiency: Modes of Transportation Ranked By MPG. <https://truecostblog.com/2010/05/27/fuel-efficiency-modes-of-transportation-ranked-by-mpg/>, 2010.
- [30] M. Glaskin. The science behind spokes. *Cyclist Magazine*, 2015.
- [31] L. Goldberg. *The Spoking Word*. Cascade Bicycle Products, Bellingham WA, 1984.

- [32] J. Grebenik, Y. Zhang, C. Bingham, and S. Srivastava. Roller element bearing acoustic fault detection using smartphone and consumer microphones comparing with vibration techniques. In *17th International Conference on Mechatronics - Mechatronika (ME)*, number 1, pages 1–7, 2016.
- [33] Y. L. Guo, S. Y. Zhao, C. Dou, and Y.-L. Pi. Out-of-Plane Elastic Buckling of Circular Arches with Elastic End Restraints. *Journal of Structural Engineering*, 140(10):9, 2014.
- [34] T. Hadland and H.-E. Lessing. *Bicycle Design*. MIT Press, Cambridge, MA, 2014.
- [35] A. D. Hartz. Finite Element Analysis of the Classic Bicycle Wheel, 2002.
- [36] D. V. Herlihy. *Bicycle: The History*. Yale University Press, 2004.
- [37] M. Hetenyi. *Beams on elastic foundation*. Univ. of Michigan Press, Ann Arbor, MI, 1946.
- [38] R. Hjertberg. Wheelbuilding Tip No. 19 - How Tight is Right? <https://www.wheelfanatyk.com/blog/wheelbuilding-tip-19-tight-right>, 2014.
- [39] X. Huang and Y. M. Xie. Convergent and mesh-independent solutions for the bi-directional evolutionary structural optimization method. *Finite Elements in Analysis and Design*, 43(14):1039–1049, oct 2007.
- [40] J. D. Hunter. Matplotlib: A 2d graphics environment. *Computing in Science Engineering*, 9(3):90–95, May 2007.
- [41] Y. J. Kang and C. H. Yoo. Thin-Walled Curved Beams. I: Formulation of Nonlinear Equations. *Journal of Engineering Mechanics*, 120(10):2072–2101, 1994.
- [42] J. Keller. Optimisation of the Spoked Bicycle Wheel. Master’s thesis, University of Southern Queensland, 2013.
- [43] M. Kern. Finite Element Analysis Simulation of Bicycle Wheel Buckling. Technical report, Northeastern University, 2016.
- [44] Q. Kong, R. M. Allen, L. Schreier, and Y. W. Kwon. MyShake: A smartphone seismic network for earthquake early warning and beyond. *Science Advances*, 2(2):e1501055, 2016.
- [45] G. Kopecky. Debunking Wheel Stiffness. *SlowTwitch.com*, 2013.
- [46] E. Larson. *The Devil in the White City: Murder, Magic, and Madness at the Fair That Changed America*. Vintage Books, 2004.
- [47] K. A. Lazopoulos. Column buckling under friction. *Archive of Applied Mechanics*, 61(4):215–221, 1991.
- [48] N. H. Lim and Y. J. Kang. Out of plane stability of circular arches. *International Journal of Mechanical Sciences*, 46(8):1115–1137, 2004.
- [49] A. P. Mann, N. Thompson, and M. Smits. Building the British Airways London Eye. *Proceedings of the Institution of Civil Engineers - Civil Engineering*, 144(2):60–72, 2001.
- [50] W. McKinney. Data structures for statistical computing in python. In S. van der Walt and J. Millman, editors, *Proceedings of the 9th Python in Science Conference*, pages 51 – 56, 2010.

- [51] W. M. McLundie. *Investigation of Two-Wheeled Road Traffic Accidents using Explicit FE Techniques*. PhD thesis, Cranfield University, 2007.
- [52] A. Meurer, C. P. Smith, M. Paprocki, O. Čertík, S. B. Kirpichev, M. Rocklin, A. Kumar, S. Ivanov, J. K. Moore, S. Singh, T. Rathnayake, S. Vig, B. E. Granger, R. P. Muller, F. Bonazzi, H. Gupta, S. Vats, F. Johansson, F. Pedregosa, M. J. Curry, A. R. Terrel, v. Roučka, A. Saboo, I. Fernando, S. Kulal, R. Cimrman, and A. Scopatz. Sympy: symbolic computing in python. *PeerJ Computer Science*, 3:e103, Jan 2017.
- [53] D. L. Miller. *City of the Century: The Epic of Chicago and the Making of America*. Simon & Schuster, New York, 1997.
- [54] J. M. Minguez and J. Vogwell. An analytical model to study the radial stiffness and spoke load distribution in a modern racing bicycle wheel. *Journal of Mechanical Engineering Science*, 222(4):563–576, 2008.
- [55] G. Morgenthal and H. Höpfner. The application of smartphones to measuring transient structural displacements. *Journal of Civil Structural Health Monitoring*, 2(3-4):149–161, 2012.
- [56] J. Ng. Finite Element Analysis of a Bicycle Wheel : The Effects of the Number of Spokes on the Radial Stiffness. Technical report, Rensselaer Polytechnic Institute, 2012.
- [57] T. E. Oliphant. *A guide to NumPy*. USA: Trelgol Publishing, 2006.
- [58] J. M. Papadopoulos. personal communication.
- [59] J. M. Papadopoulos. Aspects of stored-wheel response. *Human Power*, 5(2):1689–1699, 1986.
- [60] J. M. Papadopoulos. Comment on Bicycle wheel as prestressed structure. *Journal of Engineering Mechanics*, 121(7):847–849, 1995.
- [61] D. Pepelko. Spoke Tension Gauge. iTunes App Store, 2016.
- [62] Y.-L. Pi and M. A. Bradford. Elastic flexural-torsional buckling of continuously restrained arches. *International Journal of Solids and Structures*, 39(8):2299–2322, apr 2002.
- [63] Y.-L. Pi, M. A. Bradford, N. S. Trahair, and Y. Y. Chen. A further study of flexural-torsional buckling of elastic arches. *International Journal of Structural Stability and Dynamics*, 5(2):163–183, 2005.
- [64] Y.-L. Pi, J. P. Papangelis, and N. S. Trahair. Prebuckling deformations and flexural-torsional buckling of arches. *Journal of structural engineering*, 121(9):1313–1322, 1995.
- [65] Y.-L. Pi and N. S. Trahair. Prebuckling Deflections and Lateral Buckling. I: Theory. *Journal of Structural Engineering*, 118(11):2949–2966, 1992.
- [66] A. J. S. Pippard and W. E. Francis. On a Theoretical and Experimental Investigation of the Stresses in a Radially Spoked Wire Wheel under Loads applied to the Rim. *Philosophical Magazine*, 11(69):233–285, 1931.
- [67] A. J. S. Pippard and W. E. Francis. The Stresses in a Wire Wheel under Side Loads on the Rim. *Philosophical Magazine*, 14(91):436–445, 1932.

- [68] A. J. S. Pippard and M. J. White. The Stresses in a Wire Wheel with non-Radial Spokes under Loads applied to the Rim. *Philosophical Magazine*, 14(90), 1932.
- [69] J. Pridmore and J. Hurd. *Schwinn Bicycles*. Motorbooks, Int'l, Minneapolis, 1996.
- [70] D. Rinard. Wheel Stiffness Test. *SheldonBrown.com*. <http://sheldonbrown.com/rinard/wheel>.
- [71] G. E. Roe, W. M. Pickering, and A. Zinober. The Oscillations of a Flexible Castor, and the Effect of Front Fork Flexibility on the Stability of Motorcycles. *SAE Transactions*, 87(2):1397–1408, 1978.
- [72] H.-J. Ryu, J.-Y. Choi, G.-S. Yi, C.-O. Lee, and N.-H. Lim. Elastic Stability of Circular Arches with the Open Thin-walled Monosymmetric Section Considering the Prebuckling Deformation. pages 87–97, 2012.
- [73] N. J. Salamon and R. A. Oldham. Analysis for design of spoked bicycle wheels. *Finite Elements in Analysis and Design*, 10(4):319–333, 1992.
- [74] O. S. Salawu. Detection of structural damage through changes in frequency: a review. *Engineering Structures*, 19(9):718–723, sep 1997.
- [75] W. H. Searles. The Ferris Wheel. *Journal of the Association of Engineering Societies*, 12:614–623, 1893.
- [76] E. D. Sewall. The Bicycle Wheel. *Scientific American*, 75(16):297–298, 1896.
- [77] A. Sharp. *Bicycles and Tricycles*. MIT Press, Cambridge, MA, 2nd edition, 1977.
- [78] B. A. Smith. The Bicycle Wheel. *Report of the Meeting of the Australasian Association for the Advancement of Science*, 8:197–203, 1901.
- [79] R. A. Smith. *A Social History of the Bicycle*. American Heritage Press, 1972.
- [80] P. T. J. Spierings. The Effects of Lateral Front Fork Flexibility on the Vibrational Modes of Straight-Running Single-Track Vehicles. *Vehicle System Dynamics*, 10(1):21–35, feb 1981.
- [81] T. W. Stroberg. *Platelet Shape Change Induced by Marginal Band Instability*. PhD thesis, Northwestern University, 2016.
- [82] B. Sturges. League of American Bicyclists - Detailed History. <https://bikeleague.org/content/mission-and-history/>.
- [83] M. K. Svensson. Using Evolutionary Multiobjective Optimization Algorithms to Evolve Lacing Patterns for Bicycle Wheels Mats Krüger Svensson. Master's thesis, Norwegian University of Science and Technology, 2015.
- [84] J.-G. Teng and J. M. Rotter. Buckling of restrained monosymmetric rings. *Journal of Engineering Mechanics*, 114(10):1651–1671, 1988.
- [85] S. P. Timoshenko and J. M. Gere. *Theory of Elastic Stability*. McGraw-Hill, New York, 2nd edition, 1961.
- [86] S. P. Timoshenko and D. H. Young. *Vibration Problems in Engineering*. D. Van Nostrand Company, New York, 3rd ed. edition, 1955.

- [87] N. S. Trahair and J. P. Papangelis. Flexural-torsional buckling of monosymmetric arches. *Journal of Structural Engineering*, 113(10):2271–2288, 1987.
- [88] V. Z. Vlasov. *Thin-Walled Elastic Beams*. Israel Program for Scientific Translation, 2nd edition, 1961.
- [89] P. Weidman and I. Pinelis. Model equations for the Eiffel Tower profile: Historical perspective and new results. *Comptes Rendus - Mécanique*, 332(7):571–584, 2004.
- [90] D. G. Wilson and J. M. Papadopoulos. *Bicycling Science*. MIT Press, Cambridge, MA, 3rd edition, 2004.
- [91] C. H. Yoo. Flexural-Torsional Stability of Curved Beams. *Journal of the Engineering Mechanics Division*, 108(6):1351–1369, 1982.
- [92] Z. H. Zuo, Y. M. Xie, and X. Huang. Reinventing the Wheel. *Journal of Mechanical Design*, 133(2):024502, 2011.

APPENDIX A

Stiffness matrix for asymmetric n -cross wheel

The most general practical special case is that of the asymmetric wheel with tangent spokes and an arbitrary spoke offset vector. There are four spoke types: left-side leading, left-side trailing, right-side leading, and right-side spoke. The four independent spoke vectors are:

$$(A.1a) \quad \mathbf{n}^l = c_1^l \mathbf{e}_1 + c_2^l \mathbf{e}_2 \pm c_3^l \mathbf{e}_3$$

$$(A.1b) \quad \mathbf{n}^r = -c_1^r \mathbf{e}_1 + c_2^r \mathbf{e}_2 \pm c_3^r \mathbf{e}_3$$

The offset vector is assumed to be symmetric across the rim.

$$(A.2a) \quad \mathbf{b}_s^l = b_1 \mathbf{e}_1 + b_2 \mathbf{e}_2$$

$$(A.2b) \quad \mathbf{b}_s^r = -b_1 \mathbf{e}_1 + b_2 \mathbf{e}_2$$

The initial tension must be different on the two sides so that the lateral components balance. The left and right tensions are:

$$(A.3a) \quad T_p^l = \bar{T} \left(\frac{4\pi R c_1^r}{n_s(c_1^l c_2^r + c_1^r c_2^l)} \right)$$

$$(A.3b) \quad T_p^r = \bar{T} \left(\frac{4\pi R c_1^l}{n_s(c_1^l c_2^r + c_1^r c_2^l)} \right)$$

in terms of the average radial tension per unit circumference, \bar{T} . One further simplification is made by setting $l_s^l = l_s^r = l_s$. The spoke length generally differs by less than 1%. The smeared-spokes stiffness matrix is given below.

$$\begin{aligned}
\text{(A.4)} \quad \bar{\mathbf{k}} = & \frac{n_s E_s A_s}{4\pi R l_s} \begin{bmatrix} (c_1^l)^2 + (c_1^r)^2 & c_1^l c_2^l - c_1^r c_2^r & 0 & b_1(c_1^l c_2^l + c_1^r c_2^r) - b_2[(c_1^l)^2 + (c_1^r)^2] \\ & (c_2^l)^2 + (c_2^r)^2 & 0 & b_2(c_1^r c_2^r - c_1^l c_2^l) - b_2[(c_2^r)^2 - (c_2^l)^2] \\ & & (c_3^l)^2 + (c_3^r)^2 & 0 \\ & & & (b_1 c_2^l - b_2 c_1^l)^2 + (b_1 c_2^r - b_2 c_1^r)^2 \end{bmatrix} \\
& + \frac{\bar{T}}{l_s(c_1^l c_2^r + c_1^r c_2^l)} \begin{bmatrix} (c_1^l + c_1^r)(1 - c_1^l c_1^r) & 0 & 0 & 0 \\ & c_1^l(1 - (c_2^r)^2) + c_1^r(1 - (c_2^l)^2) & 0 & 0 \\ & & c_1^l(1 - (c_3^r)^2) + c_1^r(1 - (c_3^l)^2) & 0 \\ & & & 0 \end{bmatrix} \\
& + \frac{\bar{T}}{l_s(c_1^l c_2^r + c_1^r c_2^l)} \begin{bmatrix} 0 & c_1^l c_1^r(c_2^r - c_2^l) & 0 & -b_1 c_1^l c_1^r(c_2^l + c_2^r) - b_2[c_1^l(1 - (c_1^r)^2) + c_1^r(1 - (c_1^l)^2)] \\ & 0 & 0 & b_2 c_1^l c_1^r(c_2^l - c_2^r) + b_1[c_1^r(1 - (c_2^l)^2) - c_1^l(1 - (c_2^r)^2)] \\ & & 0 & 0 \\ & & & b_1^2[c_1^l(1 - (c_2^r)^2) + c_1^r(1 - (c_2^l)^2)] + b_2^2[c_1^l(1 - (c_1^r)^2) + c_1^r(1 - (c_1^l)^2)] \\ & & & + 2b_1 b_2 c_1^l c_1^r(c_2^l + c_2^r) \end{bmatrix}
\end{aligned}$$

APPENDIX B

Wheel properties

B.1. Standard research wheel

Many of the experiments and theoretical calculations described in this thesis use a wheel with standardized components and geometry for ease of comparison. The “standard research wheel” comprises a Sun-Ringle CR18-700C 36-hole rim laced to a custom hub with double-butteted Wheelsmith DB14 276 mm spokes. Unless otherwise noted, the spokes are all oriented outbound (with the heads on the inside of the hub flange).

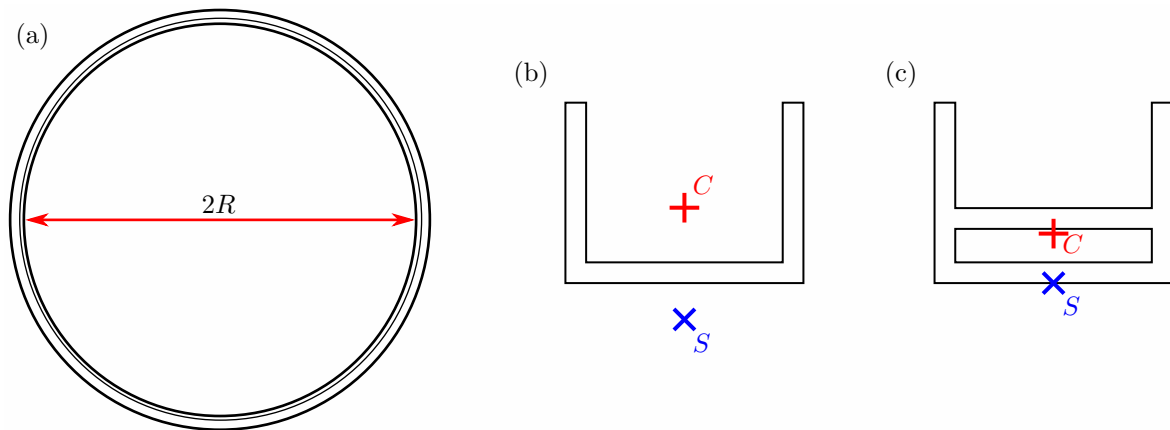


Figure B.1. (a) Diameter measurement of the Sun-Ringle CR18 rim. (b) Centroid and shear center of a thin-walled C-channel beam [85]. (c) Assumed location of the shear center of the CR18 rim cross-section.

Rim. The Sun-Ringle CR18-700C aluminum rim has a shallow double-wall construction whose shape approximates a C-channel beam. A C-channel beam with a fully-open cross-section has a shear center outside the cross-section below the web [85] (Fig. B.1 (b)). The behavior of the CR18 rim should be somewhere between that of a fully-closed, symmetric cross-section and that of a fully-open C cross-section. Therefore I measure the radius at the “bottom” of the cross-section (Fig. B.1 (c)). By this method, the effective

Table B.1. Properties of the standard research wheel and fat bike wheel.

	Standard research wheel	Fat bike wheel
Rim	Sun-Ringle CR18-700C	
R [mm]	304	300
m_{rim} [g]	538	
ρ_r [kg/m ³]	2700	
E [N/m ²]	69	69
G [N/m ²]	26	26
A [mm ²]	104	170
EI_1 [N m ²]	111 ± 9	72
EI_2 [N m ²]	219 ± 40	6995
GJ [N m ²]	26.3 ± 1.2	98
Hub	custom adjustable hub	
width [mm]	50	50
effective width (elbows in)	53	
effective width (elbows out)	48	
diameter [mm]	58	50
Spokes	Wheelsmith DB14 276 mm	
number	36	36
arrangement	radial	radial
diameter [mm]	1.7/2.0	2.0
effective diameter [mm]	1.78	
EA_{eff} [kN]	522	628

radius is 304 mm. The cross-section stiffness parameters are estimated using the acoustic method described in Chapter 3.

Hub. The custom research hub used in this thesis was designed by Joseph Alim, Mehdi Lamnyi, Alexandra Koukhtieva, and Simon Tebbe for an undergraduate capstone project sponsored by Jim Papadopoulos [4]. The hub comprises a solid chromoly steel $\frac{3}{4}$ -inch diameter “axle” with oppositely threaded ends, and two mild steel hub flanges threaded onto the axle and secured with jam nuts. With this turnbuckle design, the hub flange spacing can be changed by simply rotating the axle relative to the flanges. The research hub does not have a bearing so it cannot be rolled like a standard bicycle wheel. The purpose of the solid axle is to make the hub very stiff relative to the rim and spokes system.

Spokes. The wheel is built with stainless-steel double-buttet Wheelsmith DB14 276 mm J-bend spokes. The thick section at the top and bottom of the spoke has a diameter of 1.99 mm while the thin swaged middle section has an average diameter 1.72 mm and a length of 205 mm. The effective cross-sectional area

Table B.2. Properties of the wheels in this study. Linear dimensions are given in millimeters. EI_1 , EI_2 , and GJ are given in N m^2 .

Wheel	Rim				Hub		Spokes	
	R	EI_1	EI_2	GJ	Diam.	Width	Number	Diam.
High wheel	600	300	300	100	50	90	64	2.5
Vintage road	315	150	150	15	50	50	36	1.8
Modern road	300	200	200	80	50	50	24	1.8
Cheap MTB	280	200	200	12	50	60	32	2.0
Tandem	300	200	200	80	50	70	40	2.0
Small	225	150	150	40	50	50	32	1.8
Track	300	200	200	150	50	60	32	1.8

is calculated using the series-springs rule for the thin and thick sections:

$$(B.1) \quad \frac{l_s}{EA_{eff}} = \frac{l_1}{EA_1} + \frac{l_2}{EA_2}$$

By this method, the effective spoke diameter is 1.78 mm. For stainless steel ($E = 210 \text{ GPa}$), this gives an effective axial stiffness of $EA_{eff} = 521 \text{ kN}$.

The complete wheel properties are given in Table B.1.

B.2. Fat bike wheel

The example fat bike rim is modeled as a prismatic aluminum ($E = 69 \text{ GPa}$, $G = 26 \text{ GPa}$) beam with a hollow, thin-walled, rectangular cross-section (width: 80 mm, height: 5 mm, wall thickness: 1 mm). The relevant properties are given in Table B.1.

B.3. Example wheel library

Several example wheels are defined for the purposes of illustrative calculations and simulations. The “high wheel” represents the kind of wheel that would be found on an Ordinary, or “penny-farthing,” bicycle popular in the 1880s. The “small” wheel might be found on an adult folding bicycle or a youth bicycle. All of the properties are hypothetical and are not meant to correspond to any particular wheel or product.

All the wheels have aluminum rims ($E = 69 \text{ GPa}$, $G = 26 \text{ GPa}$, $\rho_r = 2700 \text{ kg/m}^3$) except for the high wheel rim, which is constructed of steel ($E = 200 \text{ GPa}$, $G = 80 \text{ GPa}$, $\rho_r = 8000 \text{ kg/m}^3$). The cross-sectional area of all rims is 100 mm^2 . The remaining properties are given in Table B.2.

APPENDIX C

Acoustic testing additional procedures and results

C.1. Frequency response of smartphone microphone

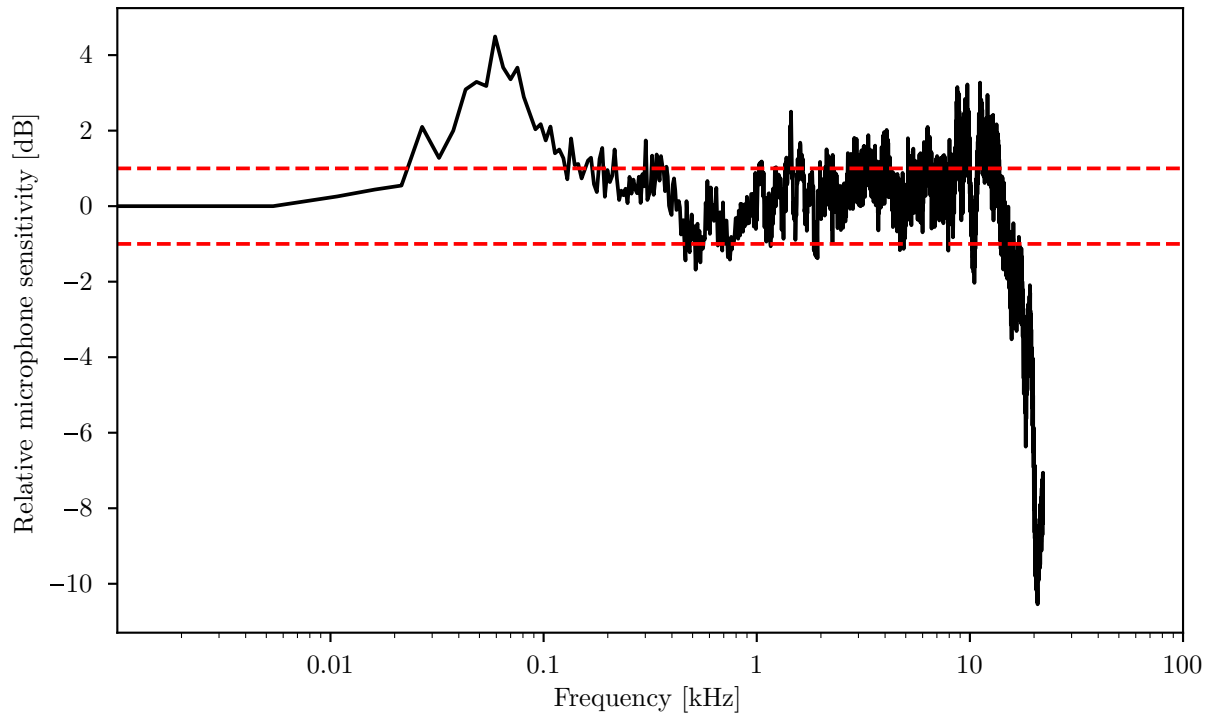


Figure C.1. Frequency response of the iPhone SE built-in microphone used in this study.

The frequency response of the built-in microphone in an Apple iPhone SE (model A1662) was measured in an anechoic chamber. The smartphone and a calibrated reference microphone with a flat frequency response (Etymotic Research ER-7C Probe Mic System) were placed on a foam block 66 inches from a single mono speaker (Roland MA-12C Micro Monitor). Approximated pink noise was generated from an online source (<https://mynoise.net/NoiseMachines/whiteNoiseGenerator.php>) and played through the

Table C.1. Rim properties determined by acoustic and mechanical tests. R is given in millimeters, m_{rim} is given in grams, EI_2 , EI_1 , and GJ are given in Nm^2 .

Rim	R	m_{rim}	Acoustic			Static		
			EI_1	GJ	μ	EI_1	GJ	μ
Alex-ALX295	305	480	310.0 ± 14.8	85.7 ± 4.7	0.405 ± 0.061	288.0 ± 17.5	96.5 ± 3.8	0.487 ± 0.017
DTS-R460	304	459	274.0 ± 13.6	103.6 ± 5.8	0.449 ± 0.065	256.0 ± 15.5	114.8 ± 5.8	0.542 ± 0.031
CR18-20"	217	380	103.0 ± 5.0	26.4 ± 1.0	0.175 ± 0.016	102.0 ± 6.2	24.7 ± 1.5	0.134 ± 0.019
CR18-700C	304	538	111.0 ± 9.2	26.3 ± 1.2	0.120 ± 0.022	113.0 ± 6.9	25.9 ± 1.7	0.099 ± 0.021
X404-27"	307	594	131.0 ± 10.6	16.9 ± 0.9	0.108 ± 0.026	134.0 ± 8.2	15.9 ± 1.0	0.068 ± 0.018
Y2000-26"	271	459	114.0 ± 7.4	14.6 ± 0.7	0.114 ± 0.021	113.0 ± 6.9	13.4 ± 0.9	0.088 ± 0.019
Y2000-700C	302	551	125.0 ± 9.8	19.2 ± 1.0	0.123 ± 0.026	123.0 ± 7.5	18.9 ± 1.2	0.096 ± 0.019

speaker. A spectral average was obtained from both microphones using the Fast Fourier Transform with a buffer size of 8192 samples at 44.1 kHz sample rate with 50 averaging windows and discarding the phase. The iPhone microphone relative sensitivity was calculated by taking the ratio of the iPhone spectrum to the reference spectrum and normalizing by the amplitude at 5.38 Hz.

C.2. Peak identification procedure

The following procedure was used to identify the radial and lateral mode frequencies for each rim: First, the two spectra were compared with the noise spectrum to identify any peaks with a signal-to-noise ratio of at least 10 (note the first two apparent peaks at 27 Hz and 60 Hz are both present in the noise spectrum and can therefore be discarded). Next, the lowest peaks were compared between the lateral and radial spectra to find duplicates. In the case of duplicates, the peak was assigned to the spectrum with the greater relative magnitude.

After identifying the approximate location of each peak, the precise peak parameters were determined by fitting a Lorentzian peak function of the form:

$$(C.1) \quad F(f) = \left(\frac{1}{2\pi} \right) \frac{\Gamma}{(f - f_0)^2 + \Gamma^2}$$

Fitted curves for f_2^{rad} , f_3^{rad} , f_2^{lat} , f_3^{lat} , and f_4^{lat} are shown below:

C.3. Rim properties

Complete properties determined by the acoustic and static tests for all rims are given in Table C.1.

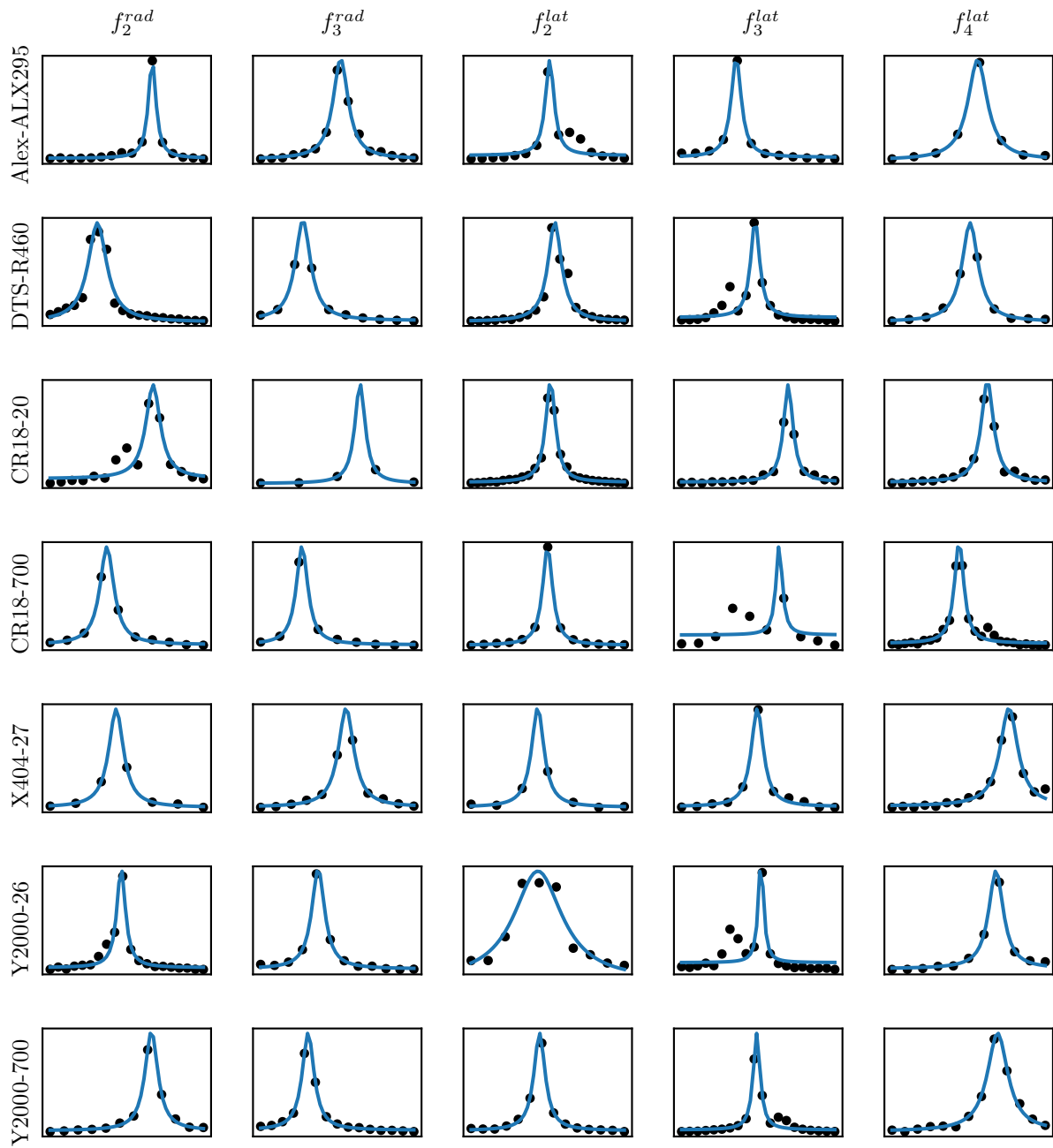


Figure C.2. Fitted peaks in frequency spectra

APPENDIX D

Tension measurement technique

I measured spoke tensions using the WheelFanatyk analog tensiometer and the calibration table supplied with the instrument. The tensiometer works on the principle that the spoke under tension behaves like a guitar string, i.e. the lateral stiffness is proportional to the tension. The spoke is loaded by a linear spring with a precisely known stiffness and the displacement is measured on the opposite side from where the load is applied. The instrument is shipped with a calibration table giving the tension for a range of displacements.

A straightforward analysis of the mechanics involved, assuming that the tension remains constant and the bending stiffness is negligible, leads to the following relationship for the tension as a function of the measured displacement:

$$(D.1) \quad T = a \left(\frac{1}{\delta} \right) + b$$

where T is the spoke tension and δ is the displacement measured in millimeters. The parameters a and b differ slightly for different spoke diameters because the preloaded spring contacts the spoke at a different point along its stroke, and thick spokes may be more affected by bending stiffness. By fitting the model above to the calibration data, I determined the following parameters for different spoke diameters:

Table D.1. Calibration constants for WheelFanatyk tensiometer.

	Spoke diameter						
Parameter	0.9 mm	0.95 mm	1.2 mm	1.5 mm	1.7 mm	1.8 mm	2.0 mm
a [N mm]	480.8	466.4	434.1	466.4	423.5	428.2	427.2
b [N]	-156.8	-189.8	-93.3	-189.8	-219.4	-273.6	-323.5

The spoke tensions reported in this thesis are calculated using the model above to effectively interpolate the values supplied by the manufacturer.

APPENDIX E

Analysis of the four-point bending test

In the four-point bending test, the rim is supported at 3 and 9 o'clock and loaded at 12 and 6 o'clock with an out-of-plane force P . A dummy torque Q is applied at each point in the same sense as the rotation of the cross-section. Free-body diagrams of the complete rim and upper section are shown below:

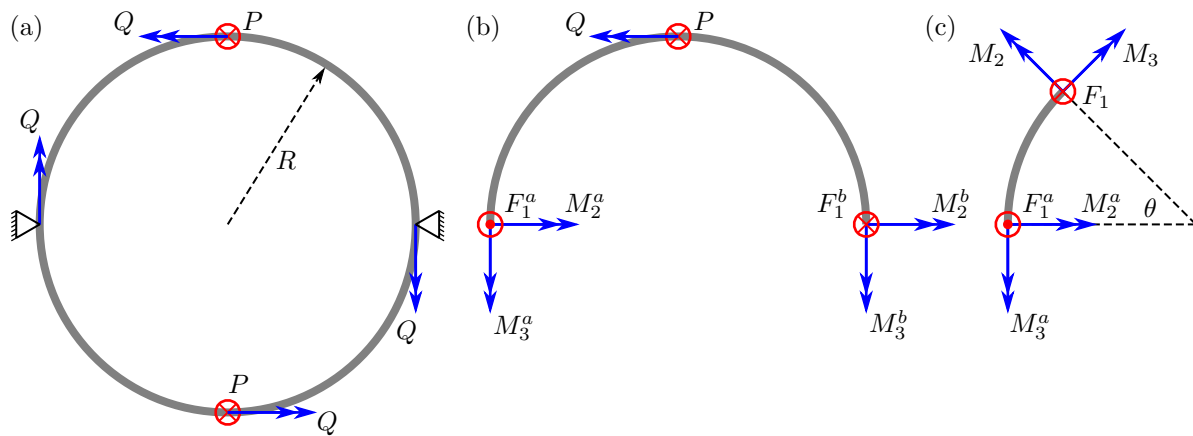


Figure E.1. (a) Force diagram for the four-point bend test. (b) Free-body diagram of the top half of the rim. (c) Free-body diagram of an arbitrary section of rim.

The internal shear, lateral bending moment, and twisting moment are F_1 , M_2 , and M_3 , respectively.

The symmetry of the problem gives us the conditions

$$(E.1a) \quad F_1^a = -F_1^b$$

$$(E.1b) \quad M_2^a = M_2^b$$

$$(E.1c) \quad M_3^a = M_3^b$$

Equilibrium of forces and moments gives

$$(E.2a) \quad F_1^a = -F_1^b = \frac{P}{2}$$

$$(E.2b) \quad M_2^a = M_2^b = \frac{PR}{2} + \frac{Q}{2}$$

$$(E.2c) \quad M_3^a = M_3^b = 0$$

The internal forces can now be determined by making a cut at an arbitrary location θ , as shown in Fig. E.1 (c). Equilibrium of forces and moments gives

$$(E.3a) \quad F_1 = \frac{P}{2}$$

$$(E.3b) \quad M_2 \cos \theta - M_3 \sin \theta = \frac{PR}{2}(1 - \sin \theta) + \frac{Q}{2}$$

$$(E.3c) \quad M_2 \sin \theta + M_3 \cos \theta = \frac{PR}{2}(\cos \theta - 1)$$

Solving (E.3) for M_2 and M_3 gives

$$(E.4a) \quad M_2 = PR(\cos \theta - \sin \theta) + \frac{Q}{2} \cos \theta$$

$$(E.4b) \quad M_3 = -PR(\sin \theta + \cos \theta) + \frac{PR}{2} - \frac{Q}{2} \sin \theta$$

The strain energy in the upper half of the rim is given by

$$(E.5) \quad U = 2 \int_0^{\pi/2} \left(\frac{M_2^2}{2EI_2} + \frac{M_3^2}{2GJ} \right) R d\theta$$

The displacement and rotation at the load point is determined using Castigliano's theorem: $u_0 = \frac{\partial U}{\partial P}$, $\phi_0 = \frac{\partial U}{\partial Q}$. This is the "balanced" deflection, i.e. the vertical deflections at each load point assuming that the slope $du/d\theta$ is zero at the supports. In the un-balanced four-point bending test (three points are constrained and the third is loaded), the displacement will be $u_l = 2u_0$.

$$(E.6) \quad u_l = -\frac{PR^3}{2GJ} [2(3 - \pi) + \mu(2 - \pi)]$$

$$(E.7) \quad \phi_l = -\frac{PR^2}{8GJ} (1 + \mu)(2 - \pi)$$